Transient Computational Fluid Dynamic Modeling of Baffled Tube Ram Accelerator

Navid Daneshvaran

A Thesis Submitted in Partial Fulfillment of the Requirements for the Degree of

Master of Science in Aeronautics and Astronautics

University of Washington
2017

Committee:

Carl Knowlen
Mitsuru Kurosaka

Program Authorized to Offer Degree:
Aeronautics and Astronautics

University of Washington

Abstract

Transient Computational Fluid Dynamic Modeling of Baffled Tube Ram Accelerator

Navid Daneshvaran

Chair of the Supervisory Committee:

Research Associate Professor Carl Knowlen

William E. Boeing Department of Aeronautics and Astronautics

Transient computational fluid dynamic modeling in laboratory frame of reference was used to investigate baffled tube ram accelerator operating characteristics in inert and reactive mixtures. The minimum entrance Mach number that allowed supersonic projectile transit through a baffled tube filled with inert gas and the thrust generated in reactive flow were examined. The primary parameters considered were chamber-to-projectile diameter ratio, projectile geometry, baffle thickness, baffle spacing and baffle geometry. Axisymmetric and three-dimensional simulations used a dynamic mesh for a projectile moving at constant Mach (ranging from 1.8 to 5.1) through stationary baffles. The maximum baffle thickness and minimum baffle spacing at velocities near the minimum allowable entrance Mach number were both found to be ~53% of the projectile diameter. Further reducing the baffle spacing resulted in the projectile pushing a normal

shockwave ahead of it like in a jet engine unstart. It was also found that thicker baffles and closer baffle spacing increased the projectile drag coefficient. Reactive flow phenomena were investigated by first establishing the combustion on the projectile in a smooth bore tube before it entered the baffled-tube section. A key finding from premixed methane and oxygen propellant simulations was that aftward-slanted baffles generated higher thrust than when the baffles were normal to the projectile or forward-slanted. This increase in thrust was associated with more complete propellant combustion in the annular baffle chambers around the tail and base sections of the axisymmetric projectile, as well as immediately behind it. It was also determined that residence time of the propellant during combustion process in the vicinity of the projectile at any given baffle, influences the overall thrust production. As the projectile Mach increases, both the propellant residence time and overall thrust level decrease.

Table of Contents

Page

Page

List of Figures

Figure numbers Page

Figure numbers Page

Figure numbers Page

Figure numbers Page

List of Tables

Table numbers Page

Glossary

a	=	speed of sound
$A_{Arrhenius}$	=	pre-exponential factor in Arrhenius rate
A	=	area
$A_{p,b}$	=	projected baffle surface area
β	=	temperature-exponent in Arrhenius rate
$BTRA$	=	baffled tube ram accelerator
γ	=	specific heats at constant pressure per constant volume for a mixture
C_d	=	coefficient of drag
C_{ED}	=	eddy-dissipation empirical constant
C_P	=	specific heat at constant pressure
D	=	drag
D_{ED}	=	eddy-dissipation empirical constant
d_c/d_p	=	chamber-to-projectile diameter ratio
d_{eff}	=	effective bore diameter
ε	=	turbulence kinetic energy dissipation rate
E_a	=	Activation energy
F	=	thrust
h	=	sensible enthalpy
I	=	non-dimensional thrust
κ	=	turbulence kinetic energy
M	=	Mach number
$M_{w,I}$	=	molecular weight of species i
$\nu'_{i,r}$	=	stoichiometric coefficient for reactant I in reaction r
$\nu''_{i,r}$	=	stoichiometric coefficient for product I in reaction r
P	=	pressure
Q	=	non-dimensional heat release parameter
Δq	=	heat release due to chemical reaction
$\Re$	=	universal gas constant
R	=	gas constant of the mixture
ρ	=	density
σ	=	rate of reaction
$SBRA$	=	smooth bore ram accelerator
T	=	temperature
$TCRA$	=	thermally choked ram accelerator
t_b	=	baffle thickness
u	=	flow velocity
φ	=	geometrical constant
V_b	=	baffle volume
V_c	=	chamber volume
V_{CJ}	=	Chapman-Jouguet detonation velocity
ω	=	specific dissipation rate
w_c	=	chamber width

$[X]_y$	=	molar concentration of species X with rate exponent y
Y_ξ	=	mass fraction of a particular reactant, ζ
Y_P	=	mass fraction of any product species

Acknowledgements

First and foremost, I like to thank my advisor, Dr. Carl Knowlen, for giving me the opportunity to work on the baffled tube ram accelerator project and continuously encouraged and inspired me to strive for the best to push my limits of understanding in various fields of study. Also, Dr. Knowlen's work-ethic and his humbleness set an excellent guidance for me to try to be a better individual.

I like to thank Dr. Andrew Higgins and Dr. Adam Bruckner for their inspiration, support, and comments in the course of developing means to model the baffled tube ram accelerator. I also like to thank Dr. Mitsuru Kurosaka as a member of my reading committee and for teaching various topics which helped me understand the flow field associated with smooth bore and baffled tube ram accelerators better.

I also like to thank Jeff Glusman and Dr. Tarek Bengherbia for their excellent theoretical, computational and experimental efforts on smooth bore and baffled tube ram accelerators which guided me in my computational works. Also, I like to thank Dr. Linda Hedges for her constructive comments on grid generation and HPC usage. The support of the following sponsors is also deeply appreciated: Joint Center for Aerospace Technology Innovation (JCATI), Washington Research Foundation (WRF), and EnergeticX, LLC.

Lastly, I like to thank my family and friends who supported me throughout my studies and kept me inspired to learn more and work hard.

Chapter 1

Introduction

The ram accelerator is a device that accelerates a sub-caliber projectile, similar to center body of ramjet, through a smooth bore tube filled with premixed fuel and oxidizer at high pressure. The combustion energy release occurs at the base of the projectile as it travels through the tube [1, 2]. A powder gun or light gas gun accelerates the projectile to supersonic speed, which must exceed the minimum entrance Mach for the ram accelerator to operate (typically above Mach 2.5 in a smooth bore). Since the projectile is sub-caliber, it is stabilized by projectile fins in a smooth bore tube or with rails mounted on the sidewalls for axisymmetric projectiles. Researchers at the University of Washington Department of Aeronautics and Astronautics have carried out theoretical and experimental research on the ram accelerator since late 1980s [1-15]. Ram accelerator velocity regimes are categorized based on velocity of the projectile relative to Chapman-Jouguet detonation velocity (V_{CJ}) of premixed fuel and oxidizer; i.e., subdetonative, transdetonative and superdetonative. Within each of these velocity regimes, the combustion process can be initiated and stabilized in several different ways [3-7].

In the subdetonative velocity regime, the projectile velocity is always less than V_{CJ} and the subsonic combustion process behind the projectile is typically stabilized by means of thermal choking at full tube area somewhere farther downstream, as shown in Fig. 1-left. In this propulsive mode, thrust decreases and theoretically goes to zero as the projectile's velocity reaches V_{CJ}. In the superdetonative velocity regime (Fig. 1-right), the projectile velocity is always greater than V_{CJ}

and all of the combustion energy release occurs supersonically (via oblique detonation, shock induced combustion, boundary layer combustion or some combination of these processes) in annular region between the body and tube wall [7-12]. Superdetonative propulsive modes are analogous to the scramjet in that they both maintain supersonic flow throughout.

Although the thermally choked ram accelerator propulsive mode is limited to V_{CJ}, experiments have shown that the projectile can smoothly accelerate from velocities below to above V_{CJ} [5, 12]. This acceleration from subdetonative to superdetonative velocities is presumed to be accomplished with a propulsive mode in which both subsonic and supersonic combustion processes occur on the body and behind the projectile, as shown in Fig. 1-middle. This mixed-mode combustion process occurs in the transdetonative velocity regime, nominally defined as $0.85V_{CJ}$ to $1.15V_{CJ}$, and results in the thrust going through a relative minimum before the combustion process moves completely up onto the body.

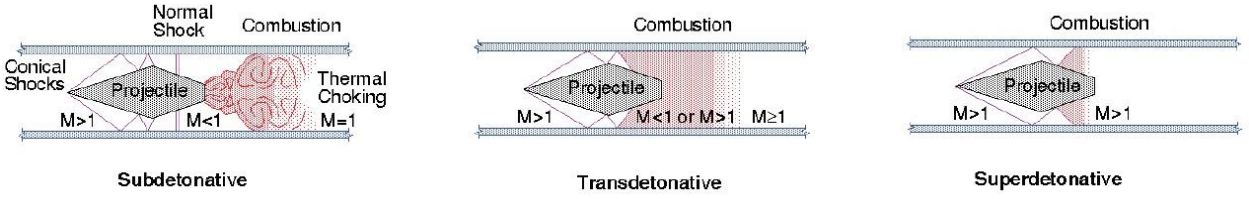

Figure 1. Propulsive modes of ram accelerator are distinguished by the velocity regime in which the projectile is being accelerated. Below V_{CJ} is subdetonative, above V_{CJ} is superdetonative, and near V_{CJ} is transdetonative velocity regime

One significant difference between the thermally choked ram accelerator propulsive mode and an air-breathing ramjet engine cycle is that its flow after combustion is thermally choked at full tube area behind the projectile instead of with a converging nozzle, as shown in Fig. 2. A second major difference is that in the ram accelerator, the propellant is premixed in the tube. This

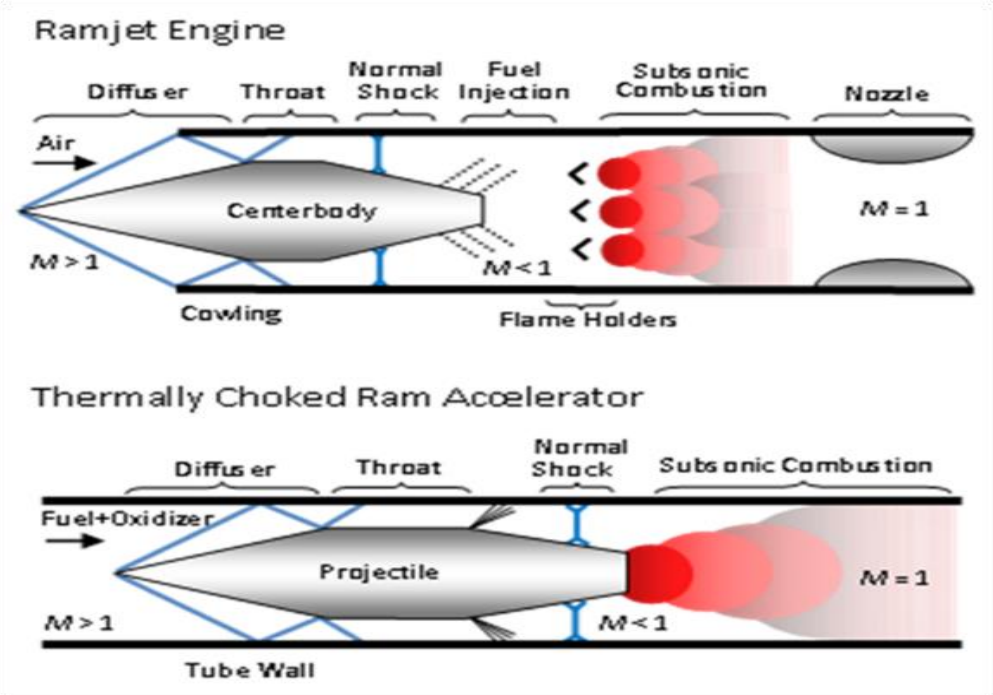

Figure 2. Conventional air-breathing ramjet (top) vs. thermally choked ram accelerator (bottom). Thermally choked ram accelerator propulsive cycle is similar to an air-breathing ramjet engine.

results in the unreacted propellant being compressed in the diffuser prior to its passage through the projectile throat, which coincides with the point of maximum projectile cross sectional area (Fig. 2). The primary variables that impact thrust production at any given projectile velocity are fill pressure, combustion energy release, and speed of sound of the unreacted propellant [5].

To characterize the performance of thermally choked ram accelerator (TCRA), a relation between non-dimensional thrust versus in-tube Mach can be established as shown in Fig. 3-left using non-dimensional heat release, Q, (described in Chapter 2) as a parameter. The theoretical thrust vs. Mach characteristics of TCRA propulsive mode predict quite well the multistage performance of a 38-mm-bore ram accelerator, as shown by the experimental velocity-distance data in Fig. 3-right, which supports the assumption that the end state of the propulsive cycle is indeed thermally choked [13]. In this particular experiment, an 80-g accelerator projectile was accelerated from 1.1 to 2.6 km/s in a 16-m-long test section. Note that the propellants used in this

multi-stage experiment (Fig. 3-right) were significantly diluted with inert gases such as N2, He, and/or excess H2 and CH4. The relatively large amount of diluent in these mixtures was empirically found to be necessary to prevent an "unstart" caused by the forward surging of a combustion driven shockwave. By developing a means that enabled operation in highly energetic propellants (via less dilution), the ram accelerator thrust could be nearly tripled using same projectile mass and fill pressure, resulting in much higher velocities in shorter barrels as indicated by the "Max Energetic Mixture" velocity-distance curve in Fig. 3-right.

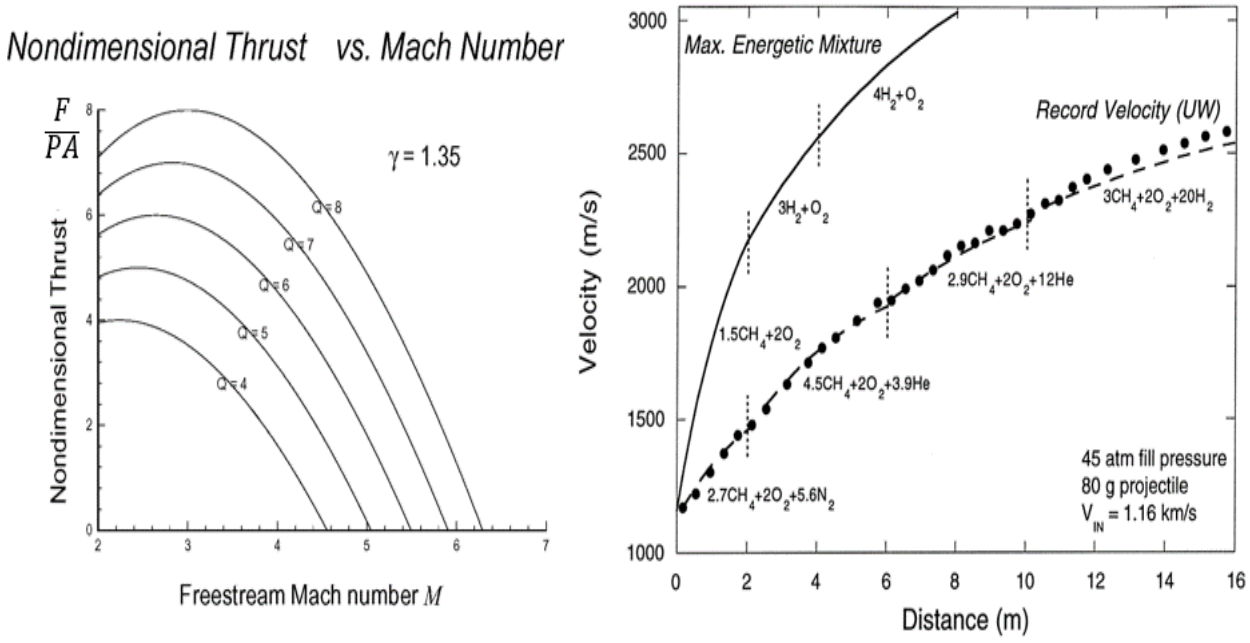

Figure 3. Non-dimensional thrust vs. in-tube Mach with non-dimensional heat release as a parameter (left). Acceleration at velocities over 2.6 km/s has been demonstrated in a 38-mm-bore tube using multiple stages. Operation with maximum energetic propellants would result in nearly three times the thrust (right).

Three main issues reduce the peak performance capabilities of the smooth bore ram accelerator. First, heat release of the propellant must be reduced to about 1/3 of which is available

(by adding inert diluents), which leads to peak thrust levels of only about 1/3 of the theoretical maximum in order to establish stable operation [13]. Experiments with propellants having larger heat release (less diluent) resulted in the undesirable situation of the combustion wave surging past the projectile, causing the diffuser to "unstart" [14].

Second, high acceleration requires high propellant-to-projectile density ratio, which results in high fill pressures for massive projectiles. Furthermore, these operating conditions result in extreme pressure spikes because the thermally choked ram accelerator propulsive mode generates pressure ratios of 10-20 times the fill pressure (depending on in-tube Mach). The resulting high pressure at the base of the projectile exerts significant loads on both the projectile and launch tube [13].

Third, peak velocity of thermally choked ram accelerator is significantly reduced when projectile fins are extended into the projectile throat (point of maximum projectile cross-section) region to better stabilize it as it moves through smooth bore tube [13]. Similar peak velocity reductions were observed in a rail-stabilized ram accelerator using axisymmetric projectiles [15]. Thus, fin-stabilized projectiles work best in a smooth bore tube while operating in the subdetonative velocity regime, but are not ideal for superdetonative velocities because of the intense heat transfer at the fin leading edges and corresponding fin drag. In contrast, rail-stabilized projectiles do not work as well in subdetonative velocity regime and are better suited for operation at superdetonative velocities [15].

To address these performance-limiting issues, the novel concept of baffled tube ram accelerator (BTRA) was first introduced by Higgins *et al*. [16, 17]. The sectional view of a representative BTRA design with an axisymmetric projectile is shown in Fig. 4. These annular baffles are like washers that protrude from the inner wall of the tube. These baffles bound chambers

that extend to the inner wall of the tube. Rails can be used to structurally reinforce baffles and provide continuous support for axisymmetric projectiles.

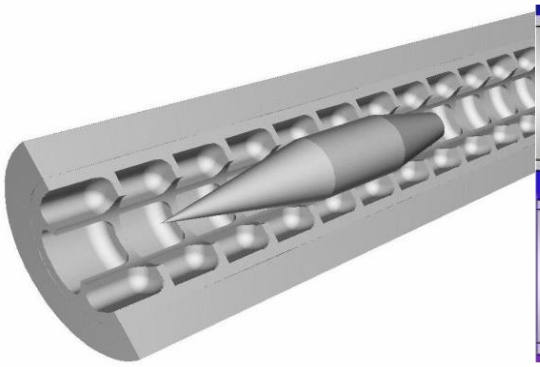

Figure 4. Section view of baffled tube ram accelerator with an axisymmetric projectile

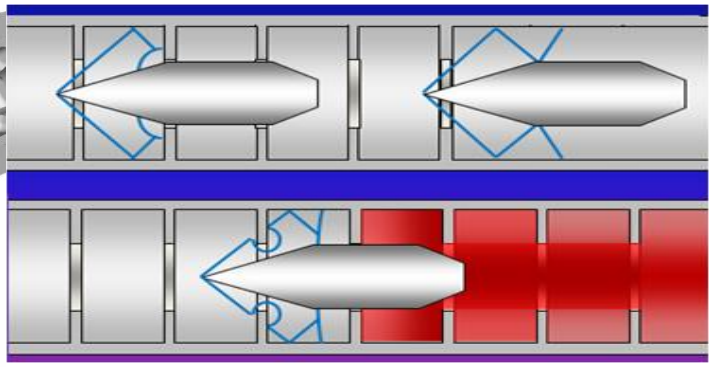

Figure 5. Propellant is ram compressed via area contraction and shockwaves in annular chamber around projectile shoulder and is ignited behind it.

Flow field phenomena arising as the projectile enters the baffled tube are illustrated in Fig. 5. As projectile enters the baffle opening and chamber at supersonic velocity, the projectile's shoulder seals the baffle and drives a shockwave into the baffle chamber. Since the shockwave axial velocity decays rapidly as it expands in the baffle chamber, the projectile can overtake the weakened shockwave before its shoulder encounters the next baffle. At the same time, the baffles behind the projectile shoulder block the forward propagation of combustion-driven pressure pulses. Thus the BTRA enables the projectile to act as a one-way valve that can ingest reactive premixed fuel and oxidizer past its throat while preventing the combustion-driven shockwave behind the projectile from surging ahead. Since these baffles prevent diffuser unstart, chamber-to-projectile diameter ratio can be increased to allow successful diffuser "start" at Mach numbers less than 2 while using more energetic propellant. For in-bore stability purposes when there are no rails, the cylindrical shoulder length of the projectile should span at least two baffles at all times.

The BTRA concept has the potential to triple the thrust performance of the conventional smooth bore ram accelerator (SBRA) while operating at same fill pressure and can reduce its minimum starting velocity (i.e., 0.7 km/s in smooth bore) by at least 25% [19]. In principle, this new ram accelerator propulsive mode can accelerate axisymmetric projectiles with masses ranging from grams to metric tons up to velocities of approximately 3 km/s. Its low starting velocity ability allows consideration of a wide range of pre-launcher technologies; which may greatly reduce the overall cost and operational complexities of hypervelocity launch systems for any application. In addition, the axisymmetric projectile geometry is favorable for railed-tube ram accelerators proposed for direct space launch applications with muzzle velocities greater than 4 km/s [20]. Thus, in addition to its high thrust potential at low Mach, the BTRA offers a significant advancement in ram accelerator technology for any application where axisymmetric projectiles are preferred.

Although the baffled tube concept offers a means to mitigate the three limitations of smooth bore ram accelerator operation previously discussed, the BTRA still has two main operational velocity limits. First, for a given projectile geometry and BTRA configuration, there is a minimum entrance Mach number that allows the projectile to pass supersonically throughout the length of the baffled tube. The conditions under which this occurs are complicated because the axisymmetric projectile unstarts; i.e., pushes a normal shock ahead of it, as its shoulder approaches each baffle, as shown in Fig. 5. The geometric parameters of BTRA must be such that the shockwave speed decays rapidly enough as it expands into the subsequent baffle chamber to allow the projectile shoulder to overtake the weakened shock before entering the next baffle. If the projectile Mach number is sufficiently high for a given BTRA configuration, then in this manner the projectile can remain started at the entrance to each baffle; i.e., maintain supersonic velocity with respect to the

quiescent propellant. Second, when the strength of the shockwave generated by the leading edge of the projectile shoulder is too strong as it just enters a chamber, it will initiate a detonation wave that travels forward and upstream through the next chamber, resulting in an unstart and cessation of thrust. A theoretical and computational modeling effort is underway to develop means to predict these two operational limits.

Optimizing the BTRA design requires knowledge of how the primary configuration parameters impact its minimum starting velocity and operating characteristics at high Mach number. The geometric variables considered here are: chamber-to-projectile diameter ratio, d_c/d_p, projectile geometry (nose cone angle and other details), baffle thickness, t_b, chamber width, w_c, and baffle inclination (Fig. 6). Baffle spacing is the distance between the front face of two adjacent baffles; i.e., $t_b + w_c$. Because of the complexity of the BTRA flow field, a transient computational fluid dynamic (CFD) modeling approach for a 38-mm-diameter ram accelerator projectile has been undertaken to determine the lowest Mach number with which it can pass supersonically through a section of baffled tube at steady velocity in inert propellant. To examine the influence of chemical

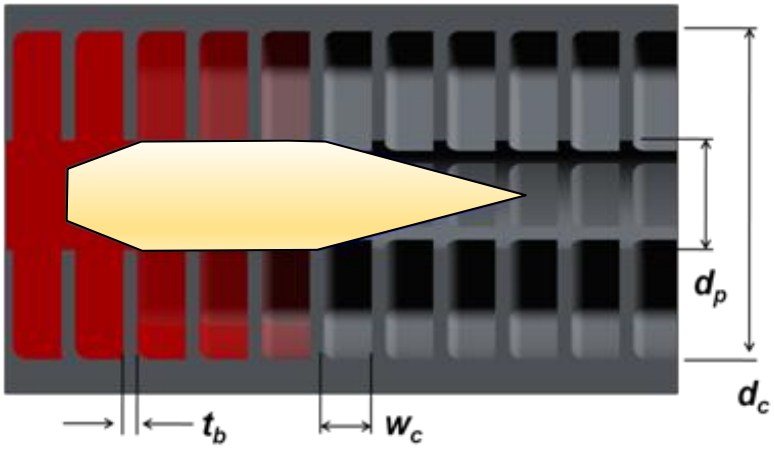

Figure 6. Baffled tube parameters include chamber-to-projectile diameter ratio (d_c/d_p), baffle thickness (t_b), and chamber width (w_c).

energy release on BTRA thrust performance for various baffle configurations, a two-step reaction model has been implemented in the CFD analysis. Details of this modeling approach for the development and implemenation of CFD models and results are presented in next few chapters.

One-dimensional flow theory of the smooth bore ram accelerator (SBRA) operating in the thermally choked propulsive mode and a correlation between non-dimensional thrust of SBRA and BTRA are briefly described here in Chapter 2. The development and implementation of CFD models using ANSYS Fluent computer software are described in Chapter 3. The important computational results of BTRA operating in inert gas and reactive mixtures are summarized in Chapter 4. The results presented in Chapter 4 are further discussed in Chapter 5. Lastly, the latest conclusions based on the results described in Chapters 4-5, future plans about the BTRA research and the potential areas of interest that need to be focused on are described in Chapter 6.

Chapter 2

Theory

Analyzing quasi-steady SBRA performance in the thermally choked ram accelerator propulsive mode can be achieved using one-dimensional flow assumptions and applying conservation of mass, momentum and energy to a control volume that contains the projectile. Quasi-steady and unsteady one-dimensional modeling of the thermally choked ram accelerator in a SBRA showed that in the Mach range of 3 to 4, thrust estimates of the unsteady one-dimensional model agree with the experimental results [21]. Standard quasi-steady model for simplicity is briefly described in this section and the details of unsteady one-dimensional modeling are shown by Bundy *et al*. and Bengherbia [22, 23].

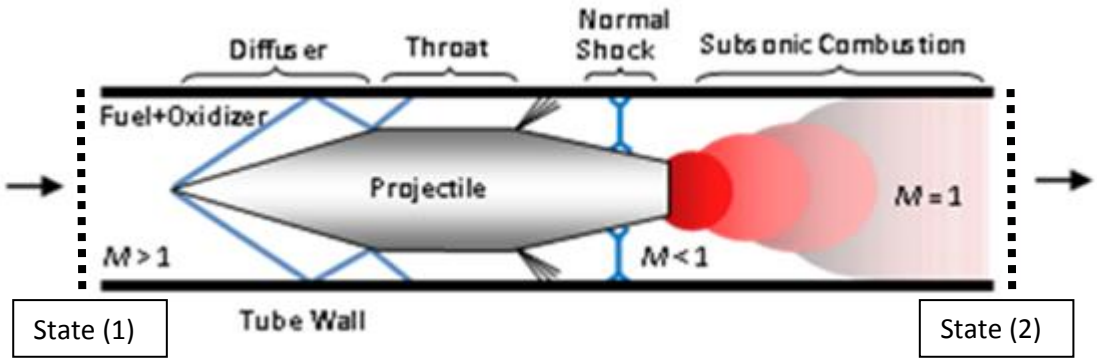

Figure 7. Smooth bore ram accelerator flow field in projectile's frame of reference. Supersonic propellant enters the control volume at State (1) ahead of the projectile. Heat release occurs inside control volume and flow is thermally choked downstream (M_2=1) and exists the control volume at State (2).

The one-dimensional quasi-steady flow field model for the thermally choked ram accelerator propulsive mode operating in a SBRA can be described in the context of a control volume drawn around the projectile as shown in Fig. 7. In this frame of reference, unreacted propellant supersonically enters the control volume at State (1). Then, the area contraction of the projectile diffuser (nosecone) slows down the flow velocity relative to the projectile until it passes through the minimum flow area at the throat. The flow must be supersonic in the throat region for the projectile diffuser to be "started." A normal shockwave is subsequently stabilized on the aftbody of the projectile, which renders the flow subsonic. Then, combustion occurs at the base of the projectile which adds heat to the subsonic flow and causes the static temperature and local flow Mach to increase. The local Mach increases until it reaches M = 1, which results in thermally choking of the flow at the control volume exit, denoted as State (2). Conservation of mass, momentum and energy equations are applied between State (1) and State (2) as described below.

Conservation of mass in Eq. 1 requires the mass flux entering and exiting the control volume to be the same where ρ is the flow density, A is the cross sectional area of SBRA and u is the one-dimensional flow velocity;

$$\rho_1 A_1 u_1 = \rho_2 A_2 u_2 \qquad (Eq. 1)$$

Conservation of momentum in Eq. 2 requires the difference between the sum of momentum flux and static pressure entering and exiting the control volume to be equal to the force F applied to the projectile;

$$P_1 A_1 + \rho_1 A_1 {u_1}^2 + F = P_2 A_2 + \rho_2 A_2 {u_2}^2 \qquad (Eq. 2)$$

Conservation of energy in Eq. 3 requires the sum of energy flux entering the control volume and the heat release due to chemical reaction to be equal to the energy flux exiting the

control volume where h is the sensible enthalpy is and Δq is the heat release due to chemical reaction;

$$h_1 + \frac{1}{2}{u_1}^2 + \Delta q = h_2 + \frac{1}{2}{u_2}^2 \qquad (Eq.3)$$

The ideal gas Equation of State (Eq. 4), speed of sound (Eq. 5), enthalpy for calorically perfect gas (Eq. 6) and Mach (Eq. 7) are sufficient to close this set of equations to derive a thrust-Mach relationship for the TCRA. New variables in Eqs. 4-6 are; R is gas constant for the mixture (different for propellant entering and combustion products leaving control volume), T is the temperature, a is the speed of sound, γ is the ratio of specific heats, and C_p is the specific heat at constant pressure;

$$P = \rho RT \qquad (Eq.4)$$

$$a = \sqrt{\gamma RT} \qquad (Eq.5)$$

$$h = h(T) \qquad (Eq.6)$$

$$M = \frac{u}{a} \qquad (Eq.7)$$

One can rewrite conservation of momentum (Eq. 2) using Eqs. 1, 4, 5 and 7 in terms of pressure ratio P_2/P_1, density ratio ρ_2/ρ_1, and non-dimensional thrust $F/(P_1A)$ as shown here;

$$1 + {M_1}^2{a_1}^2\,\frac{\rho_1}{P_1} + \frac{F}{P_1A_1} = {M_2}^2{a_2}^2\,\frac{\rho_2}{P_1} + \frac{P_2}{P_1} \qquad (Eq.8)$$

$$\frac{P_2}{P_1} = \frac{M_1}{M_2}\sqrt{\frac{\gamma_1 R_2 T_2}{\gamma_2 R_1 T_1}} \qquad (Eq.9)$$

Introducing a non-dimensional heat release parameter (Q) and using Eqs. 5-7 to rewrite conservation of energy (Eq. 3) in terms of static temperature ratio T_2/T_1, constant pressure heat capacity ratio C_{p2}/C_{p1}, and non-dimensional enthalpy $h/(C_pT)$, results in the following;

$$Q \stackrel{\text{def}}{=} \frac{\Delta q}{C_{p_1} T_1} \qquad (Eq.10)$$

$$\frac{h_1}{C_{p_1} T_1} + \frac{\gamma_1 - 1}{2} {M_1}^2 + Q = \frac{h_2}{C_{p_1} T_1} + \frac{\gamma_2 - 1}{2} {M_2}^2 \frac{C_{p_2} T_2}{C_{p_1} T_1} \qquad (Eq.11)$$

$$\frac{T_2}{T_1} = \frac{C_{p_1}}{C_{p_2}} \left(\frac{\frac{h_1}{C_{p_1} T_1} + \frac{\gamma_1 - 1}{2} {M_1}^2 + Q}{\frac{h_2}{C_{p_1} T_1} + \frac{\gamma_2 - 1}{2} {M_2}^2} \right) \qquad (Eq.12)$$

Defining I_{SBRA} to be non-dimensional thrust (Eq. 13) and rewriting Eq. 8 using Eqs. 9 and 12 yields the following global quasi-steady thrust equation for the ram accelerator operating in any propulsive mode in a smooth bore tube;

$$I_{SBRA} \stackrel{\text{def}}{=} \frac{F}{P_1 A_1} \qquad (Eq.13)$$

$$I_{SBRA} = \frac{M_1 \gamma_1}{M_2 \gamma_2} \left(1 + \gamma_2 {M_2}^2\right) \sqrt{\left(\frac{\gamma_2 - 1}{\gamma_1 - 1}\right) \left(\frac{\frac{h_1}{C_{p_1} T_1} + \frac{\gamma_1 - 1}{2} {M_1}^2 + Q}{\frac{h_2}{C_{p_1} T_1} + \frac{\gamma_2 - 1}{2} {M_2}^2} \right)} - \left(1 + \gamma_1 {M_1}^2\right) \qquad (Eq.14)$$

If flow is thermally choked at State (2); i.e., $M_2 = 1$, then Eq. 14 can be rewritten as a non-dimensional thrust equation for the thermally choked ram accelerator propulsive mode operating in a SBRA as shown here;

$$I_{SBRA} = \frac{M_1\gamma_1}{\gamma_2}(1+\gamma_2)\sqrt{\left(\frac{\gamma_2-1}{\gamma_1-1}\right)\left(\frac{\frac{h_1}{C_{p_1}T_1}+\frac{\gamma_1-1}{2}{M_1}^2+Q}{\frac{h_2}{C_{p_1}T_1}+\frac{\gamma_2-1}{2}}\right)-\left(1+\gamma_1{M_1}^2\right)} \qquad (Eq.15)$$

Knowlen *et al.* [19] showed that non-dimensional thrust for the thermally choked ram accelerator propulsive mode operating in a SBRA can be correlated to the same propulsive mode operating in the BTRA. This required the introduction of a geometrical constant, φ, that equates available baffle chamber volume for a given chamber-to-projectile diameter ratio, d_c/d_p, baffle thickness, t_b, chamber width, w_c, chamber volume, V_c, and baffle volume, V_b, to an equivalent volume in SBRA configuration with effective bore diameter d_{eff}. This constant φ is illustrated in Fig. 8 and defined in Eq. 16.

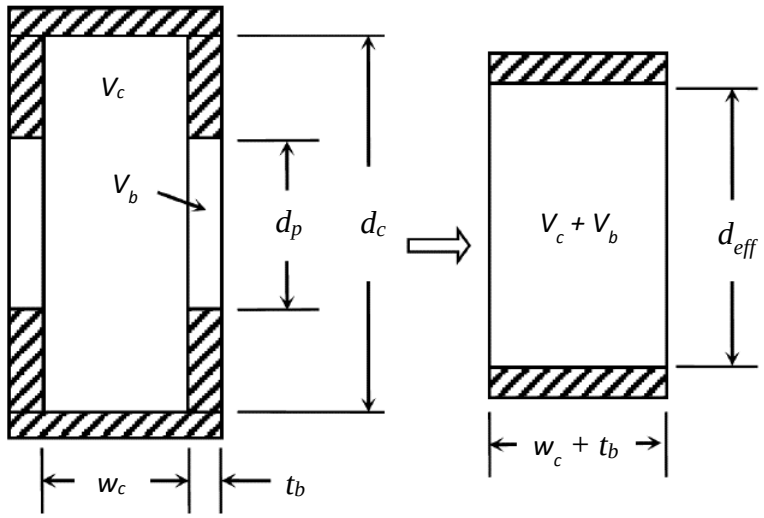

Figure 8. Geometrical constant, φ, is a ratio that describes available volume of BTRA configuration to an equivalent volume in SBRA configuration.

$$\varphi = \frac{1+\left(\frac{w_c}{t_b}\right)}{1+\left(\frac{w_c}{t_b}\right)\left(\frac{d_c}{d_p}\right)^2} \qquad (Eq.16)$$

The relation below, Eq. 17, correlates the non-dimensional thrust of one-dimensional quasi-steady SBRA to BTRA configuration [19].

$$I_{BTRA} = \frac{I_{SBRA}}{\varphi} \qquad (Eq. 17)$$

Baffle drag refers to the momentum loss of the combustion products as they move in the direction of the projectile through the baffle chambers, which diverts some of the momentum available for accelerating the projectile. Fully accounting for baffle drag in developing a quasi-one-dimensional model for the thrust-Mach performance characteristics of the BTRA is an ongoing theoretical and experimental effort [24]. Momentum and energy conservation equations in projectile frame of reference can be modified to reflect the effect of baffle drag. Momentum conservation equation (Eq. 2) can be modified into Eq. 18, in which *D* represents baffle drag. Also, the energy conservation equation (Eq. 3) can be modified into Eq. 19 to yield a new non-dimensional thrust shown in Eq. 20 [19, 25].

$$P_1A_1 + \rho_1A_1{u_1}^2 + F - D = P_2A_2 + \rho_2A_2{u_2}^2 \qquad (Eq. 18)$$

$$\rho_1A_1u_1\left(h_1 + \frac{1}{2}{u_1}^2 + \Delta q\right) - Du_1 = \rho_2A_2u_2\left(h_2 + \frac{1}{2}{u_2}^2\right) \qquad (Eq. 19)$$

$$I_{BTRA} = \frac{M_1\gamma_1}{\gamma_2}(1+\gamma_2)\sqrt{\left(\frac{\gamma_2-1}{\gamma_1-1}\right)\left(\frac{\frac{h_1}{C_{p_1}T_1} + \frac{\gamma_1-1}{2}{M_1}^2 + Q - \frac{D(\gamma_1-1)}{P_1A_1\gamma_1}}{\frac{h_2}{C_{p_1}T_1} + \frac{\gamma_2-1}{2}}\right)} - \left(1+\gamma_1{M_1}^2\right) - \frac{D}{P_1A_1} \qquad (Eq. 20)$$

By introducing baffle projected area as the surface drag acts upon, one can introduce a definition for the drag, as shown in Eq. 21, in which $A_{p,b}$ is the projected baffle surface area, C_d is the baffle drag coefficient and n_c is the number of chambers that the combustion zone actively affects [24].

$$D = C_d \rho_1 A_{p,b} n_c |u_1 - u_2|(u_1 - u_2) \qquad (Eq. 21)$$

Determining the numerical value for C_d is one of the objectives of ongoing theoretical, computational and experimental efforts at University of Washington.

Chapter 3

Development and Implementation of CFD Models

Transient CFD modeling of the BTRA in laboratory frame of reference was carried out with ANSYS Fluent computer software [26]. As an initial goal, CFD modeling was applied to determine the minimum entrance Mach number in inert propellant that allowed the projectile to pass supersonically throughout baffled tubes having different baffle geometries. After the completion of this study, a transient CFD model of reacting flows using 1-step and 2-step reaction mechanism chemistry was developed to explore the thrust characteristics of the BTRA. Means to numerically ignite the propellant and determine if the combustion could be sustained as the projectile passed through the baffles were developed. In spite of the preliminary nature of this reactive flow modeling and its intense computational demands, the numerical experiments carried out to date have provided insight on how different BTRA geometries impact projectile thrust at various in-tube Mach numbers. In this section computational domain setup and mesh sizing are discussed.

3. A: Designing computational domains

Two general computational domains were created to address the goals of this research study. To determine the minimum starting entrance Mach number in inert propellant, a computational domain for an axisymmetric model (with a short-tailed projectile) was created as shown in Fig. 9a. To examine the performance of the baffled tube ram accelerator in reactive flow, the model shown in Fig. 9b was utilized (both short- and long-tailed projectiles were included in this part of the study). Both of these computational models had multiple domains with significantly different characteristics. The projectile was surrounded by a rigid domain which moved with the projectile at constant velocity. There were several deforming domains ahead and behind the projectile which were attached to the rigid domain. In Fig. 9a, deforming domain (1) was stretched

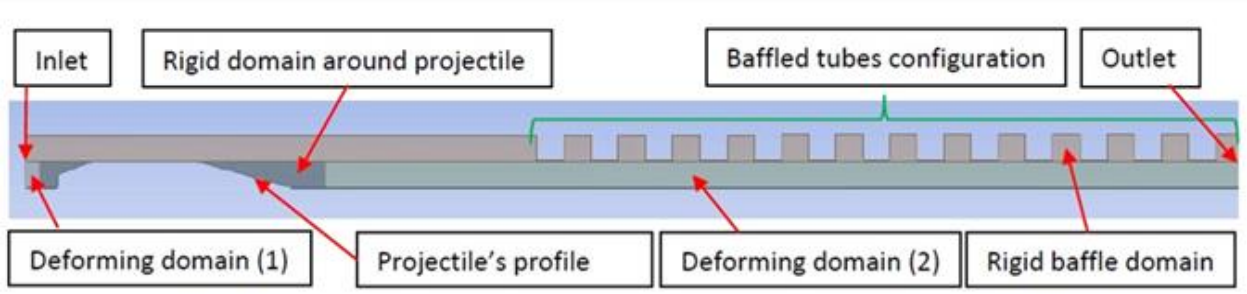

(a)

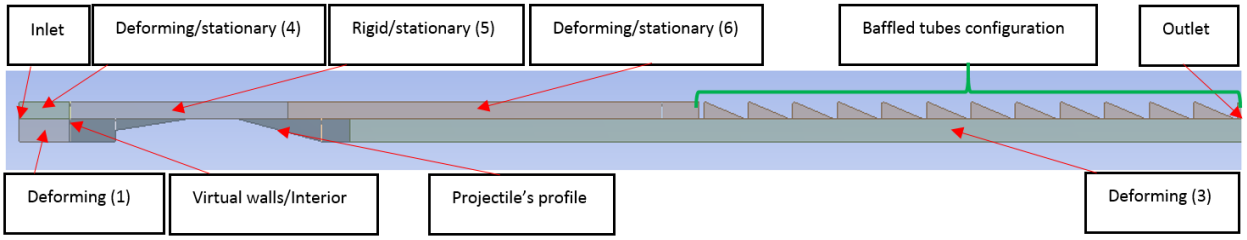

(b)

Figure 9. (a) Axisymmetric computational domain for inert flow modeling contains a smooth bore tube segment upstream of baffled tube section with discrete chamber volumes having rectangular baffles. (b) Axisymmetric computational domain for reacting flow contains a smooth bore tube segment upstream of baffled segment with discrete chamber volumes having triangular baffles (and other geometries).

and deforming domain (2) was compressed as the rigid domain and projectile moved from left to right. The rigid baffle domain above the deforming domains (1) and (2) remained stationary in laboratory reference frame and the rigid domain around the projectile remained stationary in the projectile reference frame.

Similarly, in Fig. 9b domains (1) and (4) were stretched and domains (3) and (6) were compressed as the rigid domain and projectile moved from left to right. Domains (4) and (6) remained stationary when rigid domain (5) stopped moving before the baffled tube region began. The domain (6) was initially deformed until the nose of the projectile reached the baffled tube region and then domain (6) remained stationary relative to the laboratory frame of reference. Rigid domain (5) above the projectile initially remained stationary relative to the projectile until just before it entered baffle tube section, and then domain (5) remained stationary relative to laboratory frame of reference. The purpose of rigid domain (5) was to provide a uniform cell size domain around the projectile for the flow field to develop before it entered the baffled region.

Using the computational domain for reacting flow (Fig. 9b), propellant ignition was initiated with a virtual wall that was positioned a fixed distance behind the projectile base and moved with it through the smooth-bore section. The virtual wall generated a high pressure and temperature region behind the projectile to promote propellant ignition in a manner analogous to using an obturating piston for starting the ram accelerator [27]. Once combustion was robustly initiated, the virtual wall was removed (by changing its boundary type from wall to interior) [28]. This allowed the combustion process to be established at the projectile base in a repeatable manner before it entered the baffled tube section.

3. B: General settings of flow solver in inert gas

Optimization of the CFD models was improved by using a dynamic layering mesh method [29]. The dynamic layering mesh method allowed structured cells to be stretched and compressed based on a split and collapse factor. A User-Defined Function (UDF) assigned a constant velocity to the projectile, rigid domains, and to the corresponding boundaries that were subjected to stretching or compressing [30].

The main setup parameters for inert gas CFD models were the followings [29, 31]; (see Appendix C for complete Fluent solver setup)

1. Transient-implicit-density-based solver used for axisymmetric and three-dimensional models.
2. Shear-Stress Transport (SST) κ-ω viscous model used with compressibility effect as turbulent model.
3. Implicit-advection upstream splitting method (AUSM) flux solver with first order upwind transient formulation along with following spatial discretization: least square cell based gradient, second order upwind flow, first order upwind turbulent kinetic energy and first order upwind specific dissipation rate.
4. Ideal gas equation of state used for air at an initial fill temperature of 300 K.
5. Walls of the projectile, tube and baffles were assigned to be no-slip adiabatic surfaces with 0.5 surface roughness.
6. Pressure-inlet was at 1 atm and supersonic/initial pressure at 1 atm normal to boundary with 5% turbulent intensity, turbulent viscosity ratio at 10 and at constant 300 K fill temperature.

7. Pressure-outlet at 1 atm static pressure normal to boundary with 5% turbulent intensity, turbulent viscosity ratio at 10 and at constant 300 K backflow fill temperature.

3. C: General setting of flow solver in reactive mixture

The main setup parameters for combustion CFD models were the followings [29, 31]; (see Appendix C for complete Fluent solver setup)

1. Transient-implicit-density-based solver used for axisymmetric models.
2. Shear-Stress Transport (SST) κ-ω viscous model used with compressibility effect as turbulent model.
3. Implicit-advection upstream splitting method (AUSM) flux solver with first order upwind transient formulation along with following spatial discretization: least square cell based gradient, second order upwind flow, first order upwind turbulent kinetic energy and first order upwind specific dissipation rate.
4. Ideal gas equation of state was used for methane-oxygen mixtures with initial fill temperature of 300 K or 700 K.
5. Species transport model with volumetric reaction incorporated 1- or 2-step methane-oxygen mechanisms with a hybrid finite-rate/eddy-dissipation turbulence-chemistry interaction without third-body efficiencies and specific heat mixing-law, constant thermal conductivity, constant viscosity and constant dilute approximation mass diffusivity.
6. Walls of the projectile, tube and baffles were assigned to be no-slip adiabatic surfaces with 0.5 surface roughness. In some cases, the base of the projectile was assigned a very high temperature (above 3000 K) to promote combustion.

7. Pressure-inlet and pressure-outlet were the same as inert gas models except at 5 atm and had molar ratios of 1CH4+2O2 (stoichiometric) or 2CH4+2O2 with trace amounts of CO, CO2, H2O (less than 1%) added to facilitate initiation of combustion.

3. D: General mesh settings

Meshing the computational domains was done in the following manner [31, 32]; (see Appendix B for complete meshing description)

1. General meshing size was set to have fine mesh with high smoothing on all curvatures (1-mm-maximum cell size).

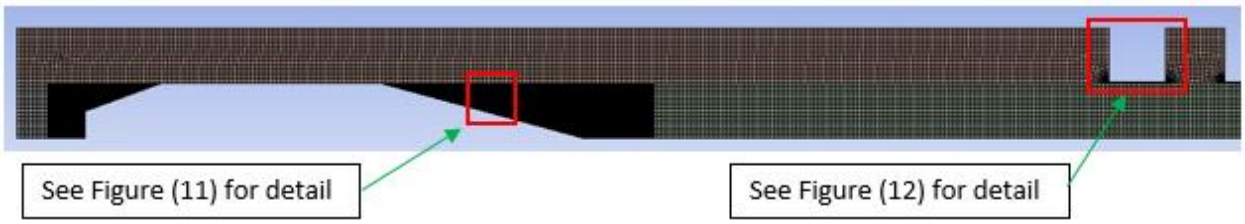

Figure 10. General mesh on the axisymmetric model used for inert gas analysis.

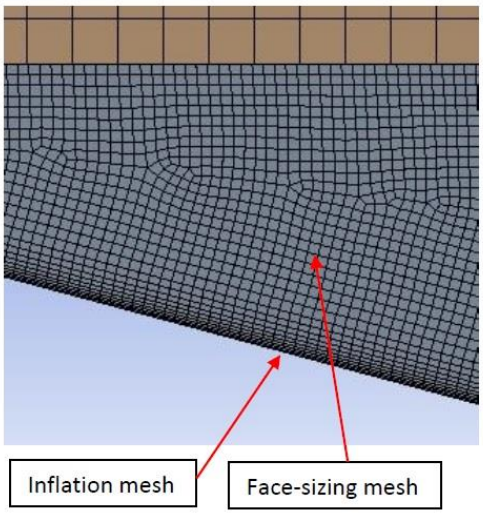

Figure 11. Projectile mesh detail.

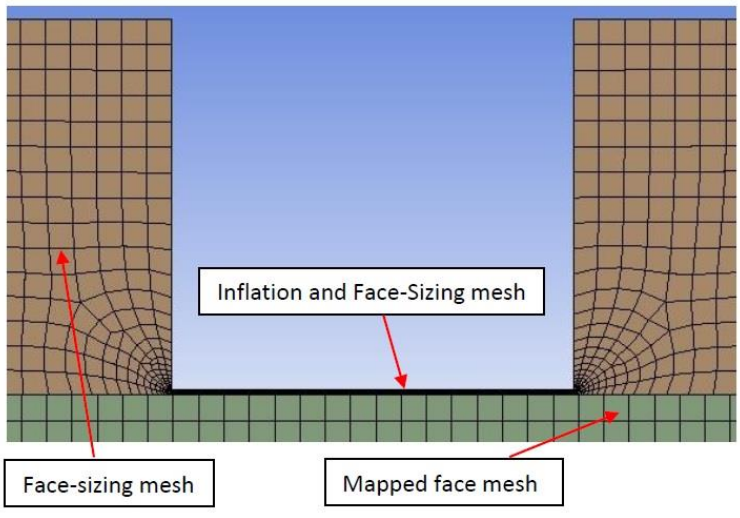

Figure 12. Baffled tube wall mesh detail.

2. In inert gas analysis (Fig. 10), the inflation method was used to add layers of cell on surface of the projectile and on minimum gap between shoulder of the projectile and baffle walls (Figs. 11 and 12), which was 0.5 mm, and also Y+ adaptation [31] was used to refine these regions (25-40 µm minimum cell size). For combustion modeling, 0.1-mm cell sizes were applied to the rigid regions around the projectile and above it to provide a uniform region for propellant ignition behind the projectile (Fig. 13).
3. Mapped face meshing was used on deforming regions ahead and behind the projectile to assure structured quadrilateral cells split and collapse accordingly.
4. Face-sizing method in rigid domains was used and their sizes were adjusted to reduce skewness between the cells and increase orthogonal and element qualities (Figs. 14 and 15).

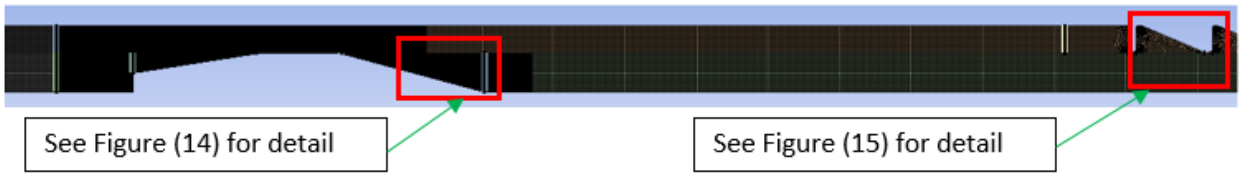

Figure 13. General mesh on the axisymmetric combustion model.

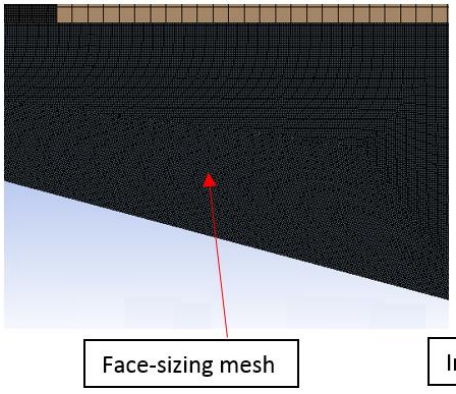

Figure 14. Projectile mesh detail.

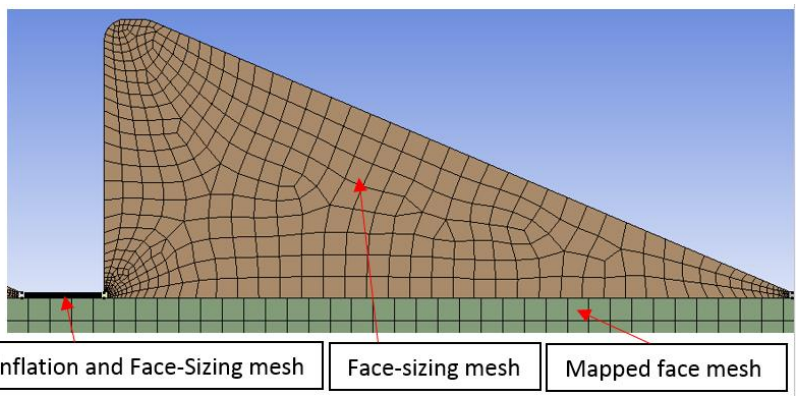

Figure 15. Baffled tube wall mesh detail.

The projectile dimensions used in these simulations were; 165-mm overall length, 36.1-mm-maximum cross section diameter, and 15° cone half angle. The "short-tailed" projectile had 72.7-mm-long cylindrical shoulder (throat region) and 20° rear cone taper down to a 17.8-mm-diameter bluff base. The "long-tailed" projectile had 39.5-mm-long cylindrical shoulder and 8.9° rear cone taper down to a 17.8-mm-diameter bluff base.

In inert gas analyses, baffle spacing and baffle thickness were varied while keeping constant the bore diameter and chamber diameter at 37.1 mm and 72.1 mm, respectively, which resulted in a chamber-to-projectile diameter ratio of 2 with a clearance gap of 0.5 mm between the projectile shoulder and baffle bore. In combustion analysis, chamber-to-projectile diameter ratios of 2 and $\sqrt{3}$ (maintained same projectile shoulder diameter) with the same clearance gap of 0.5 mm between projectile shoulder and baffle bore were investigated. The complete description of design and meshing inputs used in this research study are provided in Appendix A (Fluent – Design inputs) and Appendix B (Fluent – Meshing inputs).

Chapter 4

Computational Results

The CFD analyses in sections A & B were divided into inert gas (air) and reactive flow, respectively. Some of the key BTRA parameters (Fig. 6) investigated in inert gas were baffle thickness, t_b, chamber width, w_c, baffle spacing, (t_b + w_c) and Mach number, M, with the short-tailed projectile. Examined in inert flow conditions were the variations in projectile drag coefficient as it passed through the baffle chambers and the corresponding wall pressure as a function of position and time. The primary variables investigated in the reactive flow section included projectile in-tube Mach number, baffle inclination angle, fuel equivalence ratio, and projectile geometry. The significant findings of these studies are presented here.

4. A: Inert Gas Analysis

The first objective for the CFD modeling was to determine the minimum projectile entrance Mach number that allowed the diffuser to start for the given chamber-to-projectile diameter ratio of 2 in inert gas (air). For the flow area contraction at the projectile shoulder ($1-(d_p/d_c)^2 = 0.75$) in a smooth bore tube, ideal compressible flow calculations predict that the flow will be sonic with respect to the projectile shoulder at an in-tube Mach number of $M = 1.66$, which corresponds to 570 m/s in room temperature air [33]. Initial CFD results, with baffle thickness $t_b = 3.81$ mm and chamber width $w_c = 30.6$ mm, found that the projectile would unstart when entering the baffled tube section at a Mach number of $M = 1.59$ (545 m/s), and remain started at entrance Mach of $M = 1.75$ (600 m/s). Thus at entrance Mach numbers 5% greater than the theoretical minimum, the

total pressure losses due to shocks and viscous effects were not sufficiently high to cause the projectile to unstart. Further refinement of the minimum starting entrance Mach number was not pursued in this study because it required a longer computational domain to determine if projectile would eventually unstart. Shown in Figs. 16 and 17 are the flow field static pressure contours in the 0.1-2.0 atm range, for projectiles traveling at 545 and 600 m/s, respectively. Upon completing its transit through the baffled tube section, the projectile traveling at 545 m/s (Fig. 16) was pushing a shockwave ahead of its throat and was thus unstarted, as to be expected at velocities below the minimum predicted by one-dimensional flow theory. Whereas in the case with a projectile velocity

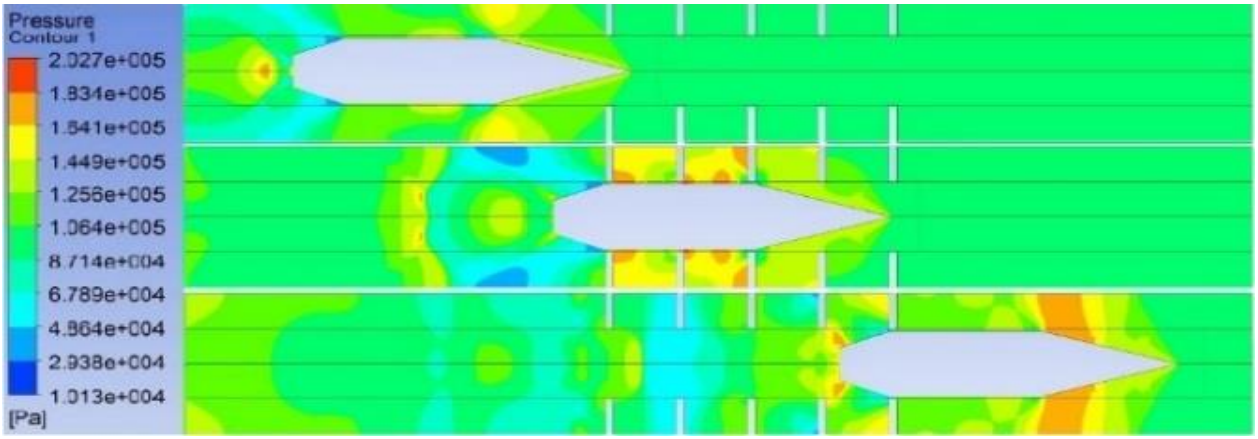

Figure 16. Flow pattern does not recover after passing through baffles at 545 m/s.

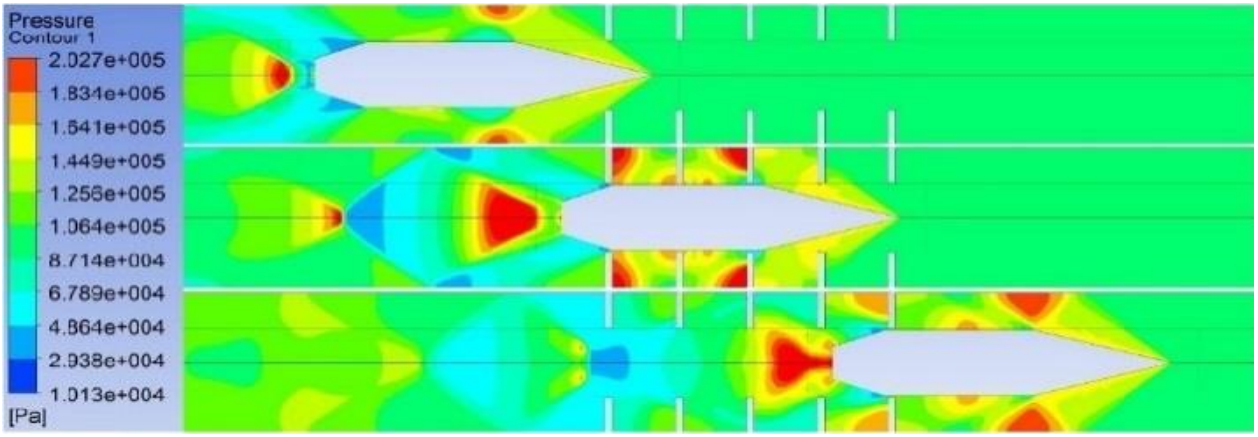

Figure 17. Flow pattern almost completely recover after passing through baffles at 600 m/s.

of 600 m/s, which is 5% above the minimum theoretical velocity, the flow remained supersonic with respect to the projectile while it passed through the baffles, which is a necessary condition for successful baffled tube ram accelerator operation with reactive propellants. At all entrance Mach numbers investigated above $M = 1.75$, the projectile remained started. The start – no start results of computations for various entrance Mach numbers mentioned here (Cases 1-3) and other BTRA configurations are listed in Table 1.

Table 1 CFD results for inert gas and various BTRA configurations.

Case	Baffle Thickness (mm)	Chamber Width (mm)	Baffle Spacing (mm)	Area Contraction	Entrance Mach	Entrance Velocity (m/s)	Start (Yes/No)
1	3.81	30.6	34.4	0.75	1.59	545	No
2	3.81	30.6	34.4	0.75	1.75	600	Yes
3	3.81	30.6	34.4	0.75	2.50	857	Yes
4	7.62	24.9	32.5	0.75	1.75	600	Yes
5	11.4	19.2	30.6	0.75	1.75	600	Yes
6	15.2	13.5	28.7	0.75	1.75	600	Yes
7	19.1	7.77	26.8	0.75	1.75	600	No
8	19.1	19.2	38.3	0.75	1.75	600	Yes
9	9.40	30.6	40.0	0.75	2.62	900	Yes
10	11.4	19.2	30.6	0.84	1.52	600	Yes
11	19.1	7.77	26.8	0.84	1.52	600	No

The next step in inert gas CFD modeling was to examine how baffle thickness, chamber width, and baffle spacing affect the projectile starting characteristics at the minimum entrance Mach number ($M = 1.75$). Results from CFD modeling of Cases 4−6 in Table 1 indicated that supersonic flow with respect to the projectile was readily maintained as the baffle thickness increased by a factor of 4 and chamber width decreased by ~130% with respect to the reference

geometry of Cases 1-3. The flow field pressure contours of Cases 5 and 6 are shown in Fig. 18a and 18b respectively.

The brief period of unstart in the thinner baffle case, (Fig. 18a) as the projectile shoulder passes through the baffle, results in a relatively weak forward moving shock that is quickly overtaken as the projectile exits the baffle. Whereas there is a stronger shock pushed ahead of the

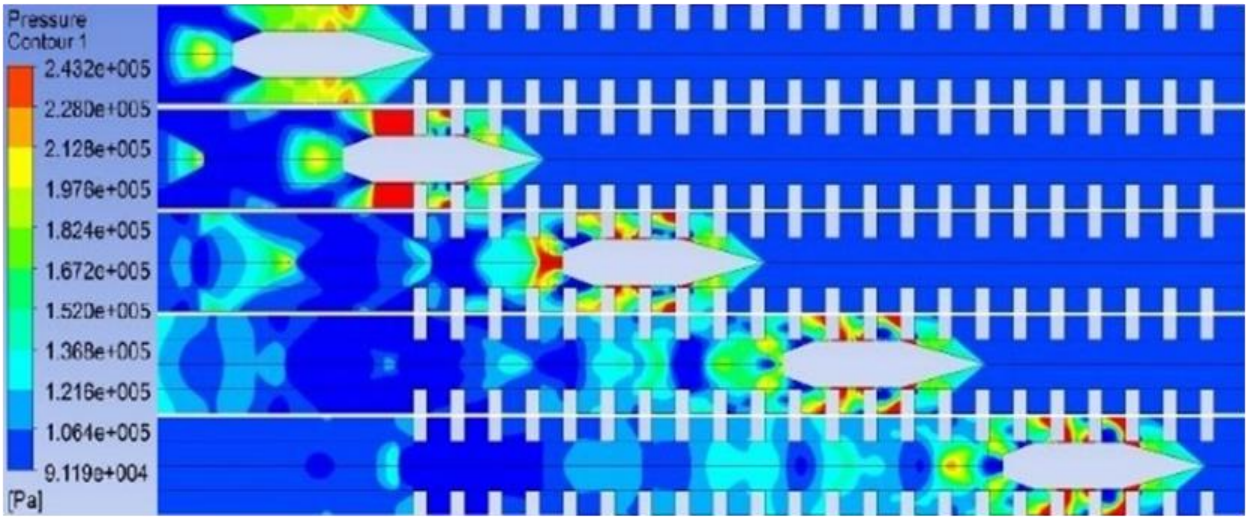

(a)

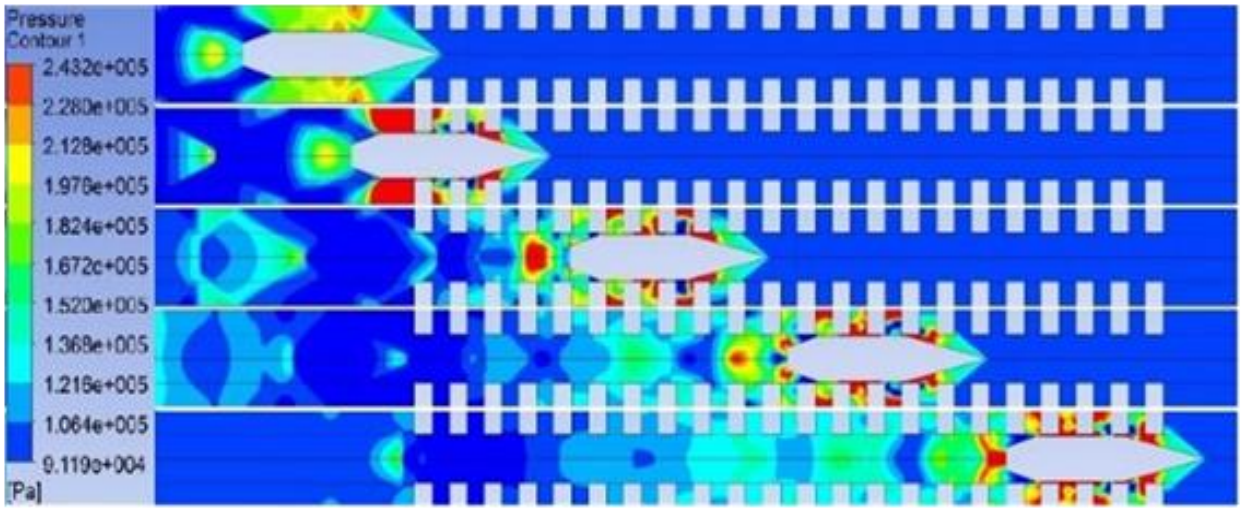

(b)

Figure 18. BTRA pressure field contours for Case 5 (a) and Case 6 (b) parameters listed in Table 1. Projectile enters BTRA at *M* = 1.75 and remains started in both cases shown here.

projectile shoulder as it exits a thickened baffle (Fig. 18b) which the projectile never quite overtakes, yet this shock does not jump out ahead of the projectile nosecone within the domain modeled here. Thus Case 6 is considered to be on the boundary of the minimum entrance Mach number envelope for this BTRA configuration.

In Case 7, where the baffle thickness was increased ~25% and chamber width reduced by ~60% with respect to Case 6 (Table 1), the shock driven by the passage of the projectile shoulder through the baffle overran the nosecone, resulting in an unstart after passing through about 10 baffles, as shown in Fig. 19a. Beyond this point, if there is no change in BTRA parameters, the projectile remains unstarted as it pushes the shockwave ahead of it.

In Case 8, where the chamber width was increased by ~150% while keeping the baffle thickness the same as in Case 7 (Table 1), the CFD modeling showed that the projectile would remain started (see Fig. 19b) at the same Mach number (M = 1.75) where it was unstarted before. This indicates that the projectile can recover from an unstart after its passage through a relatively thick baffle if the baffle spacing is such that the adjacent chamber exceeds a minimum width.

The maximum baffle thickness that allows the projectile to remain started after it exits the baffle opening has not yet been determined for the chamber-to-projectile diameter ratio of this configuration. Note that for a given chamber width, increasing projectile Mach number and/or chamber diameter will also enable the projectile to recover from an unstart after its passage through a "thick" baffle if the baffle spacing is such that the adjacent chamber exceeds a minimum width (Cases 10 and 11).

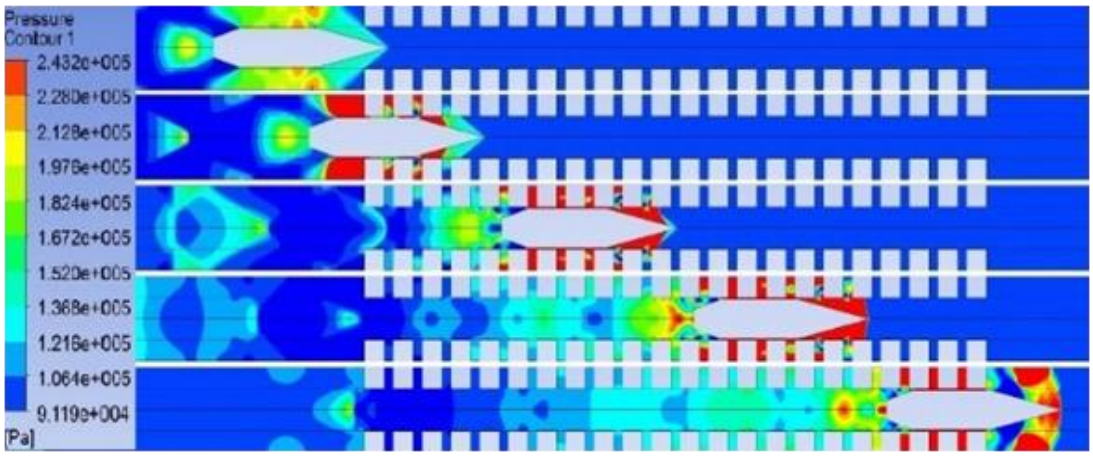

(a)

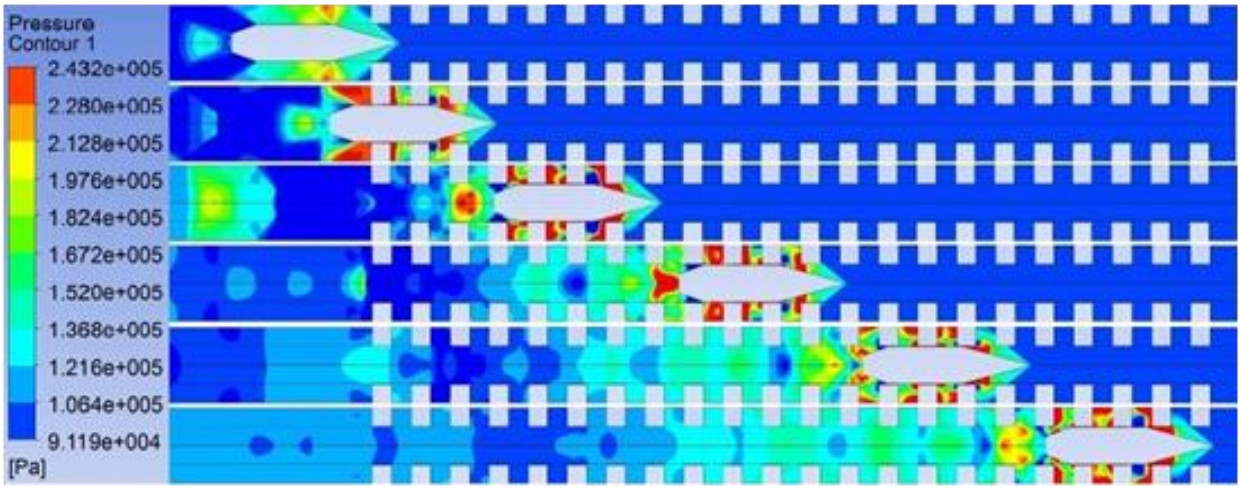

(b)

Figure 19. BTRA pressure field contours for Case 7 (a) showing an unstart and Case 8 (b) showing the projectile remains started at *M* = 1.75 with same baffle thickness tb (see Table 1).

The envelope boundaries of entrance Mach vs. baffle thickness-to-chamber width (t_b/w_c) ratio and baffle chamber-to-projectile diameter ratio (d_c/d_p) can be determined by this CFD modeling approach, which is a subject of future investigations. The transient CFD modeling was applied to a three-dimensional domain to explore the more complicated baffled-tube configurations of the experimental apparatus [19]. The new baffled tube design (Fig. 20) had tapered rails that were

staggered at 45° in adjacent chambers between the baffles. It was shown numerically by Knowlen *et al.* [19] that this baffled tube configuration enhanced structural rigidity and could withstand higher pressure load than the axisymmetric configuration.

The corresponding CFD domain for this three-dimensional baffled-tube with 1/8 symmetry is shown in Fig. 21. There is a smooth bore section of tube prior to the baffles to allow the CFD calculations to establish the axisymmetric supersonic flow field before the projectile enters the baffled tube section. Static pressure contours of the projectile as it passes through the 3-D baffled tube (from left to right) are shown in Fig. 22. Even though the details of the pressure field within the baffle chambers are significantly different, CFD results indicate that the projectile will be able to transit this baffled-tube configuration at $M = 1.75$ without unstarting. Note that experiments have operated at Mach numbers as low as $M = 2.1$ in this BTRA configuration [19].

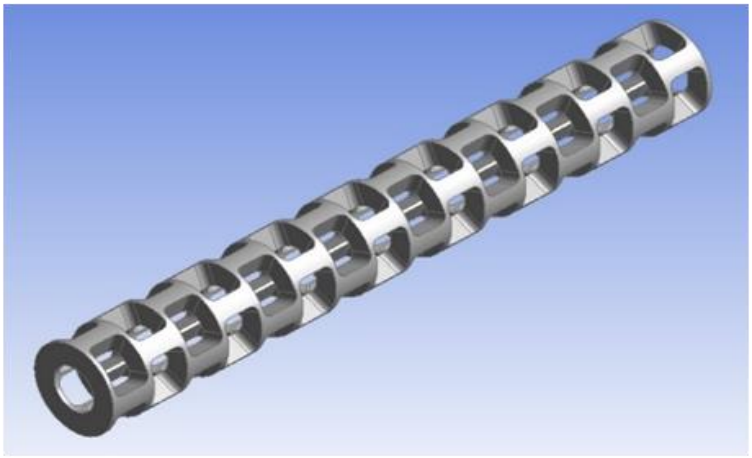

Figure 20. Experimental BTRA configuration with tapered rails in between baffles.

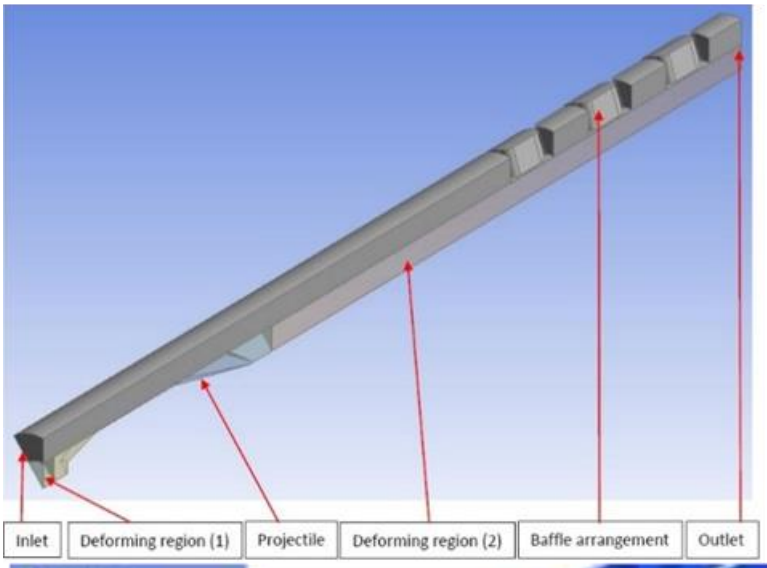

Figure 21. Experimental BTRA with 1/8 symmetry in 3-D computational domain.

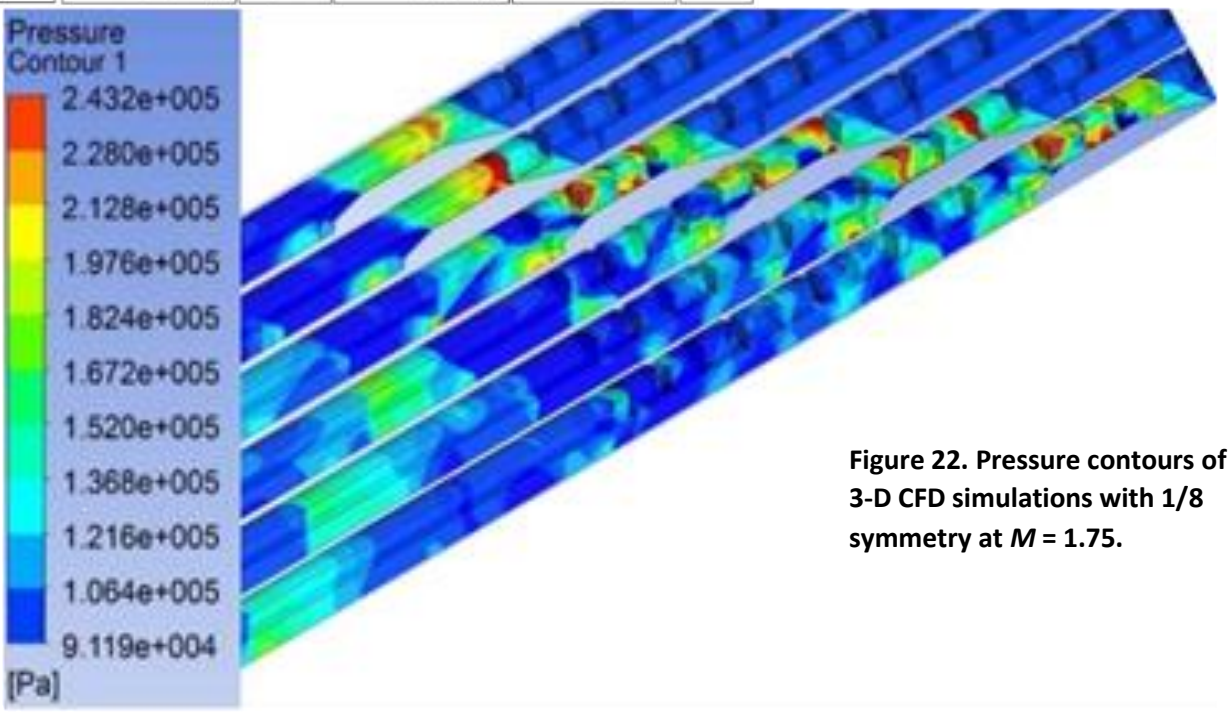

Figure 22. Pressure contours of 3-D CFD simulations with 1/8 symmetry at *M* = 1.75.

4. A.1: Drag coefficient study

Transients in drag coefficient (C_d) of the short-tailed projectile, referenced to its maximum area, were determined for several BTRA configurations at in-tube Mach numbers in the range of $1.75 \leq M \leq 4.37$. The instantaneous C_d was calculated by integrating the surface pressure and shear forces acting on the projectile at multiple positions as it passed from one particular baffle to the next. The variations in C_d when the projectile moves through the chamber between the 10^{th} to 11^{th} baffle in the BTRA configuration of Case 1 are shown in Fig. 23. The beginning and end points of these C_d plots indicate that the maximum drag coefficient values occur as the projectile shoulder just enters and leaves the baffle chamber. The highest C_d values were typically ~50% greater than those determined when the shoulder was in the middle of the chamber.

The impact of BTRA configuration on C_d was found to be significant, as evident by the C_d plots in Fig. 24 for the Case 8 configuration with same projectile in the Mach range of $1.75 \leq M \leq 3.49$. In this case, the baffle thickness was increased by a factor of 4 and the chamber width was reduced by 37%. With these much thicker baffles, the peak C_d values occurred after the shoulder cleared the baffle opening and had a maximum value approximately 4 times that of the relative minima at all Mach numbers. These results along with processed data from all other cases listed in Table 1 showed that the peak value of drag coefficient increased with increasing baffle thickness. Also, from numerical results not shown, it was found that for a given baffle thickness, the drag coefficient decreased as baffle spacing increased. Interestingly, maximum C_d did not monotonically increase with Mach number in either case shown here, this is attributed to the complexity of the wave interaction phenomena occurring in the chambers.

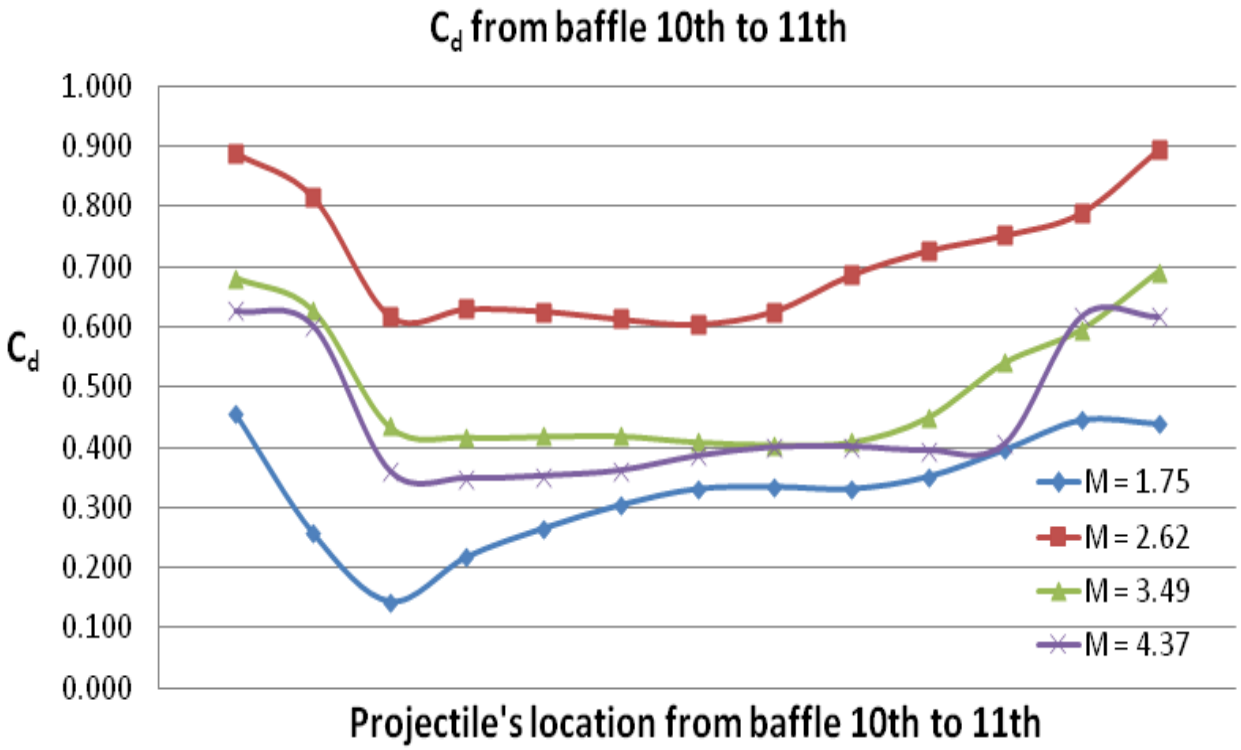

Figure 23. Variation of C_d during transit of Case 1 baffle chamber at different Mach numbers.

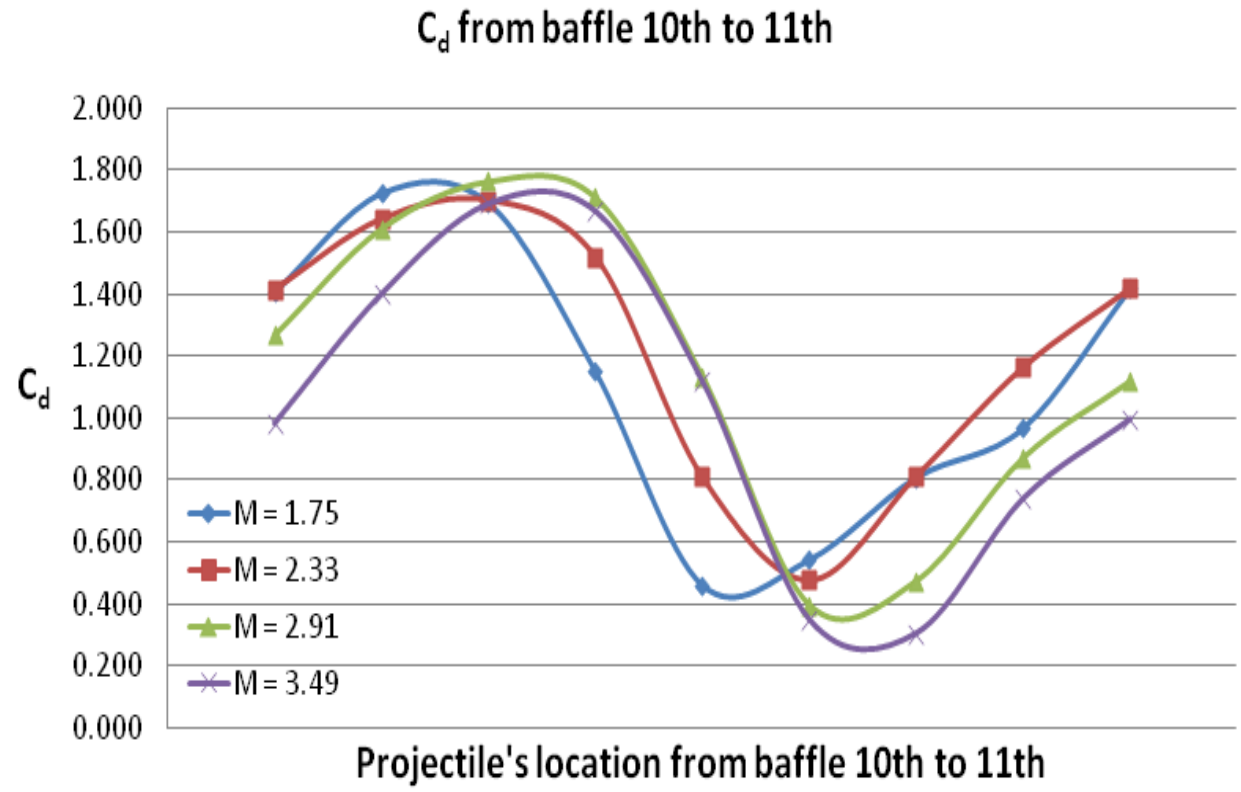

Figure 24. Variation of C_d during transit of Case 8 baffle chamber at different Mach numbers.

4. A.2: Chamber wall pressure study

Baffled tube chamber wall pressure distributions as the projectile passes through it were investigated to see how to correlate experimental tube wall pressure data as a function of transducer location. Computational pressure data for a short-tailed projectile were examined in detail at five equally spaced tube wall locations inside a single chamber, as shown in Fig. 25. The BTRA geometries of Cases 1 and 9 were analyzed in detail. In the representative cases presented here, tube-wall pressure histories were tracked inside the 11th chamber (between 11th and 12th baffle) from when the leading conical shockwave first enters the chamber until the bluff base of the projectile enters the chamber.

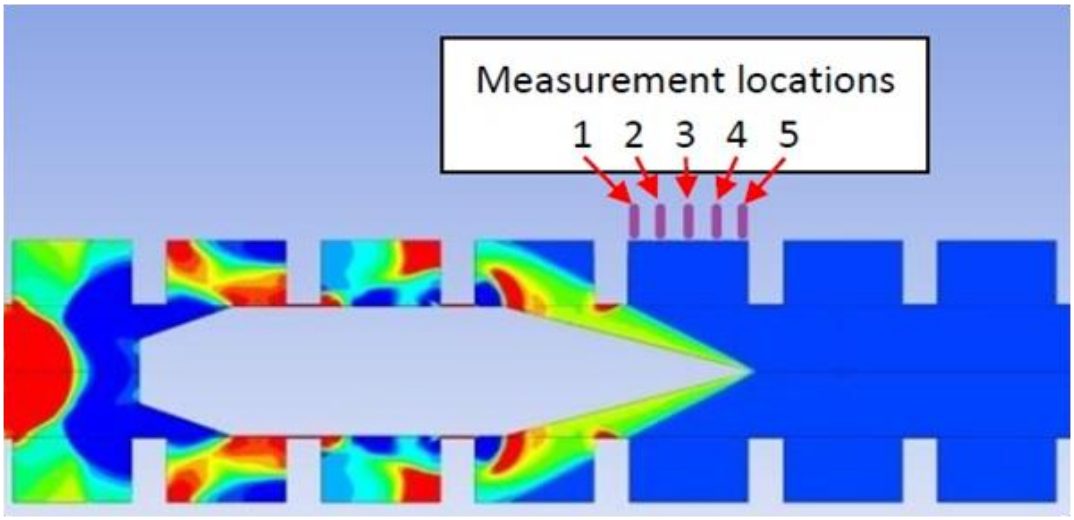

Figure 25. Tube wall locations for pressure-time data in baffle chamber.

The chamber pressure histories for a projectile moving at $M = 2.62$ (900 m/s) through the baffled tubed with $t_b = 3.81$ mm and $w_c = 30.6$ mm (Case 1 BTRA parameters) are shown in Fig. 26a and for a thicker baffle (9.40 mm) with same chamber width in Fig. 26b. These CFD results indicate that interpreting tube wall pressure data and tracking shockwave speeds via piezoelectric pressure transducers is complicated when the instrument ports at various stations

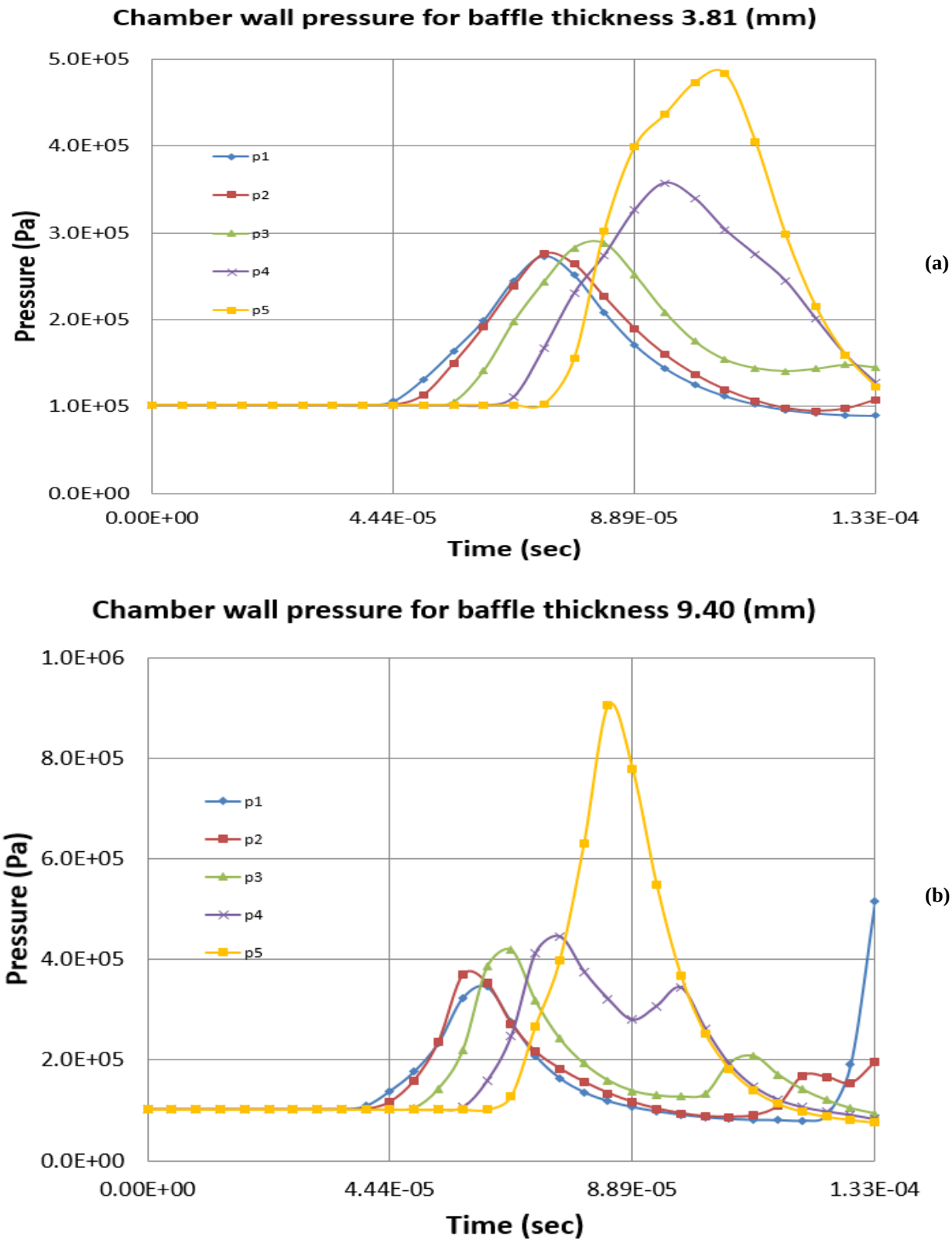

Figure 26. Tube wall pressure history at M = 2.62 from five equally spaced locations in baffle chamber of width w_c = 30.6 mm with baffle thicknesses of (a) t_b = 3.81 mm and (b) t_b = 9.40 mm.

along the BTRA are not exactly located at the same point in the chamber. Furthermore, the pressure on the forward face of the baffle is much higher than that elsewhere in the chamber, indicating that aftward-slanted baffles may reduce structural loads and drag forces acting on the projectile. These results led to an investigation of slanted baffles which is presented in the following section. Note, aftward (toward breech) and forward (toward muzzle) slants are from perspective of the baffle.

4. B: Reactive Flow Analysis

Thrust characteristics of the BTRA with various baffle designs and reactive propellants were investigated. As mentioned in Chapter 3, a smooth-bore domain was used prior to the baffled section to enable the combustion process to be initiated in a repeatable manner so that the influence of baffle geometry variations on net thrust generation could be distinguished from ignition transients. The baffled-tube section of the domain was made long enough (i.e., ~23 baffles) for a periodic flow field solution to be determined. After the transient behavior upon entrance to the baffled section had diminished, the pressure and shear forces on the projectile were integrated to determine the instantaneous thrust generated by the BTRA. With this procedure, the influences of baffle geometry, projectile shape, and projectile Mach number were examined for methane-oxygen propellants.

A hybrid finite rate/eddy-dissipation turbulent chemistry interaction model was utilized in reactive flow analysis. The pre-exponential factor in Arrhenius rate (finite rate model) is related to gas kinetic collision frequency and the higher its value, the higher its potential for starting the ignition process at a given temperature. Also, lower activation energy values in the Arrhenius rate promote the starting of the ignition process as well. A preliminary series of CFD calculations for a BTRA having $d_c/d_p = 2$ and $2CH_4+2O_2$ propellant with trace amounts of CO, CO_2, H_2O (less

than 1%) were carried out with a single step reaction mechanism chemistry in which the pre-exponential factor and activation energy values in Arrhenius rate were changed at various points in the simulation before the projectile enters the baffled-tube section while keeping the mixing rate of eddy-dissipation model the same. It was observed that the higher pre-exponential factor indeed promoted faster ignition; whereas changing activation energy caused some instability and led to divergence in the solutions. The impact of varying these Arrhenius rate parameters in the smooth bore section to promote propellant ignition and then reverting their values back to default in the BTRA section was found to be insignificant on the resulting BTRA thrust characteristics ultimately determined. Although ANSYS Fluent allows multi-step chemical reactions with finite rate/eddy-dissipation model, using more than 2-step mechanism is not recommended. Because, multi-step chemical mechanisms are based on Arrhenius rate which differ for each reaction. While, eddy-dissipation model has the same turbulent mixing rate. Therefore, the model cannot predict kinetically controlled species such as radicals in intermediate step (reactant → intermediate → products) [30]. To incorporate a multi-step chemical kinetic mechanisms in turbulent flow (more than 2-step chemical reactions), it is recommended to use eddy-dissipation model for large eddy simulation (LES). Carefully sized cell structures in the computational domains of LES regions are required, otherwise the computational time drastically increases. Also, it is important to note that, eddy-dissipation model requires product species to initiate the reactions and this is the reason that trace amounts of CO, CO_2 and H_2O were introduced during solver initialization [30].

The 2-step chemical reactions for $1CH_4+2O_2$ (stoichiometric) with finite-rate/eddy-dissipation turbulence-chemistry interaction model used in the rest of the reactive flow studies are shown below as Reactions (1) and (2). Also, inlets and outlets of the computational domains had the following mole fractions; 33% CH_4, 63% O_2, 1.34% CO, 1.33% CO_2 and 1.33% H_2O. The

Arrhenius rate relation for this finite-rate chemistry model is shown in Eq.22 with the coefficients for each reaction listed in Table 2. The eddy-dissipation rate model [34, 35] parameters for each reaction are shown in Eqs. 23-25 and their coefficients (C_{ED} and D_{ED}) are also listed in Table 2 (see Glossary section for complete description of variables used in Eqs. 22-25).

$$1CH_4 + \frac{3}{2}O_2 \rightarrow 1CO + 2H_2O \qquad Reaction(1)$$

$$1CO + \frac{1}{2}O_2 \rightarrow 1CO_2 \qquad Reaction(2)$$

$$\sigma_{Arrhenius} = A_{Arrhenius} T^{\beta} e^{-\frac{E_a}{\Re T}} [CH_4]^a [O_2]^b [CO]^c [CO_2]^d [H_2O]^e \qquad (Eq.22)$$

$$R_{1i,r} = \nu'_{i,r} M_{w,i} C_{ED} \rho \frac{\varepsilon}{\kappa} min_{\xi} \left(\frac{Y_{\xi}}{\nu'_{\xi,r} M_{w,\xi}} \right) \qquad (Eq.23)$$

$$R_{2i,r} = \nu'_{i,r} M_{w,i} C_{ED} D_{ED} \rho \frac{\varepsilon}{\kappa} \left(\frac{\sum_p Y_p}{\sum_j^n \nu''_{j,r} M_{w,j}} \right) \qquad (Eq.24)$$

$$\sigma_{Eddy-Dissipation} = min \left(R_{1i,r} , R_{2i,r} \right) \qquad (Eq.25)$$

Table 2. Finite-rate/eddy-dissipation turbulence-chemistry interaction model inputs.

Reaction	$A_{Arrhenius}$	E_a	β	a	b	c	d	e	C_{ED}	D_{ED}
1	5.012e+11	2e+8	0	-0.3	1.3	1	0	1	4	0.5
2	2.239e+12	1.7e+8	0	0	0.25	1	1	0	4	0.5

Table 3. Baffle and projectile geometry study.

Case	Baffle Geometry	Projectile Geometry
1	45° forward slanted	Short tail
2	45° aftward slanted	Short tail
3	Normal to wall	Short tail
4	23° aftward slanted	Short tail
5	23° aftward slanted	Long tail

The baffle and projectile geometry combinations listed in Table 3 were modeled with the reactive flow CFD to determine how they interact to affect thrust. In this part of the investigation, the projectile moved at $M = 2.86$ in a BTRA having $d_c/d_p = \sqrt{3}$ filled with stoichiometric methane-oxygen ($1CH_4+2O_2$) at 5 atm and 700 K. The static temperature contours of the flow field with the projectile at several different positions in the BTRA are shown in Fig. 27 for Cases 1-3.

Note forward-slanted baffles had a ramp on the downstream side of the baffle (Case 1) and aftward-slanted baffles had an inclined ramp on the upstream side (Case 2). The temperature contours within baffle chambers behind the projectile indicated that the propellant combustion was more complete in the Case 2 configuration (Fig. 27-middle), an observation which was backed up by the corresponding specie mass fraction contours (not shown). The thrust plots calculated at multiple points during the passage of the projectile through the BTRA are shown in Fig. 28 for each of the Cases 1-3 in Table 3.

Periodic solutions that occur in the latter half of the BTRA domain indicate the nominal operating conditions of the projectile for each particular case. The average thrust for Case 2 (aftward-slanted baffles) was found to be ~150% greater than that of Case 1 (forward-slanted

baffles). Case 3 (normal to sidewall baffles) thrust showed long transient behavior as thrust level was decreased while passing through to the BTRA and overall maintained lowest level of thrust in compare to Case 1 and Case 2. Because the average thrust was highest throughout most of the

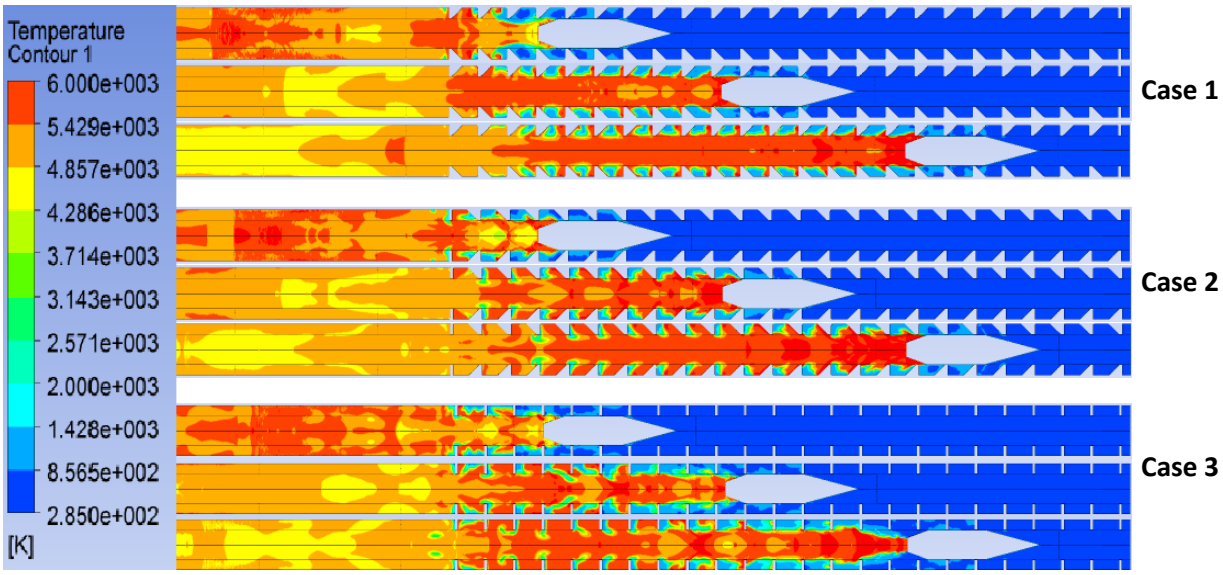

Figure 27. Static temperature contours at 3 projectile positions for Cases 1-3 at *M* = 2.86.

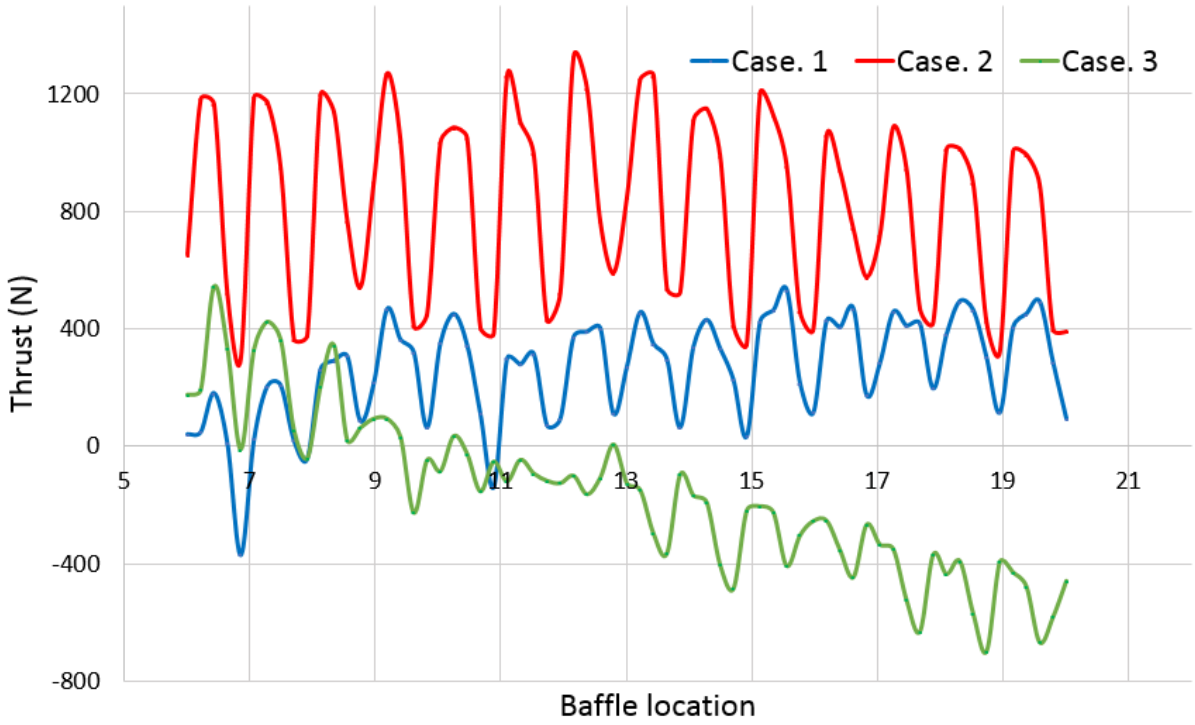

Figure 28. Thrust profiles of Cases 1-3 at *M* = 2.86 from baffles 6 to 20

BTRA in the Case 2 configuration, the aftward-slanted baffles were selected for more in depth investigation.

The static temperature contours of the flow field with the projectile at several different positions in the BTRA are shown in Fig. 29 for Cases 2, 4, and 5 in Table 3. Based on the

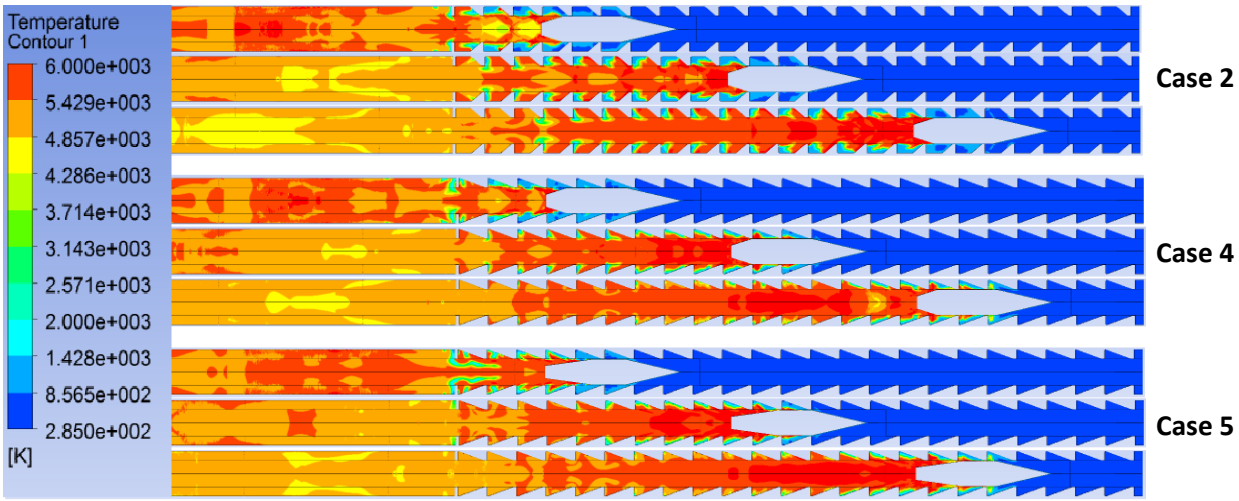

Figure 29. Static temperature contours at 3 projectile positions for Cases 2, 4, and 5 at *M* = 2.86.

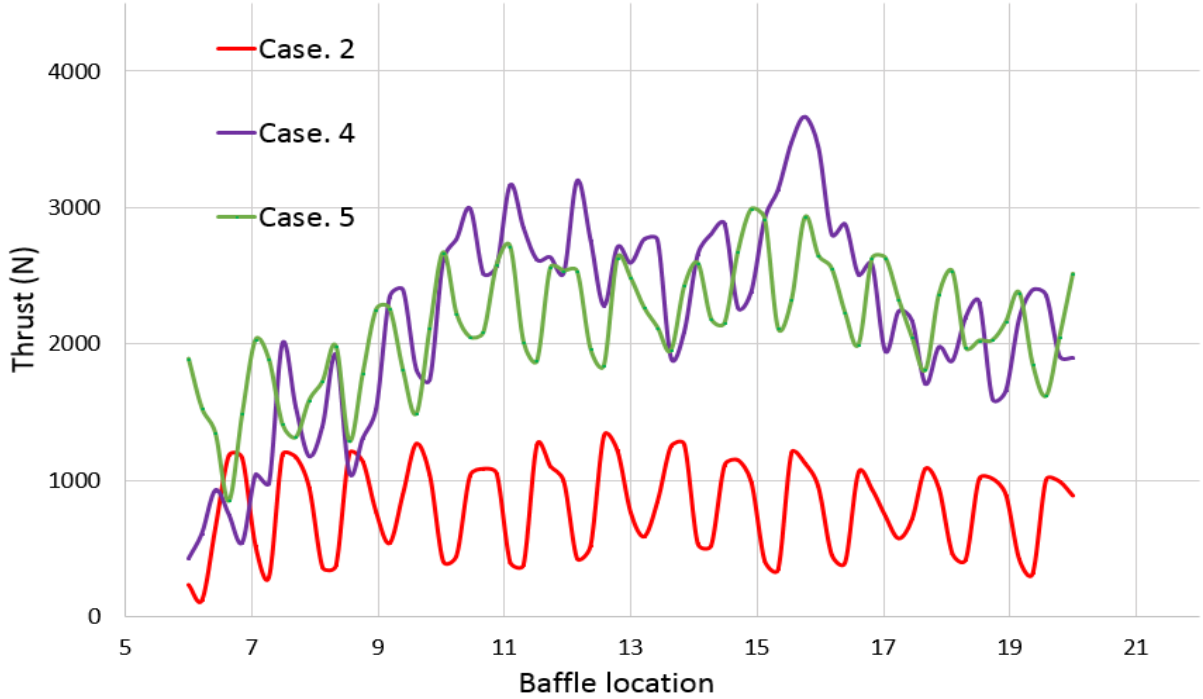

Figure 30. Thrust profiles of Cases 2, 4 and 5 at *M* = 2.86 from baffles 6 to 20.

indications that the combustion goes to completion in a shorter distance for the Case 2 configuration (Fig. 27), the ramp angle was decreased in Cases 4 and 5 from 45° to 23°. The impact of tail cone length and angle was investigated by using a short-tailed projectile (20° tail divergence angle) in Case 4 calculations and the long-tailed one (8.9° tail divergence angle) for Case 5. The temperature contours show that the more inclined baffles promote combustion completion in fewer baffles, and that the combustion moves farther up onto the projectile when the tail cone is lengthened for Case 5. The impact on thrust generation of these baffle and projectile variations is shown in Fig. 29. Both Cases 4 and 5 had average thrusts about 3 times greater than that of Case 2, although the difference in projectile geometry seemed to have little effect. A high transient thrust peak was observed for Case 4 around the 16^{th} baffle; however, this is likely a numerical artifact and needs to be further resolved. In any case, it is pretty conclusive that aftward-slanted projectiles improve BTRA thrust performance and shallower ramp angles are preferred. Optimization studies have not yet been attempted.

The influence of in-tube projectile Mach number was investigated using the Case 5 BTRA and projectile configurations in Table 3 in $1CH_4+2O_2$ propellant at 5 atm and 300 K. The temperature contours of projectiles traveling at constant Mach numbers of M = 2.91, 3.49 and 4.37 are shown in Fig. 31. These results indicate that the combustion requires more baffle chambers before it can go to completion as projectile Mach number increases. This is counter-intuitive considering that the total temperature of the flow increases with increasing Mach, as do the kinetic rates. Yet the time interval between projectile passage and any given baffle is smaller as the projectile Mach increases, thus the residence time of the propellant within the baffle chamber decreases proportionally. For example, the difference in baffle chamber residence time from M = 2.91 to 4.37 is ~33%, whereas the difference in total temperature is ~79%.

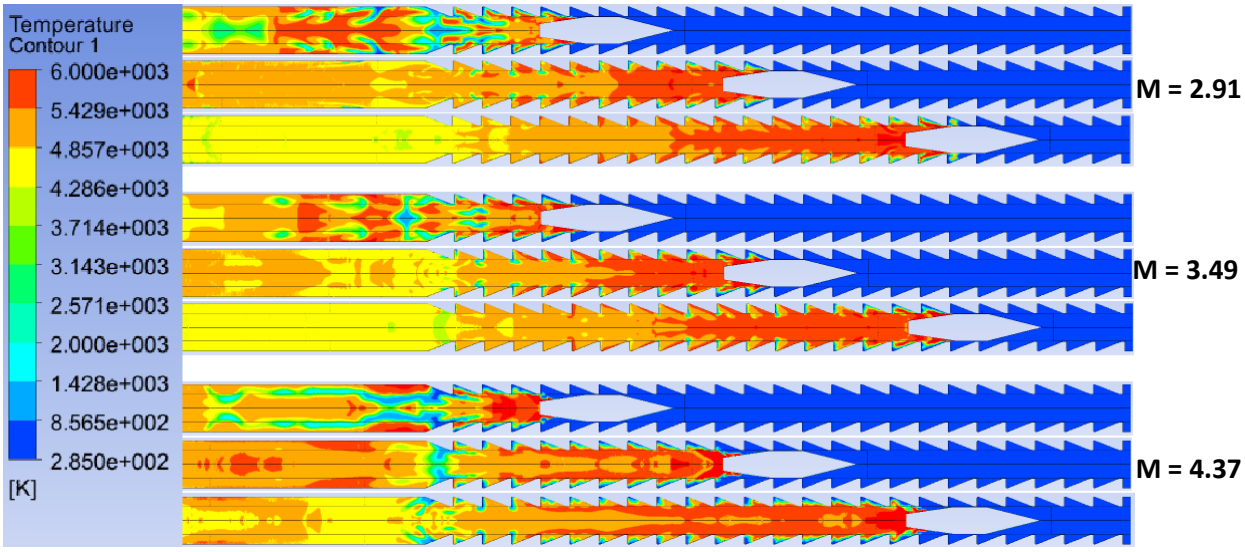

Figure 31. Temperature contours of Case 5 BTRA and projectile configuration at 3 Mach numbers.

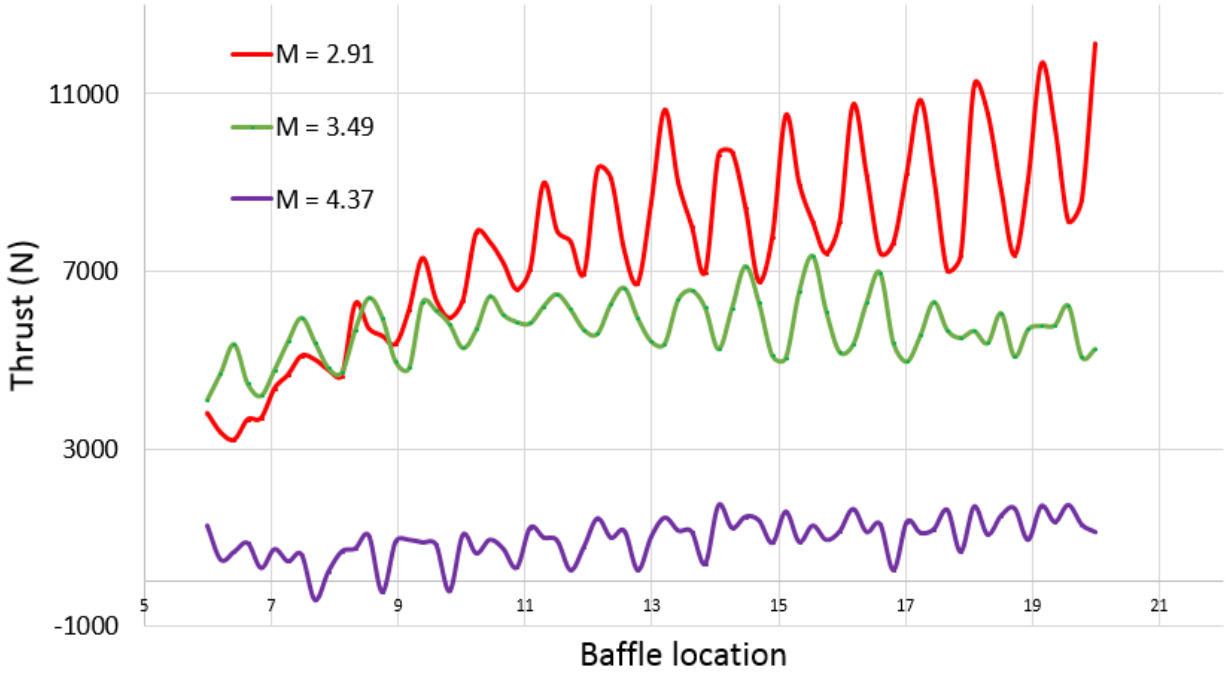

Figure 32. Thrust profile for Case 5 at *M* = 2.91, 3.49 and 4.37 from baffles 6 to 20.

Thus it appears that the decrease in combustion induction time due to the corresponding increase in propellant static temperature could compensate for the shortened residence time, however, turbulent mixing should also be taken into account. This is a topic currently under investigation.

The corresponding projectile thrust profiles for M = 2.91, 3.49 and 4.37 are plotted in Fig. 32. It is evident that the thrust decreases with increasing Mach number, which is consistent with predictions of general one-dimensional flow theory for the thermally choked ram accelerator propulsive mode [1, 4]. Deriving a thrust-Mach profile from this CFD method is possible and the detailed flow field calculations could provide insight into the influence of baffle drag on experimental BTRA thrust data [19].

As a result, a series of CFD models was generated to study projectile thrust profile behavior as Mach increased to determine the zero net thrust and its corresponding Mach on the long-tailed projectile (8.9° tail divergence angle) for both 23° and 45° aftward-slanted BTRA configurations in $1CH_4+2O_2$ propellant at 5 atm and 300 K. The baffle thickness, t_b, was 3.81 mm, the chamber width, w_c, was 30.6 mm and area contraction at 0.67 (or $d_c/d_p = \sqrt{3}$).

This study showed that in 23° BTRA configuration, the net thrust on the projectile decreased relatively linear and ultimately reached zero as Mach increased from 2.91 to 4.66. This behavior is consistent with the thrust-Mach behavior predicted using one-dimensional flow theory for thermally choked ram accelerator at subdetonative propulsive mode.

This study also found that in 45° BTRA configuration, the net thrust on the projectile decreased as Mach increased from 2.91 to 5.09. The numerical interpolation between data points indicates a nonlinear thrust reduction when Mach increased which could suggest a similar trend as in SBRA transitional behavior between thermally choked propulsive mode to transdetonative propulsive mode, which was experimentally observed when the ram accelerator operates at velocities greater than 85% of V_{CJ} [5, 12].

The cases listed in Table 4 were run at various Mach numbers with 2 different aftward slant angles for the baffles. Average net projectile thrust was obtained by integrating pressure and shear forces over its entire surface at every time step as it traversed the region from baffle 6th through baffle 20th.

Table 4. Long-tailed projectile study at various Mach numbers in BTRA configurations having aftward-slanted baffles.

Case	Baffle Inclination	In-Tube Mach	Average Thrust (N)
1	23°	2.91	8860
2	23°	3.49	5820
3	23°	4.37	1090
4	23°	4.66	-100
5	45°	2.91	4250
6	45°	3.49	1950
7	45°	4.37	1150
8	45°	4.66	890
9	45°	5.09	100

The projectile thrust profiles corresponding to Cases 1-4 listed in Table 4 are illustrated in Fig. 33. It shows that as Mach increases, the net thrust decreases. Data points of Cases 1-3 were extrapolated to determine that M = 4.66 was the gas dynamic limit in which there was zero net thrust on 23° BTRA configuration. The projectile thrust profiles corresponding to Cases 5-9 listed in Table 4 are illustrated in Fig. 34. In the 45° aftward slant configuration, unlike it did in with 23° slant, the net thrust did not go to zero at M = 4.66. It was found that in the 45° configuration, the net thrust decreases much more slowly than 1-D theory predicts as Mach increases from 3.49 to 4.66. Therefore, a new extrapolation of the computational results was required to estimate the Mach at which the projectile net thrust goes to zero. For the 45° BTRA configuration, it was found that at M = 5.09 the net thrust goes to zero after projectile passes the baffle 18th, as shown in Fig. 34.

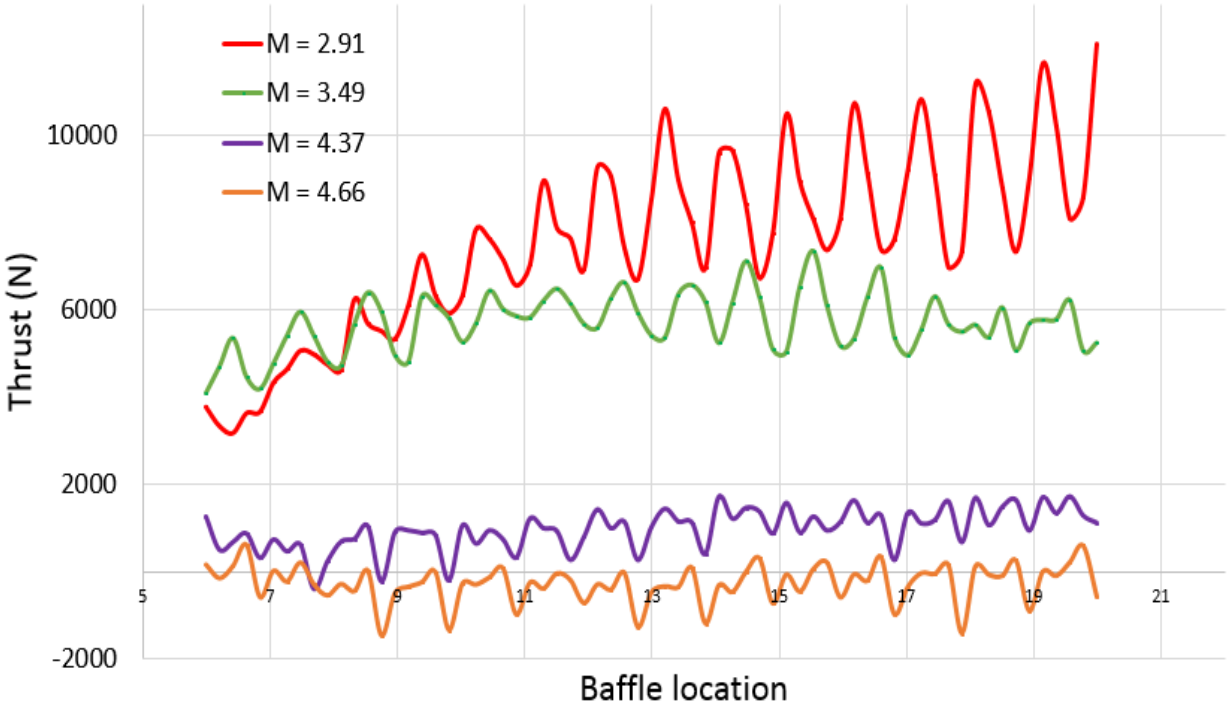

Figure 33. Thrust profile for long-tailed projectile in 23° aftward slanted configuration at *M* = 2.91, 3.49, 4.37 and 4.66 from baffles 6 to 20.

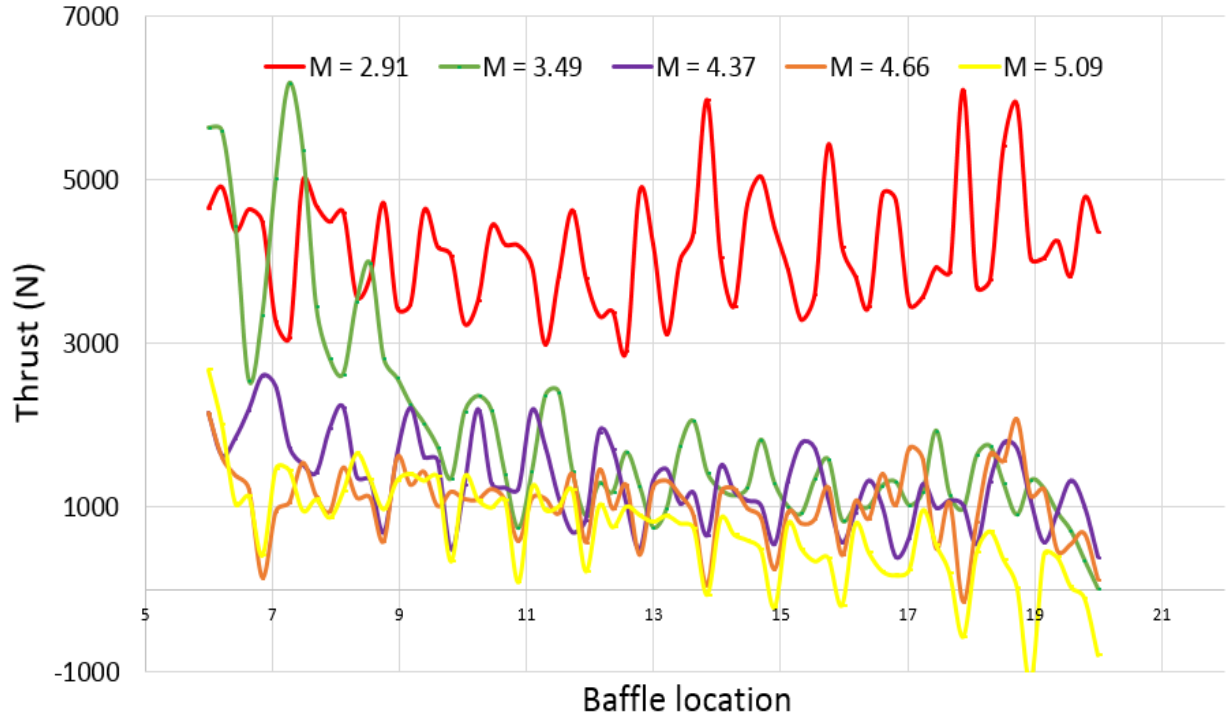

Figure 34. Thrust profile for long-tailed projectile in 45° aftward slanted configuration at *M* = 2.91, 3.49, 4.37, 4.66 and 5.09 from baffles 6 to 20.

The projectile thrust vs. Mach trends for Cases 1-9 (Table 4) are shown in Fig. 35. The dataset for 23° and 45° BTRA configurations are plotted with red-crosses and blue-dots, respectively. First order (red dash-line) and third order (blue dash-line) curves were fit to CFD thrust calculations for the 23° and 45° BTRA configurations, respectively. As discussed before, the thrust-Mach trend of the 45° BTRA configuration at higher Mach has a similar behavior to that experimentally observed in the transdetonative velocity regime by Hertzberg *et al.* [5] in SBRA. This implies that sufficient combustion may be occurring in the annular region between the

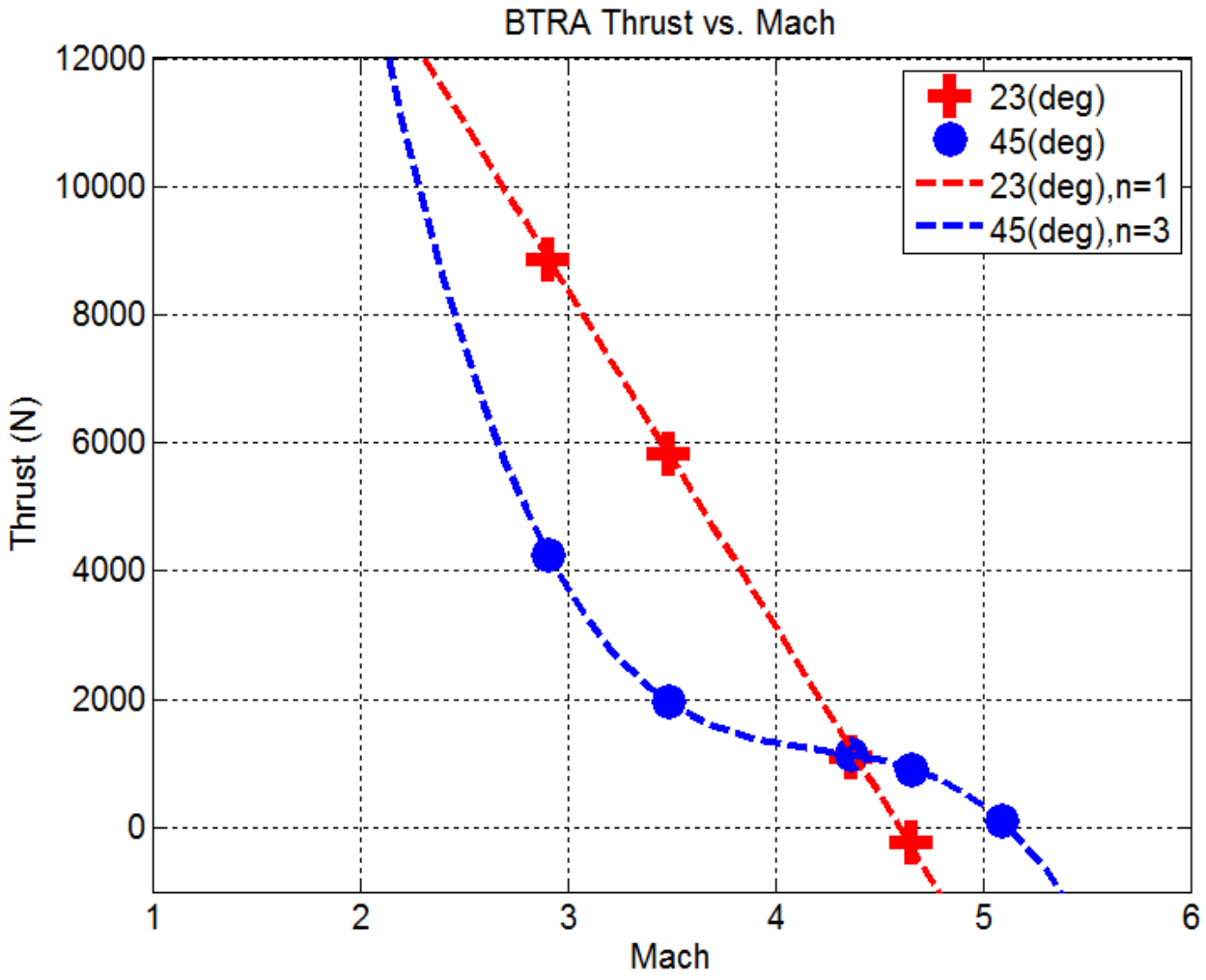

Figure 35. Thrust-Mach computations for a long-tailed projectile in BTRAs with 23° (red-crosses) and 45° (blue-dots) aftward-slanted baffles at *M* = 2.91, 3.49, 4.37, 4.66, 5.09 from baffles 6 to 20. First order (red dash-line) and third order (blue dash-line) curves were fit to CFD results for the 23° and 45° BTRA configurations, respectively.

projectile shoulder and chamber wall to generate extra thrust from combustion products being expanded by the tailcone nozzle.

4. B.1: Chamber wall pressure study

Wall pressure distributions from a baffle chamber of a BTRA configuration having normal baffles (i.e., with zero slant) as the projectile passes through it in reactive mixture was investigated to see how to correlate experimental chamber wall pressure data as a function of transducer location. In this particular case, computational pressure data for a short-tailed projectile were examined in detail in normal BTRA configurations at M = 2.86 at five equally spaced chamber wall locations inside a single chamber, as shown in Fig. 36 for Case 3 listed in Table 3.

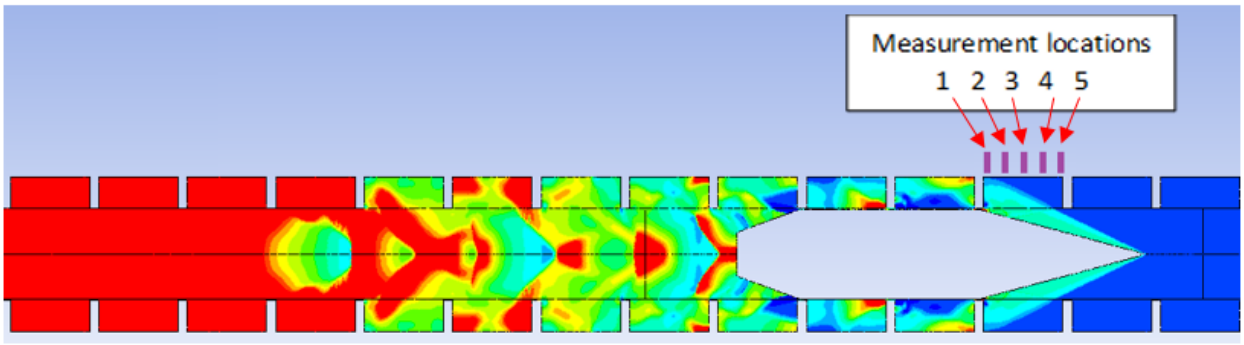

Figure 36. Wall chamber pressure data in normal BTRA configurations at M = 2.86.

In the representative case presented here, tube-wall pressure histories were tracked inside the 12th chamber (between 12th and 13th baffle) from when the leading conical shockwave first enters the chamber until the bluff base of the projectile leaves the 12th chamber. The chamber pressure histories for a projectile moving at M = 2.86 (1500 m/s) when fill temperature was 700K with t_b = 3.81 mm and w_c = 30.6 mm (Case 3 in Table 3) are shown in Fig. 37.

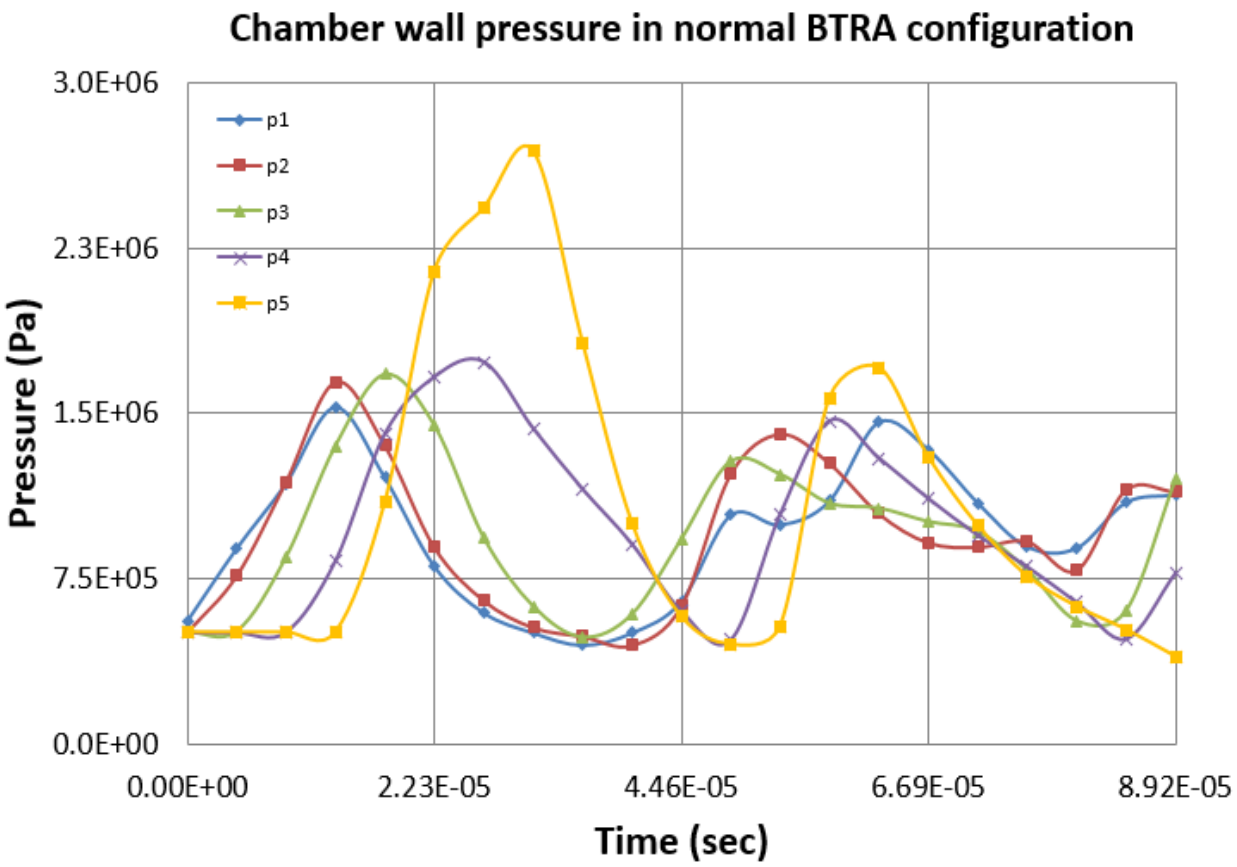

Figure 37. Chamber wall pressure history at M = 2.86 from five equally spaced locations in baffle chamber of width w_c = 30.6 mm and t_b = 3.81 mm in normal BTRA configurations

Similar to results from the chamber wall pressure study carried out in inert gas, the pressure peak on the forward face of the baffle (station 5) in reactive flow is much higher than anywhere else in the chamber in the normal to the wall BTRA configuration.

Chamber wall pressure distributions as the projectile passes through 23° and 45° BTRA configurations in reactive mixture were also investigated to see how to correlate experimental chamber wall pressure data (generated from experiments that are currently in progress) as a function of transducer location. Computational pressure data for a long-tailed projectile were examined in detail in 23° and 45° BTRA configurations at M = 3.49, Cases 2 and 6 (as listed in Table 4), at five equally spaced chamber wall locations inside a single chamber, as shown in Fig. 38a and 38b. In the cases presented here, tube-wall pressure histories were tracked inside the 12th chamber (between 12th and 13th baffle) from when the leading conical shockwave first enters the chamber until the bluff base of the projectile leaves the 12th chamber.

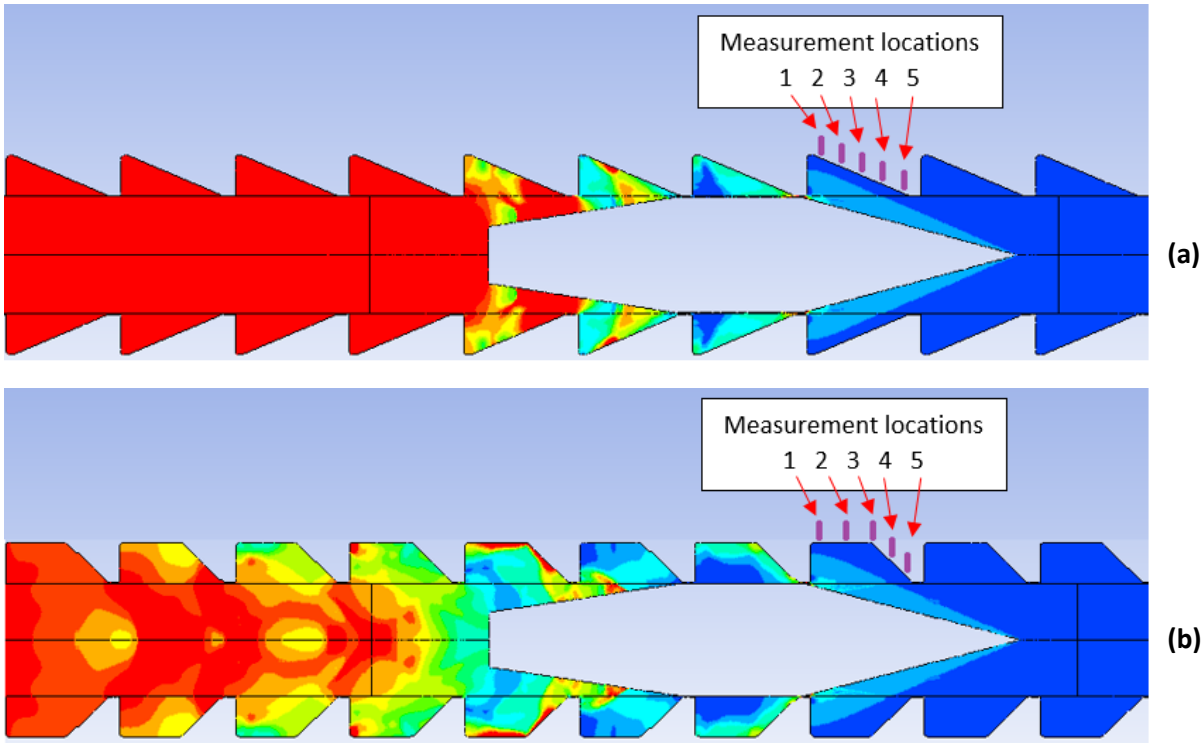

Figure 38. Wall chamber pressure data in (a) 23° and (b) 45° BTRA configurations at *M* = 3.49.

The chamber pressure histories for a projectile moving at M = 3.49 (1200 m/s) when fill temperature was 300 K through the 23° BTRA configuration with t_b = 3.81 mm and w_c = 30.6 mm (Case 2 in Table 4) are shown in Fig. 39a and for 45° BTRA configuration with the same baffle thickness and chamber width in Fig. 39b. The wall pressure histories as the projectile enters the baffle chambers of both BTRA configurations were similar; whereas the influence of the slant-angle of the baffles resulted in large differences in amplitude and character of the pressure data as the projectile base approached the exit of the chamber.

These CFD results indicate that interpreting chamber wall pressure data and tracking shockwave speeds via piezoelectric pressure transducers is complicated when the instrument ports at various stations along the BTRA are not exactly located at the same point in the chamber (similar to results from the chamber wall pressure study carried out in inert gas). Furthermore, the pressure peak on the leeward face of the baffle (station 1) is much higher than anywhere else in the chamber in the 23° BTRA configuration. It was also found that the 23° BTRA configuration experiences higher chamber wall pressure than 45° BTRA configuration when projectile moves at the same Mach number. Also in both BTRA configurations, the least chamber wall pressure fluctuation was measured at the 5th position in a given time range relative to other locations inside the chamber.

Although there is no direct comparison between the cases shown in Figs. 37 and 39 due to not having the same fill temperature and Mach, normal to the wall BTRA configuration does not experience high pressure loads in compare to aftward-slanted BTRA configurations. The lower pressure experienced in the normal to the wall BTRA configuration is consistent with low thrust production for this case.

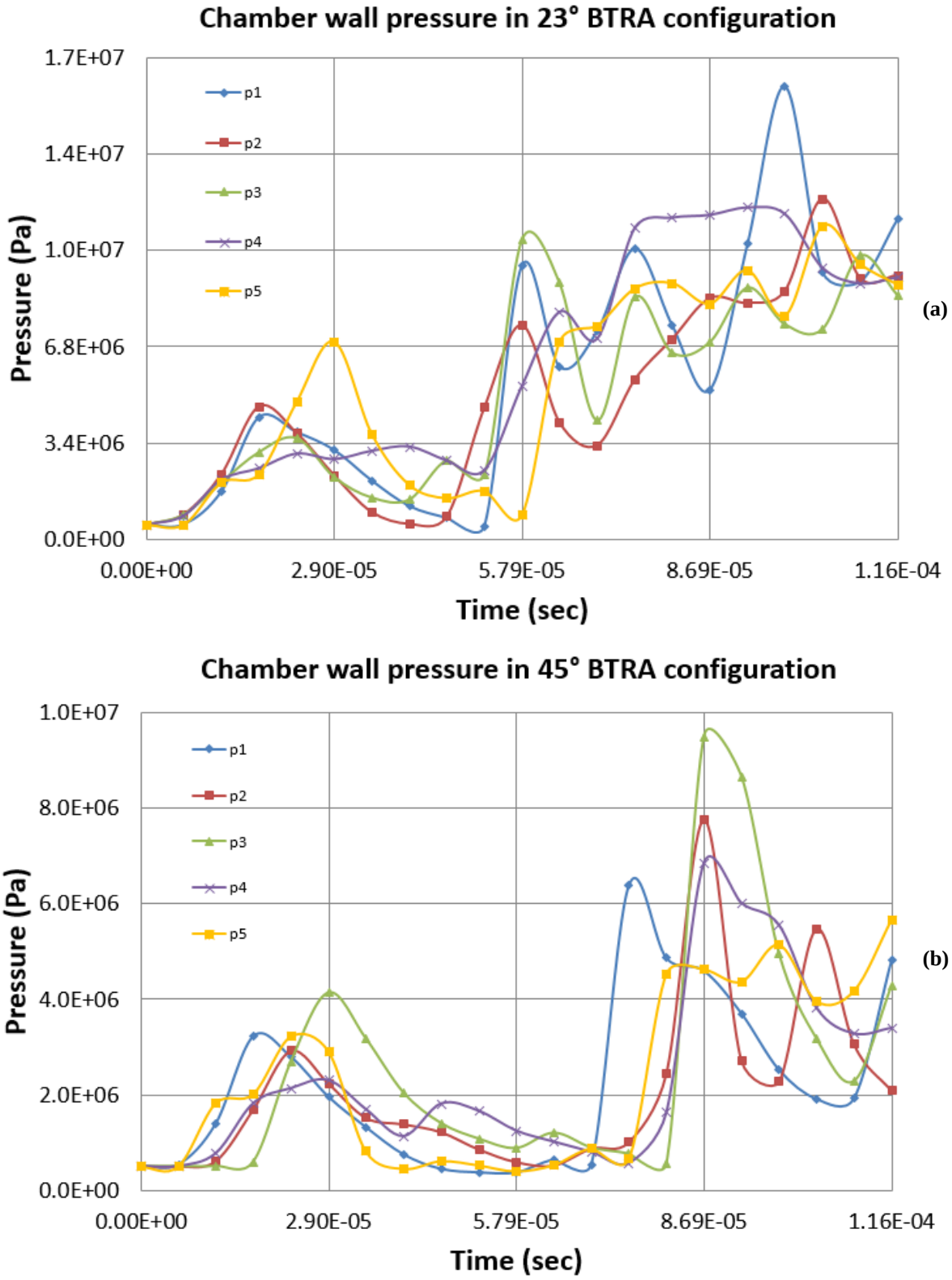

Figure 39. Chamber wall pressure history at M = 3.49 from five equally spaced locations in baffle chamber of width w_c = 30.6 mm and t_b = 3.81 mm in (a) 23° and (b) 45° BTRA configurations

4. B.2: Baffle-drag study

Baffle drag refers to the momentum loss of the combustion products as they move in the direction of the projectile's motion between a theoretical thermally choked plane, $M_2 = 1$, and aft-body of the projectile being accelerated in the BTRA. Transient baffle-drag of the long-tailed projectile was examined in detail in 23° and 45° BTRA configurations at in-tube $M = 3.49$, using results from Cases 2 and 6 listed in Table 4. Baffle-drag can be determined based on the time history of the pressure forces acting on the chamber walls and baffle surfaces. The moving flow behind the projectile exerted forces on the chamber walls as projectile passed through the baffled tube section. The force was calculated by integrating the surface pressure and shear forces on the chamber walls in the direction of projectile motion from the projectile's base as its shoulder just enters the baffle chamber from baffle 6^{th} to 20^{th}, as shown in Fig. 38.

A parameter called "n-chamber-offset drag variation" was defined which was the difference in calculated forces between any n-consecutive numbers of chamber behind the projectile's base (i.e., 8-chamber-offset drag variation was the difference in calculated forces when projectile's base was between baffle 17^{th} and 9^{th}, 16^{th} and 8^{th}, etc.). As a result, 1-chamber-offset drag variation and 9-chamber-offset drag variation produced 11 and 3 data-points respectively. The transients behavior of n-chamber-offset drag variation in 23° and 45° BTRA configurations at in-tube $M = 3.49$ using 7^{th} and 6^{th} order polynomial curve fits are shown in Figs. 40 and 41 respectively. The results showed that 45° BTRA configuration experienced larger chamber-offset drag variations than 23° BTRA configuration. Using data-points shown in Figs. 40 and 41, one can find an averaged chamber-offset drag for each of these curves between their relative maximum and minimum values respectively. The limits and averaged drag vs. numbers of chamber offset

from the base of the projectile using 7th and 6th order polynomial curve fits are shown in Figs. 42 and 43 for 23° and 45° BTRA configurations respectively.

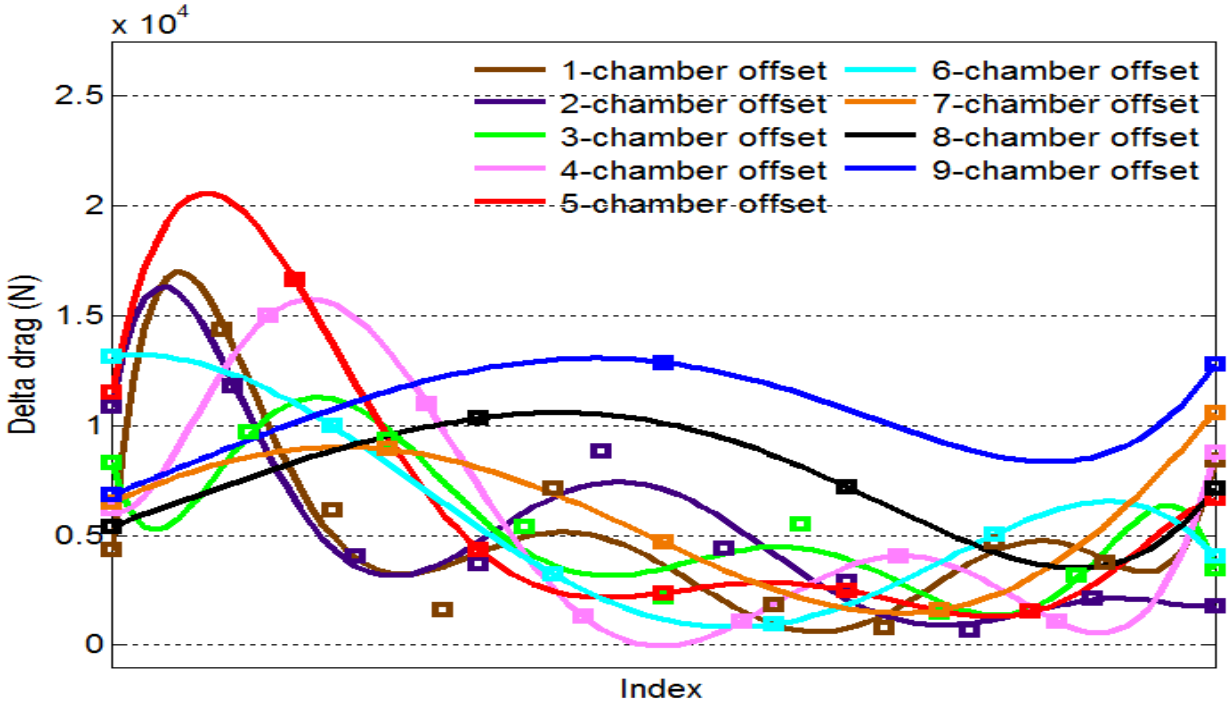

Figure 40. Chamber-offset drag variations in 23° BTRA configuration using 7th order polynomial curve fit as the projectile moved from baffle 6 to baffle 20.

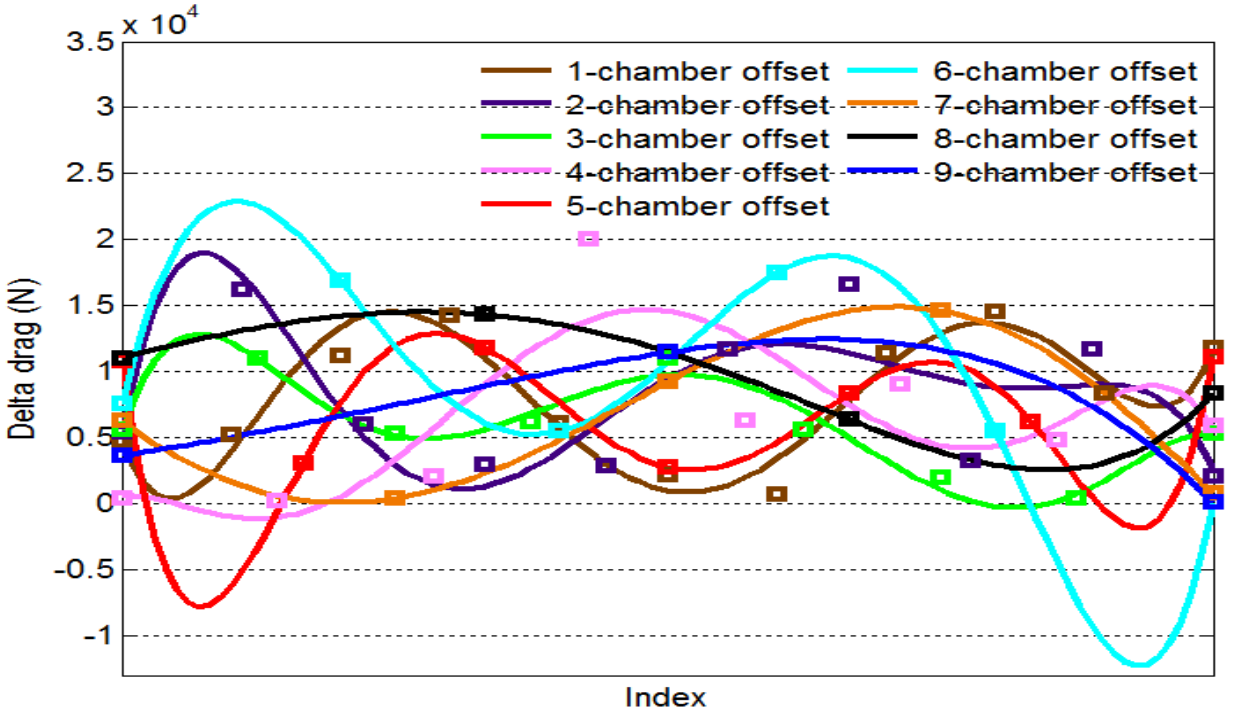

Figure 41. Chamber-offset drag variations in 45° BTRA configuration using 6th order polynomial curve fit as the projectile moved from baffle 6 to baffle 20.

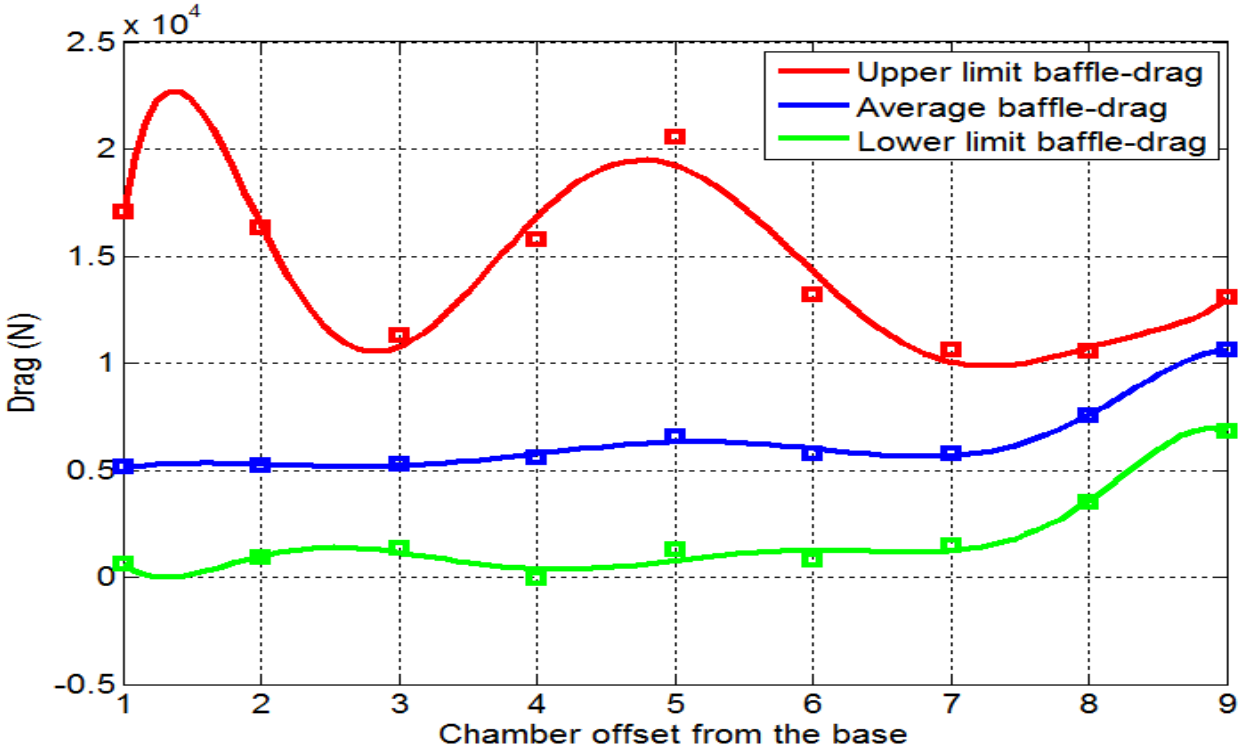

Figure 42. Upper, lower and averaged drag vs. number of chamber offset from the base of the projectile in 23° BTRA configuration using 7th order polynomial curve fit from baffle 6 to baffle 20.

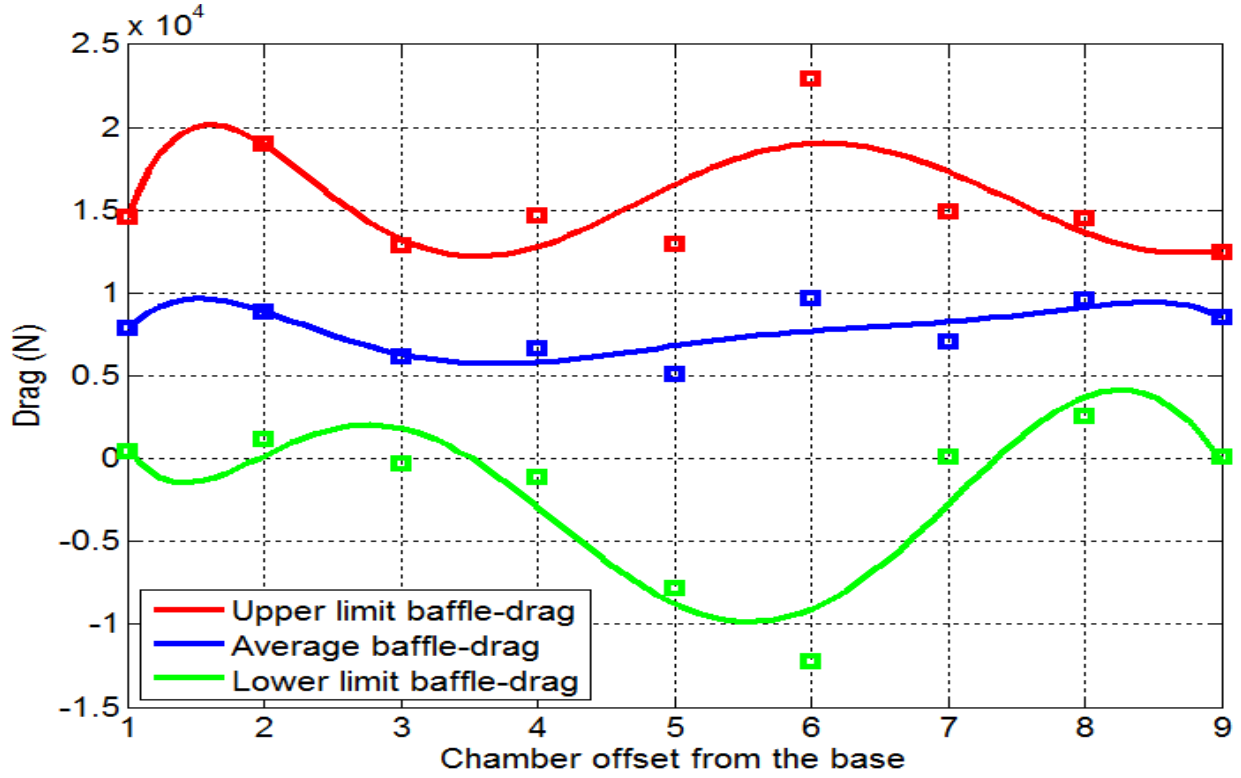

Figure 43. Upper, lower and averaged drag vs. number of chamber offset from the base of the projectile in 45° BTRA configuration using 6th order polynomial curve fit from baffle 6 to baffle 20.

The results shown in Figs. 42 and 43 indicate an oscillatory behavior on baffle-drag as a function of numbers of chamber behind the projectile's base. Interestingly, both 23° and 45° BTRA configurations had the least baffle-drag variation at about 8 chambers behind the projectile's base.

This observation suggests that the drag exerted on chamber walls from the moving flow behind the projectile showed the least variation in its magnitude around 8 chambers behind the projectile's base in baffled tube section. This observation led to further investigation to determine the local flow Mach behavior relative to the projectile in both BTRA configurations at around 8 chambers behind the projectile's base and whether the flow was thermally choked.

Similar to SBRA flow field shown in Chapter 2 (Fig. 7), one could draw the control volume around the projectile and baffled tube section to examine the flow field from upstream of the nosecone to a few chambers downstream of the projectile base. In Fig. 44, the control volume entrance (1) and exit (2) planes are identified for a 23° BTRA configuration.

The static pressure contours in Fig. 44a range from 1-110 atm for the BTRA operating conditions of Case 2 (Table 4). The pressure on tail section of the projectile is much higher than fill pressure, whereas the region of highest pressure is several chambers behind the projectile base. The local speed of sound contours in Fig. 44b range from 347-1500 m/s, which also closely correspond to temperature conours. The high sound speed (1500 m/s) throughout the center core of the BTRA control volume indicates that combustion has likely gone to completion within several chambers of the projectile base. The axial velocity component contours in Fig. 44c range from 0-1200 m/s. Flow on the tail section and in its wake for several chambers downstream is moving at near the projectile velocity (1200 m/s) and slows down to near zero velocity by the time it exits the control volume.

Based on flow field details like those shown in Figs. 44b and 44c, spatially averaged local speeds of sound and axial flow velocites in projectile's direction of motion were calculated at Station (2). The location of this exit plane was varied from 6-12 chambers behind the projectile base in the 23° configuration and 5-11 chambers in the 45° configuration as the projectile moved through the 15^{th} to 20^{th} baffles in the computational domain. Then flow velocity was calculated relative to the projectile using Galilean frame of reference transformation and the average axial Mach number was obtained using Eq. 7 at Station (2).

The control volume exit (Station 2) Mach number estimates, M_2, relative to the projectile, as a function of the number of chambers considered behind the projectile base for 23° and 45° BTRA configurations, are shown in Figs. 45 and 46, respectively. It was found that the Mach at Station (2) in 23° BTRA configuration reaches its maximum value of $M_2 = 0.80$ on average at about 7-9 chambers behind projectile's base. Similarly, the Mach at Station (2) in 45° BTRA configuration reaches its maximum value of $M_2 = 0.75$ on average at about 8-9 chambers behind projectile's base. In both BTRA configurations, M_2 increased due to heat addition via combustion process behind the base and reached a maximum value at about 8 chambers behind the projectile's base and then its value steadily decreased.

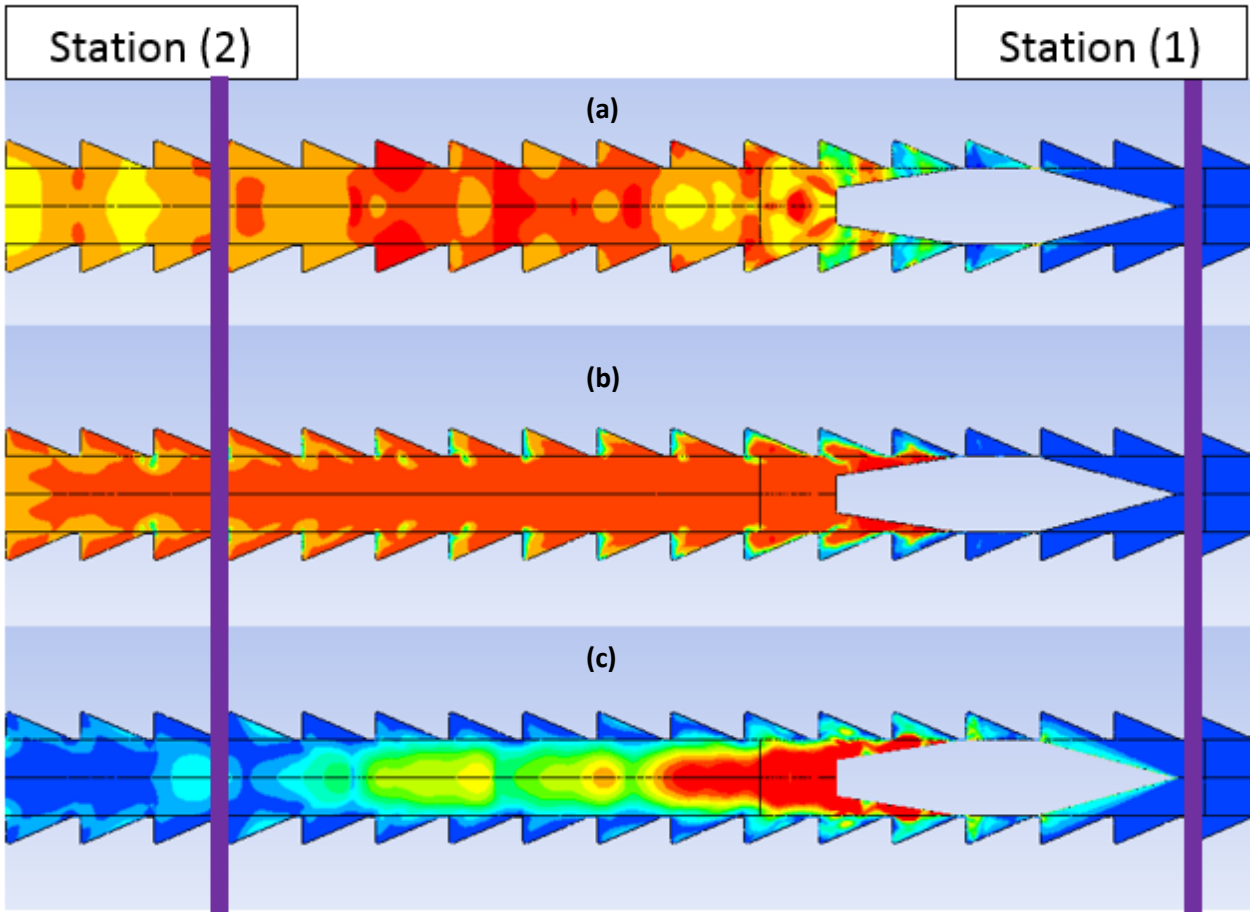

Figure 44. Control volume in 23° BTRA configuration at *M*=3.49 drawn on (a) static pressure contour in the range 1-110 atm, (b) local speed of sound in the range 347-1500 m/s and (c) velocity contour prior to Galilean frame of reference transformation in the projectile's direction of motion at laboratory frame of reference in the range 0-1200 m/s.

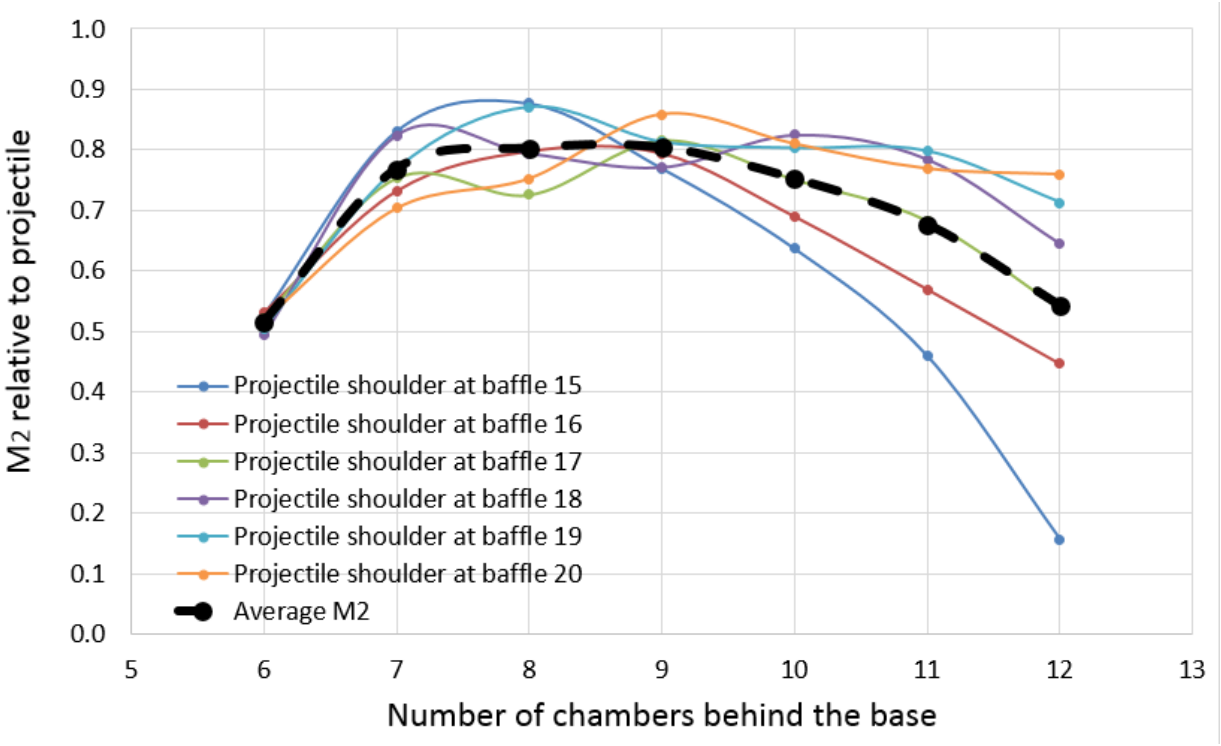

Figure 45. M_2 variations relative to the projectile as a function of numbers of chamber offset from the base of the projectile in 23° BTRA configuration from baffle 6 to baffle 20.

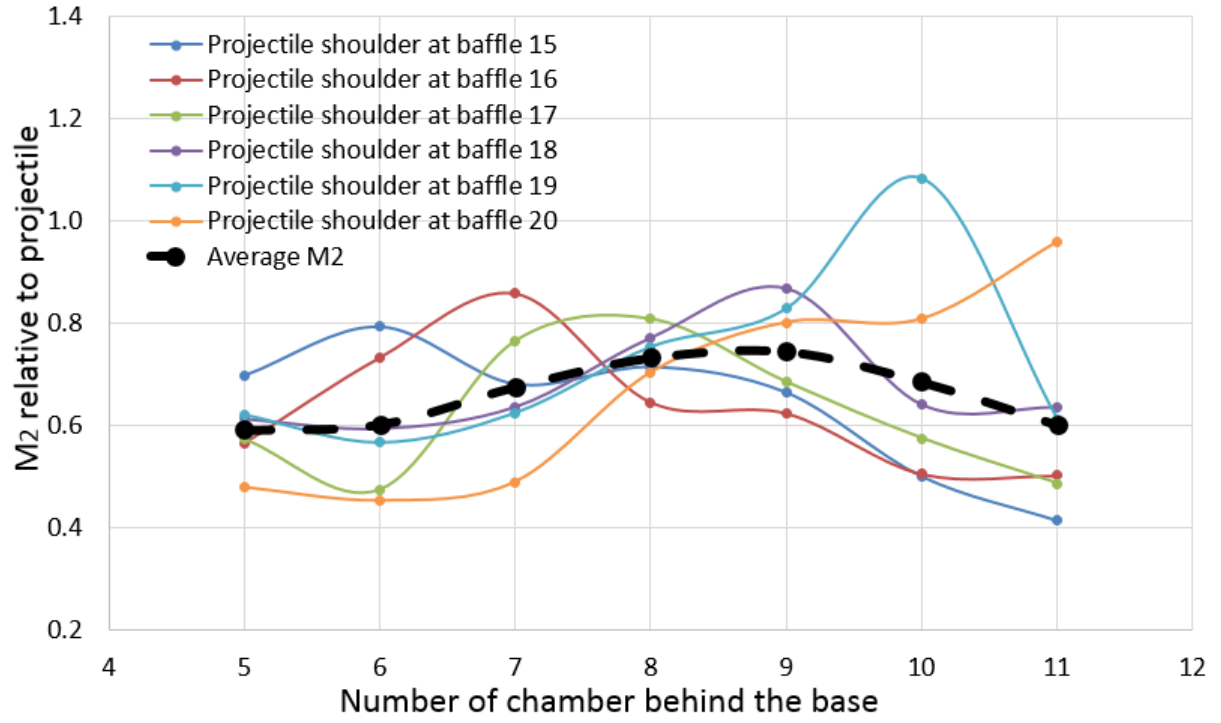

Figure 46. M_2 variations relative to the projectile as a function of numbers of chamber offset from the base of the projectile in 45° BTRA configuration from baffle 6 to baffle 20.

The numerical solutions did not show that flow reached the theoretical choked condition on average at Station (2), (i.e., $M_2 = 1$), as indicated by the average exit Mach curves (black-dash lines) in Figs. 45 and 46. It was found, however, that the least baffle-drag variation occurred where flow reached its maximum M_2 at about 8 chambers behind the projectile's base for both BTRA configurations at control volume entrance Mach of $M_1 = 3.49$.

If one could utilize both this observation and the average baffle-drag at about 8 chambers behind the projectile base, then thrust-to-baffle-drag ratio for 23° BTRA configuration was about 78% and about 20% for 45° BTRA configuration. Theoretical, computational and experimental baffle-drag analysis are subject of on-going investigations at University of Washington.

.

Chapter 5

Discussion

5. A: Inert gas results

The transient CFD modeling approach presented here generated inert gas solutions in about 8 hours per case on a AS-2022G-URF Supermicro workstation with 32 cores. The unstart process at the marginal entrance Mach number conditions was found to be quite gradual in that it required very long BTRA sections to attain either a periodic solution where the projectile nosecone remained supersonic or a solution with a normal shockwave being pushed ahead of the projectile. Since starting of the projectile was shown to be possible at an entrance Mach number 5% greater than the theoretical minimum for the reference BTRA geometry (Case 2, Table 1), efforts to further refine this result were not pursued. Instead, an investigation of the influences of baffle thickness and spacing on minimum starting Mach number was carried out. The results of this study led to the realization that baffles with greater thicknesses than initially anticipated could be used without a significant increase in minimum entrance Mach number. Thus, BTRAs designed with thicker baffles are feasible for higher fill pressures to achieve corresponding increases in potential thrust generation. The impact of rail thickness on minimum entrance Mach number is of interest, but has not yet been investigated.

The reflections of the shockwaves generated by the nosecone and projectile shoulder as it enters the baffle chamber result in a complex flow field that can be examined with transient CFD

methodology presented here. Although not shown in detail, it was found that wall pressure characteristics in the baffle chambers were strongly dependent on axial and azimuthal locations for 3-D BTRA geometries having rail supports in between the baffles. Thus, even in inert gas, interpretations of experimental tube-wall pressure have to consider the locations of the sensors (Fig. 26). The comparison of theoretical and experimental wall pressure measurements is part of this ongoing investigation.

The projectile drag in inert gas is periodically varying as it transits the baffle chambers; however, average drag coefficients can be determined as function of BTRA geometry, projectile Mach and projectile geometry. Variations in nosecone angle and rear cone geometry will change the projectile drag coefficient values, which are not that significant in themselves because the reactive flow thrust calculations inherently account for their influence. Nonetheless, the trend of increasing drag coefficient observed with thicker baffles and closer baffle spacing implies that optimized BTRA systems should not incorporate baffles with a thickness greater than that needed for the anticipated pressure peaks during operation and the spacing between baffles should be as large as allowable for the desired projectile shoulder lengths.

5. B: Reactive flow results

Reactive flow calculations using a 2-step chemistry model for CH_4-O_2 propellant in a computational domain having approximately $7.5x10^5$ cells were typically run for about $1.5x10^4$ time steps, each of which included about 30 sub-iterations before advancing (duration of time step varied from $7.5x10^{-8}$ to $4.3\ x10^{-8}$ second at various Mach). The resulting solutions took about 8-10 days to converge a solution on twin parallel computers having 4X20 E5-2698 v4 cores (overall 80 cores) connected via 56 Gbps InfiniBand cables. Others have shown that CFD modeling using a 5-step chemistry model for CH_4-O_2-N_2 propellant with axisymmetric projectiles can effectively and efficiently (i.e., 3-6 days per case with about five times the number of mesh elements and 100 times smaller mesh size) [21] determine the flow field properties in the combustion zone behind projectile over a relatively wide range of Mach number (e.g., $3.2 < M < 5$); however, these calculations were carried out in the projectile frame of reference with flow field initializations based on the solution from a different Mach number. Each solution of the transient modeling, using laboratory reference frame reported on here, required the calculations to start with the projectile impulsively moving at the Mach number of interest at the beginning of the computational domain, solutions from prior computations were not able to be used to speed up calculations.

Complete propellant combustion required 5-10 baffle chambers, depending on baffle geometry, and the number of required chambers tended to increase with increasing Mach number. Since the walls were adiabatic, heat losses, which may be significant in an actual BTRA, were not a factor. It is not yet clear if these numerical results are an artifact of the relatively simplistic 2-step chemistry model, finite-rate/eddy-dissipation turbulence-chemistry interactions, and/or computational mesh size scale (0.1 mm); or actually a good representation of the flow situation in a BTRA. Nonetheless, these results are consistent with recent experimental data showing thrust

deficits with respect to one-dimensional flow theory of 15%-50% in a BTRA having the baffle configuration of Case 1 in Table 1 [19]. More detailed experimental data from baffle chambers are needed to determine the accuracy of these calculations.

The preliminary baffle-drag study in reactive mixture indicates that the calculated baffle-drag is varying as it transits the baffle chambers; however, average baffle-drag can be determined as function of numbers of chamber behind the projectile base, projectile geometry, BTRA configuration and in-tube Mach. The current CFD results indicate that the baffle-drag increased as the baffle inclination angle increased for a given in-tube Mach.

As an engineering tool, these calculations were considered sufficiently accurate to guide the design of a more optimized BTRA configuration that incorporated ramped baffles. The current experimental efforts at University of Washington is focusing on validating the performance of aftward-slanted BTRA configuration. Fully accounting for baffle-drag in developing a quasi-one-dimensional model for the thrust-Mach performance characteristics of the BTRA is an ongoing theoretical and experimental effort [24].

Chapter 6

Conclusion and Future Plans

Transient CFD modeling with inert gas was used to examine the influence of various geometric parameters on the starting characteristics of the baffled-tube ram accelerator. The minimum starting Mach number for representative BTRA configurations was found to be only 5% greater than the ideal minimum, which implies that operation can be initiated at velocities less than 600 m/s in air-methane propellants. Excessive increases in baffle thickness while reducing the chamber width increased the minimum starting Mach number; however, it was found that very thick baffles could be used if their spacing was sufficiently large.

A method for analyzing reactive flow cases with transient CFD modeling was successfully developed. A smooth bore section was used to initiate and stabilize combustion prior to the projectile entering into the BTRA section. The transients of the entry process would die out after 10 baffles or so in the cases where periodic solutions were ultimately attained in the latter half of the computational domain. Aftward-slanting baffles with a shallow angle were identified as the most promising configuration for BTRA thrust generation. The thrust in the BTRA was found to decrease with increasing Mach number in the manner predicted by one-dimensional flow theory. Also the residence time of the propellant during combustion process in the vicinity of the projectile at any given baffle, influences the overall thrust production. As the projectile Mach increases, both the propellant residence time and overall thrust level decrease. The results of this investigation are

supporting the ongoing experimental and theoretical program to develop and optimize BTRA technology.

This study was a preliminary CFD modeling of BTRA and some of its characteristics was explored. The envelopes of operation in normal to the wall, aftward-slanted and forward-slanted BTRA configurations have yet to be explored in more details. Also, examining the combustion process properly requires to implement a multi-step rather than 2-step reaction mechanism chemistry. Baffle-drag analysis requires further scrutiny and detailed studies. Lastly, a systematic approach to optimize BTRA geometries could lead to a more profound understanding of BTRA configurations and their limits of operation.

Bibliography

[1]Hertzberg, A., Bruckner, A. P., and Bogdanoff, D. W., "Ram Accelerator: A New Chemical Method for Accelerating Projectiles to Ultrahigh Velocities," *AIAA Journal, Vol.* 26, 1988, pp. 195-203.

[2]Bruckner, A. P., Knowlen, C., Hertzberg, A., and Bogdanoff, D. W., "Operational Characteristics of the Thermally Choked Ram Accelerator," *J. of Propulsion & Power*, 7:828-36, 1991

[3]Knowlen, C., Bruckner, A. P., Bogdanoff, D. W., and Hertzberg, A., "Performance capabilities of the ram accelerator," *23rd Joint Propulsion Conference, Joint Propulsion Conferences*, AIAA paper, San Diego, CA, 1987-2152.

[4]Bruckner, A. P., Knowlen, C., Scott, K. A., and Hertzberg, A., "High-velocity modes of the thermally choked ram accelerator," 24th Joint Propulsion Conference, Boston, MA, AIAA 1988-2925.

[5]Hertzberg, A., Bruckner, A. P., and Knowlen, C., "Experimental investigation of ram accelerator propulsion modes," *Shock Waves*, Vol. 1, No. 1, 1991, pp 17-25.

[6]Hertzberg, A., Burnham, E. A., and Hinkey, J. B., *Recent advances in ram accelerator technology*, Combustion in High Speed Flows. Kluwer Academic Publishers, Dordrecht, 1994, Vol. 1, pp. 309-342.

[7]Kull, A. E., Burnham, E. A., Knowlen, C., Bruckner, A. P., and Hertzberg, A., "Experimental studies of superdetonative ram accelerator modes," *25th Joint Propulsion Conference*, AIAA paper, Monterey, CA, AIAA 1989-xxxx.

[8]Knowlen, C., "Theoretical and Experimental Investigation of the Thermodynamics of the Ram Accelerator in the Thermally Choked Mode," PhD thesis, Department of Aeronautics and Astronautics, University of Washington, Seattle, WA, 1991.

[9]Chew, G., Knowlen, C., Burnham, E. A., Hertzberg, A., and Bruckner, A. P., "Experiments on Hypersonic Ramjet Propulsion Cycles Using a Ram Accelerator," *27th Joint Propulsion Conference*, Sacramento, CA, AIAA 1991-xxxx.

[10]Brackett, D. C., and Bogdanoff, D. W., "Computational investigation of oblique detonation ramjet-in-tube concepts," *Journal of Propulsion and Power*, Vol. 5, No. 3. 1989, pp. 276-281.

[11]Bogdanoff, D. W., "Ram accelerator direct space launch system- New concepts," *Journal of Propulsion and Power*, Vol. 8, No. 2. 1992, pp. 481-490.

[12]Burnham, E. A., Kull, A. E., Knowlen, C., Bruckner, A. P., and Hertzberg, A., "Operation of the Ram Accelerator in the Transdetonative Velocity Regime," *26th Joint Propulsion Conference*, Orlando, FL, AIAA 1990-1985.

[13]Bruckner, A.P. and Knowlen, C., "The Ram Accelerator: Review of Experimental Research Activities in the U.S," *Experimental Methods of Shock Wave Research,* Vol. 9, Igra O. and Seiler, F. eds., Springer-Verlag, Berlin, 2014.

[14]Higgins, A. J., Knowlen, C., and Bruckner, A. P., "Ram Accelerator Operating Limits, Part 1: Identification of Limits" *Journal Propulsion and Power*, Vol. 14, No. 6, 1998, pp. 951-958.

[15]Seiler, F., Patz, G., Smeets, G., and Srulijes, J., "Presentation of the Rail Tube Version II of ISL's RAMAC 30" *Ram Accelerator* Takayama K, Sasoh A (ed.) Springer-Verlag, Heidelberg, 1998, pp. 79-87.

[16]Higgins, A. J., Knowlen, C., and Kiyanda, C. B., "Gasdynamic Operation of Baffled Tube Ram Accelerator in Highly Energetic Mixtures" *20th International Colloquium on the Dynamics of Explosions and Reactive Systems,* McGill University, Montreal, Canada, July 31 – August 5, 2005.

[17]Higgins, A. J., "Ram Accelerators: Outstanding Issues and New Directions," *Journal Propulsion and Power*, Vol. 22, No. 6, 2006, pp. 1170-1187.

[18]Bruckner. A. P., and Knowlen, C., "Ram Accelerator," *Encyclopedia of Aerospace Engineering*, R. Blockley and W. Shyy (eds), John Wiley & Sons, Ltd. 2010, Airbreathing Engines 590

[19]Knowlen, C., Glusman, J.F., Grist, R., Bruckner, A.P., and Higgins, A.J., "Experimental Investigation of a Baffled-Tube Ram Accelerator," AIAA-2016-4813.

[20]Knowlen, C., and Bruckner, A.P., "Direct Space Launch Using Ram Accelerator Technology," *Space Technology and Applications International Forum*, American Institute of Physics. 2001.

[21]Bengherbia, T., Yao, Y., Bauer, P., and Knowlen, C., "Numerical Study of Gaseous Reactive Flow Over a Ram Accelerator Projectile in Subdetonative Velocity Regime," *Eur. Phys. J. Appl. Phys.*, 55:11022, 2011.

[22]Bundy, C., Knowlen, C., and Bruckner, A.P., "Unsteady Effects on Ram Accelerator Operation at Elevated Pressures," *J of Propulsion & Power*, 20(5):801-810, 2004.

[23]Bengherbia, T., Contribution to Numerical Simulation Analysis of the Flow in the Ram Accelerator in the Subdetonative Propulsion Mode, *Ph.D. Dissertation,* École Nationale Supérieure de Mécanique et d'Aérotechnique, Aout, 2006.

[24]Glusman, J.F., "Theoretical Performance Model and Initial Experimentation of a Baffled-Tube Ram Accelerator," Masters Thesis, William E. Boeing Department of Aeronautics and Astronautics, University of Washington, Seattle, WA, 2016.

[25]Tanguay, V., and Higgins, A., On the Inclusion of Frictional Work in Non-Ideal Detonations, 20th International Colloquium on the Dynamics of Explosions and Reactive Systems. McGill University, Montreal, Canada, July 31August 5, 2005.

[26]ANSYS Fluent, Software Package, Ver. 14.0 & 15.0, ANSYS, Inc. Southpointe 2600 ANSYS Drive Canonsburg, PA.

[27]Schultz, E., Knowlen, C., and Bruckner, A.P., "Starting Envelope of the Subdetonative Ram Accelerator," *Journal of Propulsion & Power*, 16:1040-1052, 2000.

[28]ANSYS, Inc. “Ansys Fluent User’s Guide,” Boundary Conditions, 2013, pp. 327-423.

[29]ANSYS, Inc. “Ansys Fluent User’s Guide,” Dynamic Layering, 2013, pp. 592-595.

[30]ANSYS, Inc. “Ansys Fluent UDF Manual,” Dynamic Mesh DEFINE Macros, 2013, pp. 190-192.

[31]ANSYS, Inc. “Ansys Fluent Theory Guide,” 2013, Chapter 1, 3, 4, 20, 21.

[32]ANSYS, Inc. “Ansys Fluent Meshing’s User Guide,” 2013.

[33]Liepmann, H. W, and Roshko, A., *Elements of Gasdynamic*, New York: Wiley, 1957

[34]Magnussen, B.F and Hjertager, B.H. “On Mathematical Models of Turbulent Combustion with Special Emphasis on Soot Formation and Combustion,” 16th Symp. (Int’l.) on Combustion. The Combustion Institute, 1976.

[35]Spalding, D.B. “Mixing and Chemical Reaction in Steady Confined Turbulent Flames,” 13th Symp. (Int’l.) on Combustion. The Combustion Institute, 1970.

Appendix A

Fluent – Design Inputs

In this section, generating the computational domain for an axisymmetric BTRA using the ANSYS-Fluent-Design Modeler is briefly described in few general steps:

1. One needs to sketch various computational domains based on knowledge of realizing which regions in the domain are rigid or deforming.
2. Fully constraint sketches must be used to generate "surfaces from sketches". 1st surface is generated via "add material" option and the rest of surfaces are generated via "add frozen" option.
3. Additional sketches must be created to generate edges which are used to split the surfaces. Splitting a surface to sub-surfaces allows implementing various mesh cell sizes to a single surface and the connectivity between all sub-surfaces are preserved.
4. Use sketches to generate edges via "line from sketches" and then implement "projection" to utilize edges to split the surfaces of interest.

Fig. A shows the general interface of ANSYS-Fluent-Design Modeler and a typical axisymmetric 23° aftward-slanted BTRA configuration computational domain. On the left-hand side of the Fig. A, "surfaces from sketches", "line from sketches" and "projection" operations for various regions are illustrated. The next figure, Fig. B, illustrates the virtual walls location behind the projectile and also four edges which were utilized to split the rigid domain around the projectile

for optimal mesh generation. The edges were used to split the baffled tube region at minimum gap between shoulder of the projectile and baffle wall for optimal mesh sizing are shown in Fig. C.

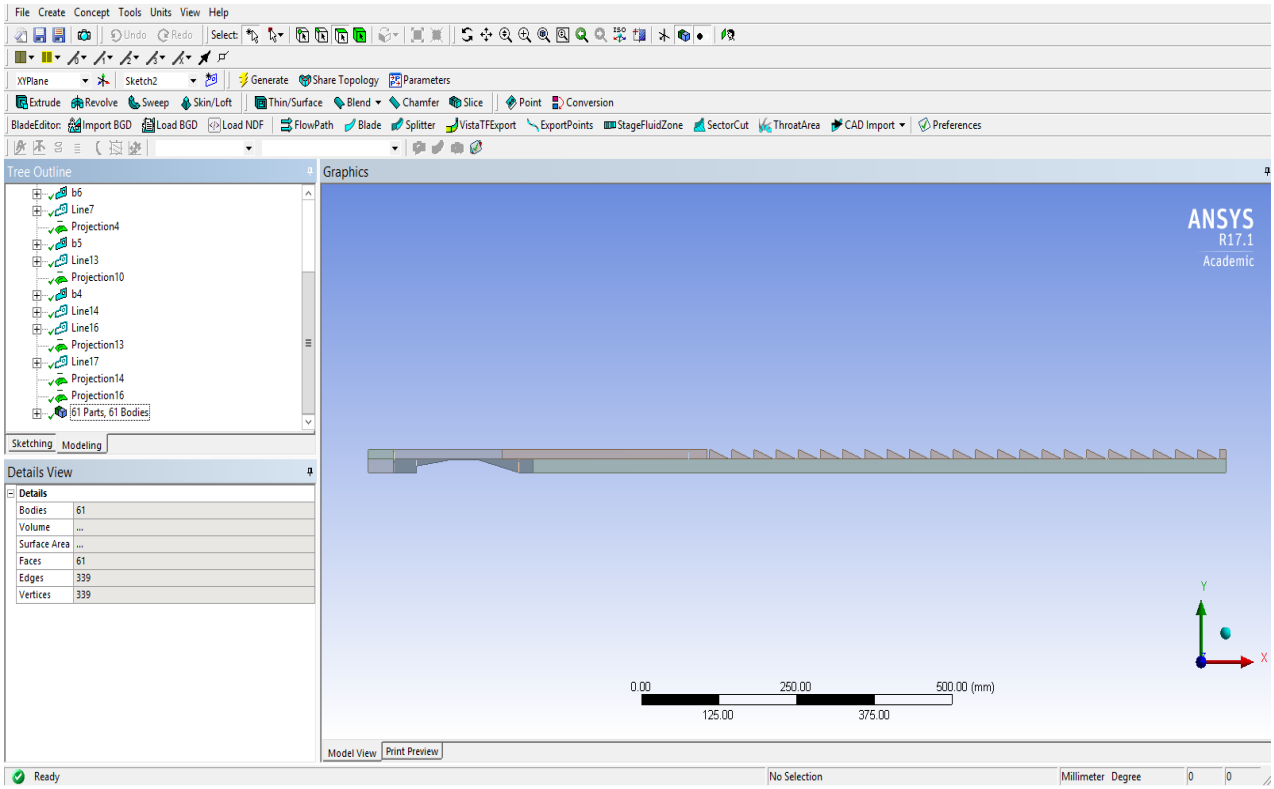

Figure A. ANSYS-Fluent-DesignModeler interface with toolbar at the top. Surfaces, edges and projections are generated under tree outline shown on left. Generic axisymmetric 23° aftward-slanted BTRA configuration computational domains shown on the right.

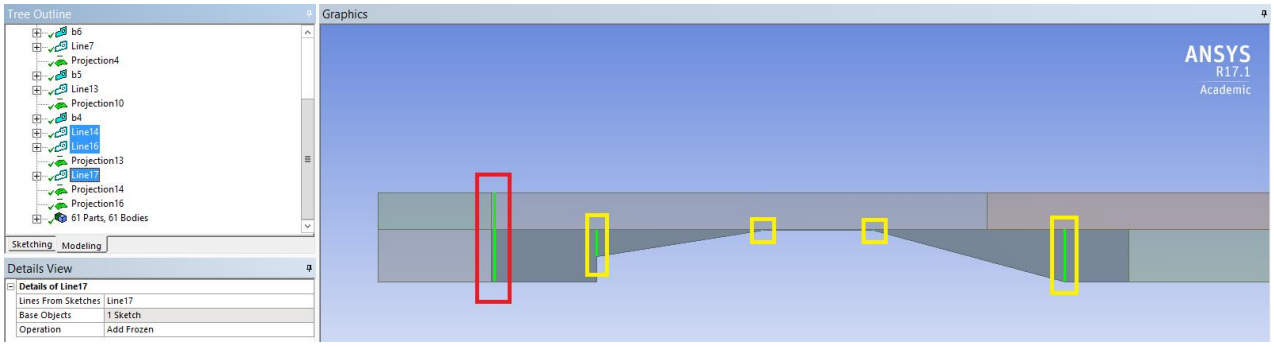

Figure B. Virtual wall location located behind the projectile (shown in red box). Four edges were used to split the rigid domain around the projectile for optimal mesh sizing (shown in yellow

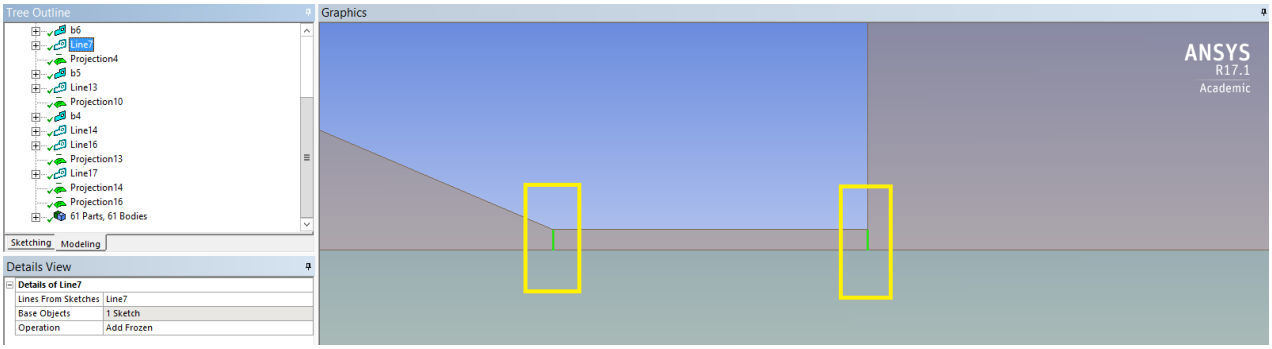

Figure C. Edges (shown in green) were used to split the baffled tube region at minimum gap between shoulder of the projectile and baffle wall.

It is important to note that an elegant design of the computational domain not only ease the meshing efforts and facilitate setting up the solver, but also save time during post-processing and data analysis.

Appendix B

Fluent – Meshing Inputs

In this section, generating the mesh on an axisymmetric BTRA using the ANSYS-Fluent-Mesh is briefly described in few general steps:

1. One needs to assign name to all edges, interfaces and domains by selecting them and right-clicking and “create name selections” prior to executing any meshing operations.
2. Inlet, outlet, axis and wall are the generic names that Fluent solver recognizes. Various edges can be grouped as one entity if needed and assigned a specific name.
3. It is highly recommended to break baffled tube wall section into individual walls and distinguish each of them with a distinct number; i.e., wall1, wall2, etc. A thoughtful name allocation to various edges, interfaces and domains eases the post-processing and data analysis.
4. Contact between various domains are generated under “connection” using the names that were assigned to all edges and interfaces. This operation guarantee the connectivity between different interfaces and domains.
5. Setup a default “sizing”, “inflation” and “assembly meshing” cell dimensions based on relatively well-understood physics of the BTRA prior using meshing tools such as “sizing”, “contact sizing”, and “refinement” on various regions.
6. Run diagnostic after each meshing attempt. Utilizing “statistics” mesh metric such as “skewness”, “element quality” and “orthogonal quality” are highly recommended.

7. Knowing the computational limits and their expenses, carefully adjust numbers of the cells and/or their sizes if necessary without compromising the solution quality and its accuracy. Multiple preliminary CFD runs are generally required to validate the accuracy of the results.

Fig. D shows the general interface of ANSYS-Fluent-Mesh and a typical axisymmetric 23° aftward-slanted BTRA configuration computational domains. On the left-hand side of the Fig. D, "connections", "mesh" and "name selections" for various regions are illustrated. Fig. E1-5 show the locations of all the edges and interfaces and where they have "connection" to other domains and interfaces. Fig. F shows a generic default setup for mesh sizing. Fig G1-4 show cell sizing for specific highlighted area shown in blue regions.

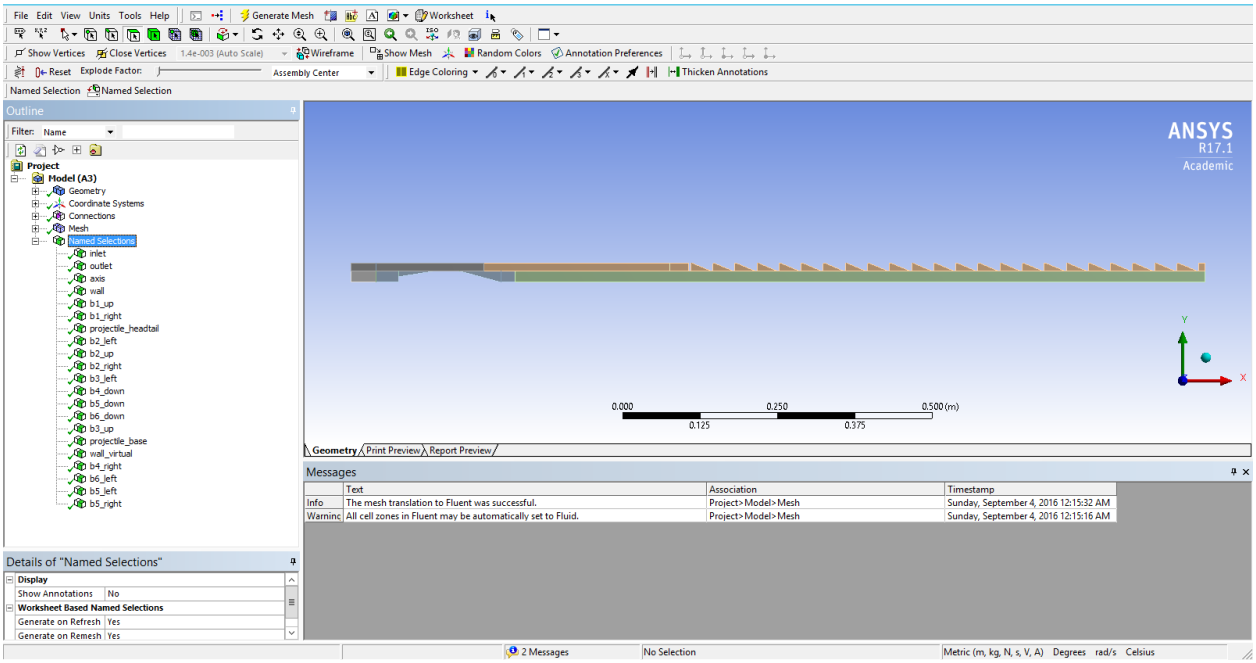

Figure D. ANSYS-Fluent-Mesh interface with toolbar at the top. Connection, mesh and name selections are shown under outline on the left. Generic axisymmetric 23° aftward-slanted BTRA configuration computational domains shown on the right.

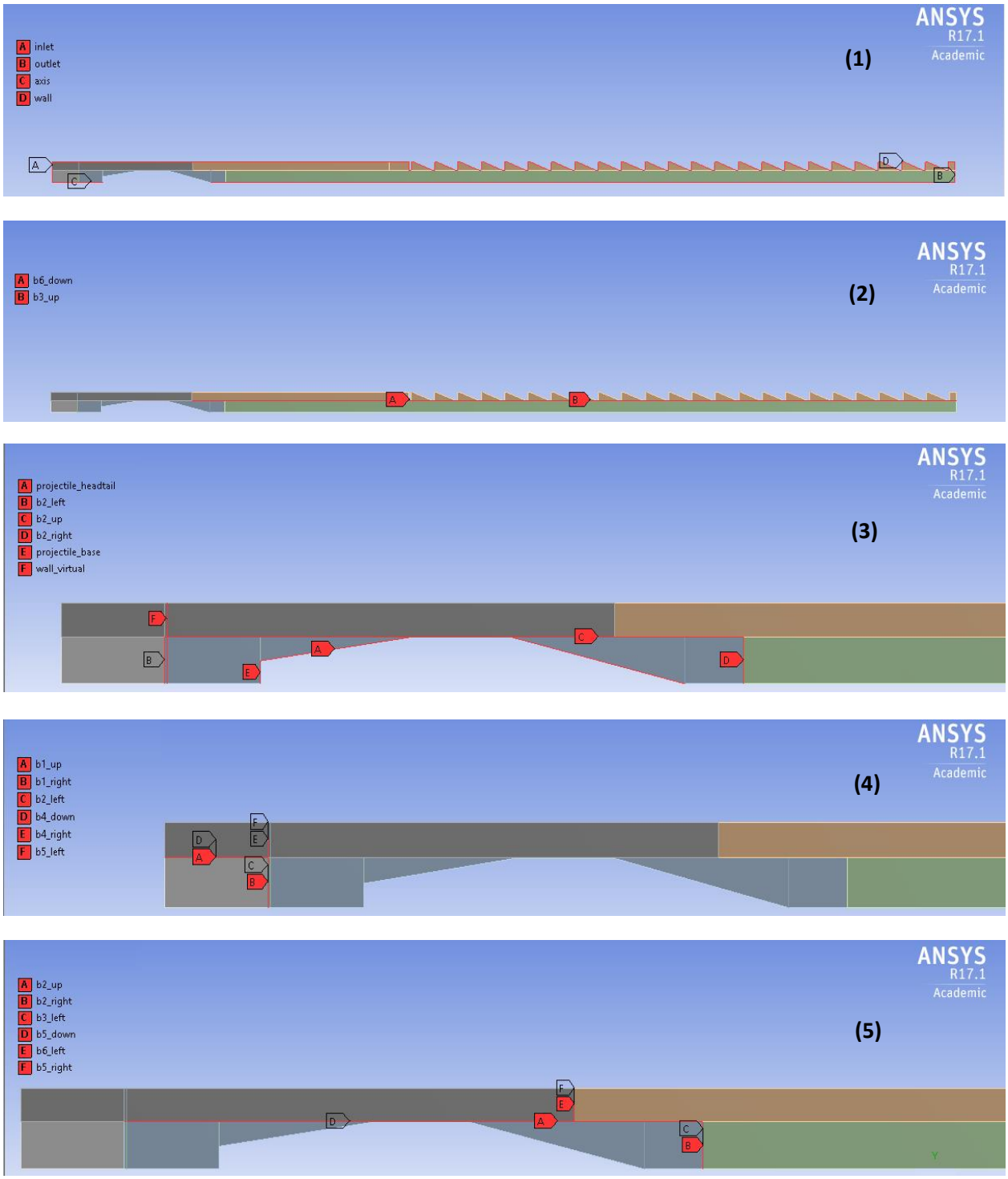

Figure E. shows Inlet, outlet, baffled tube walls and axis of symmetry (1), connection region between lower face of baffled tube section with upper face of deforming region ahead of the projectile (2), projectile and the interfaces around it with the virtual wall (3), connection of interfaces and domains behind the projectile relative to each other (4) and connection of interfaces and domains ahead of the projectile relative to each other (5).

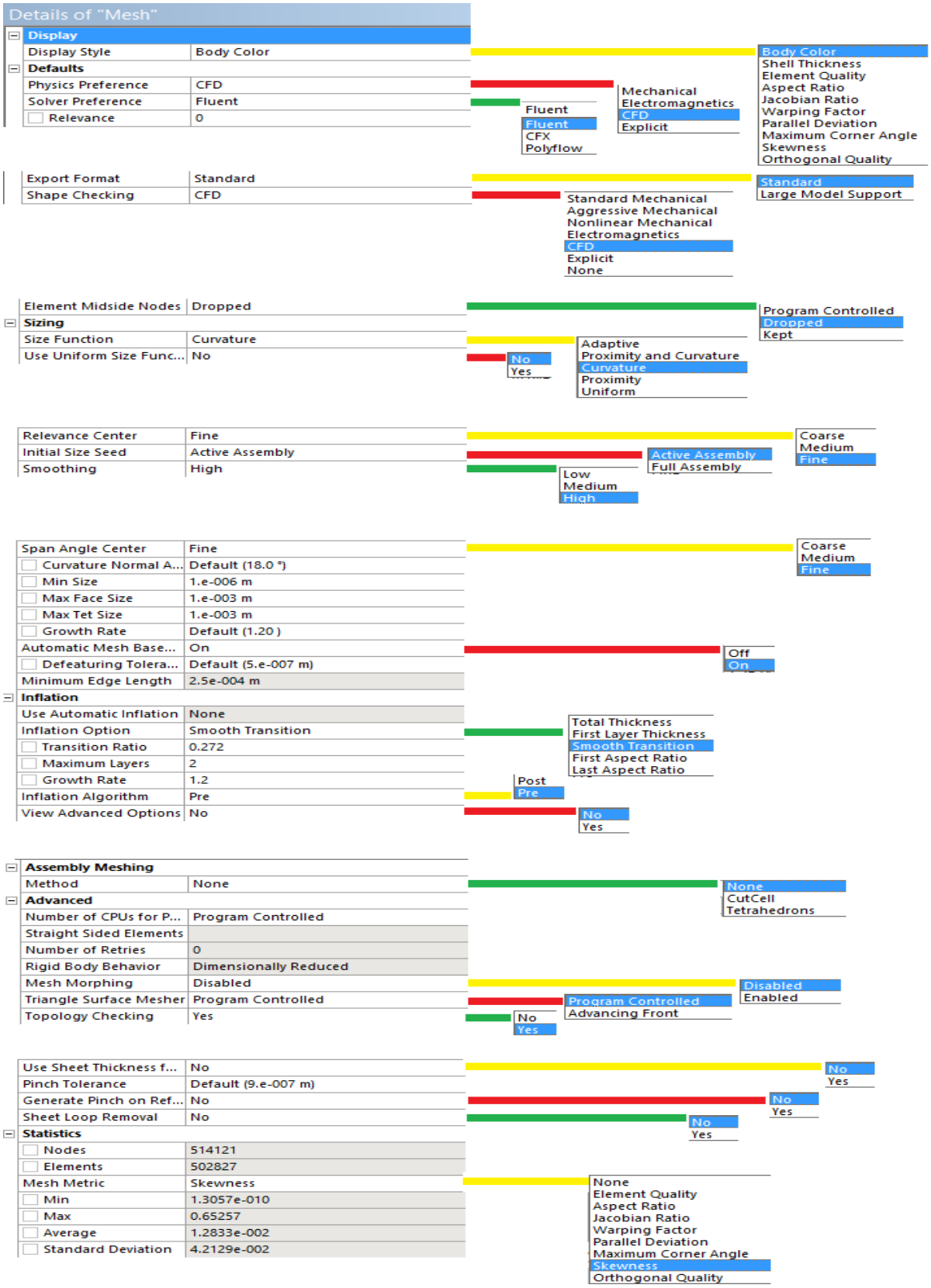

Figure F. Generic default setup for mesh sizing.

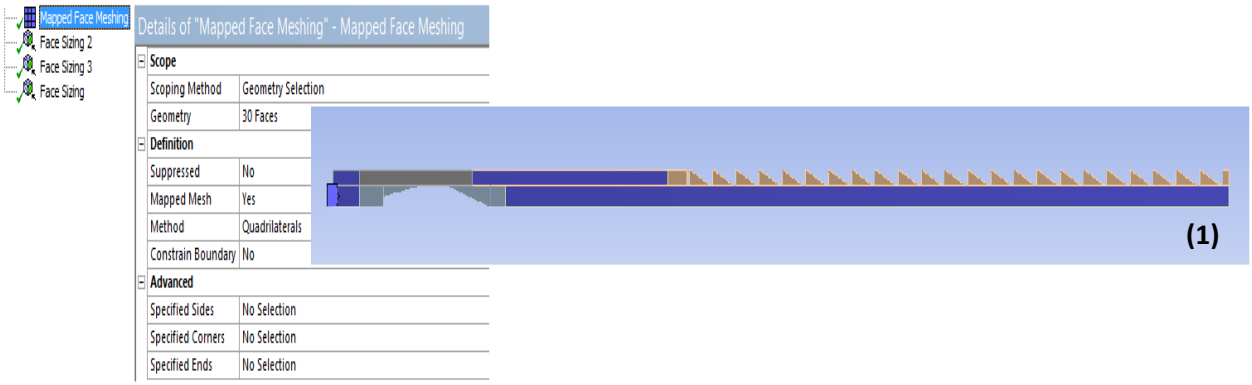

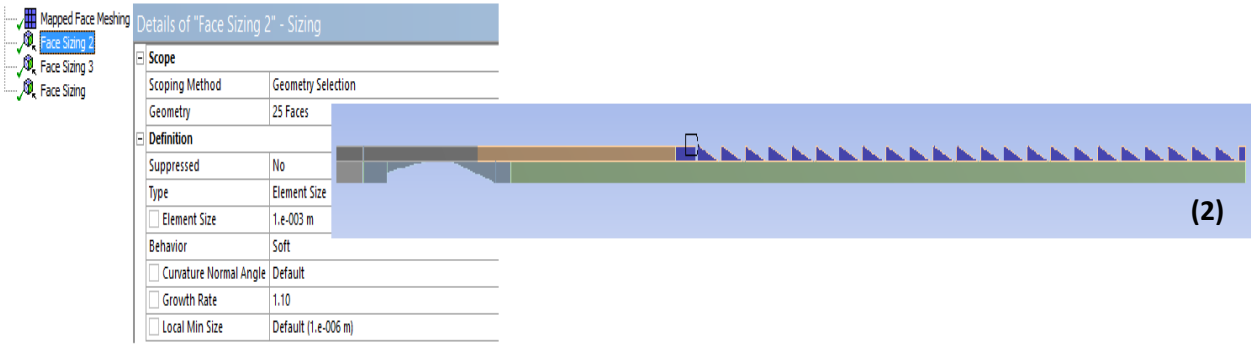

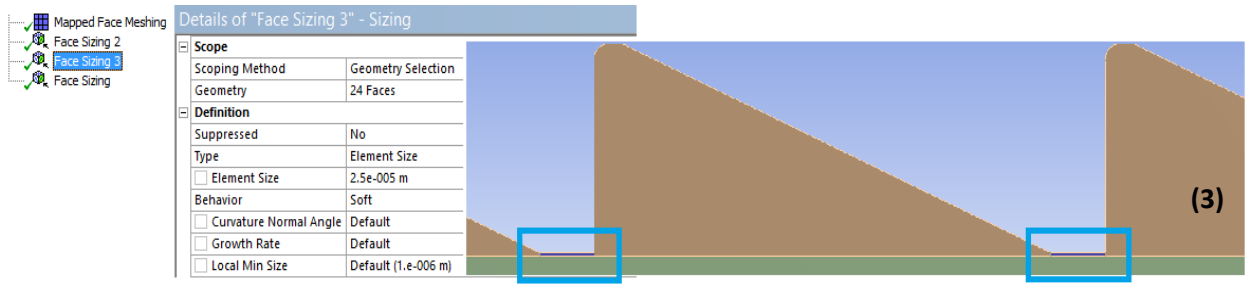

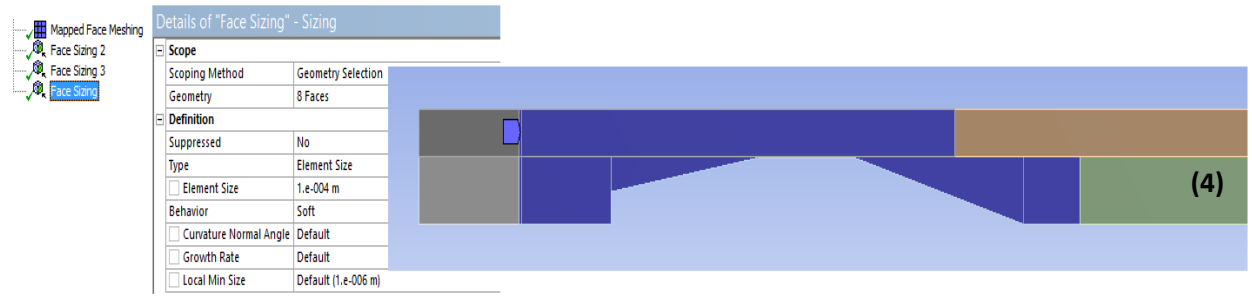

Figure G. Specific cell sizing on deforming regions (1), baffle tube region (2), minimum gap between shoulder of the projectile and baffle wall (3) and rigid regions (4).

Appendix C

Fluent – Solver Inputs

In this section, settings of Fluent solver are illustrated in series of figures (Figs. H1-57) and there are few key points to pay attention to prior running any case:

1. Fluent solver has a lot of variables and options that can adjusted based on the various cases. Routinely usage of ANSYS Fluent guides [29, 31] is highly recommended at all time.
2. Many domains and interfaces such as boundary conditions and dynamic mesh regions have similar functionality in the computational domain. Assure all domains and interfaces have proper inputs.
3. Using pressure-based solver in lieu of density-based solver varies multiple inputs used in solver's setup especially in combustion modeling.
4. A user-defined-function (UDF) was written in C++ and used to assign constant velocity to various interfaces and domains. UDF must be compiled in the same directory as the case. Usage of ANSYS Fluent UDF manual [30] is necessary to update and upgrade the current code if one needs to advance BTRA study to variable velocity cases. The description of the UDF used in this study is shown below;

```
#include "udf.h"
#include "dynamesh_tools.h"
/* Projectile, Interface and Domains Motion */
DEFINE_CG_MOTION(projectile, dt, vel, omega, time, dtime)
{
Thread *t;
face_t f;
vel[0]=1500;
}
```

5. Since obtaining a single solution in reactive flow study took about 8-10 days, it is highly recommended to monitor the residuals of conservation equations routinely. Also, it is utterly important to know which flow variables to save and be cognizant of how often to save full datasets. Having a series of full dataset allows scrutinizing the flow variables, leaves room for diagnostics and restarting a case if a divergence occurs in the solution.
6. The variables that were collected routinely to allow data analysis during post processing were: static pressure, static temperature, Mach, velocity, density, speed of sound, mass and mole fractions of CH_4, O_2, CO, CO_2 and H_2O.

The process of setting up the Fluent solver is time consuming in general and requires inputting variables and changing options carefully. However, designing an elegant computational domain based on knowing what information need to be extracted from the solution could ease solver setup and post-processing data.

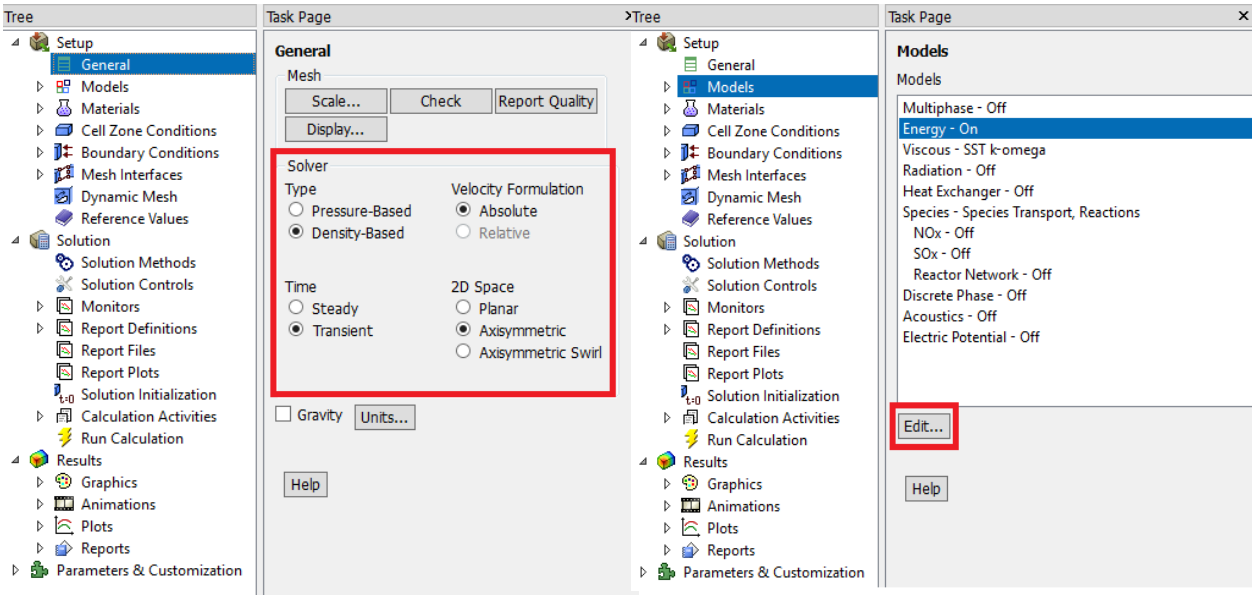

Figure H1 and –2. ANSYS-Fluent-Solver setup.

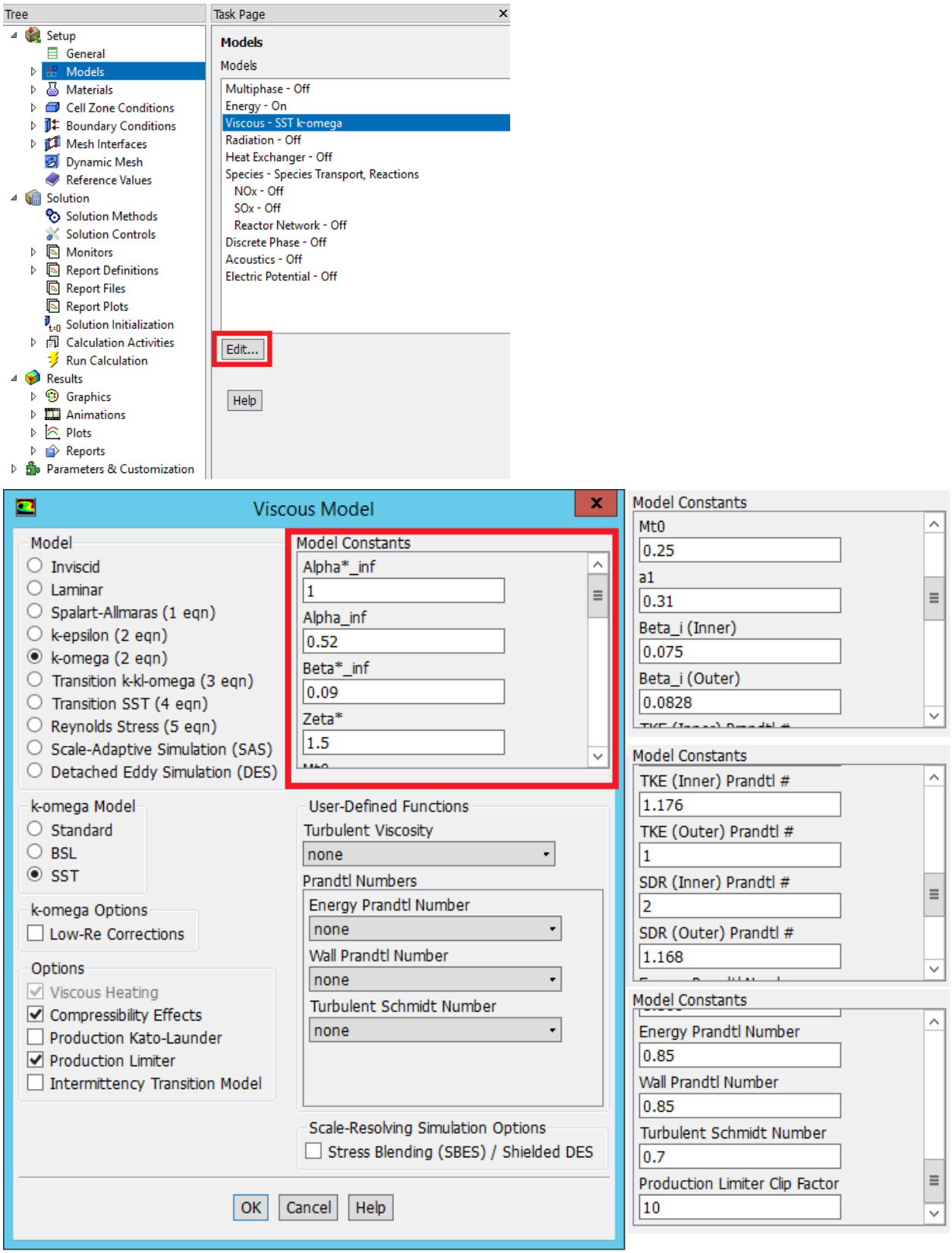

Figure H3 and –4. ANSYS-Fluent-Solver setup.

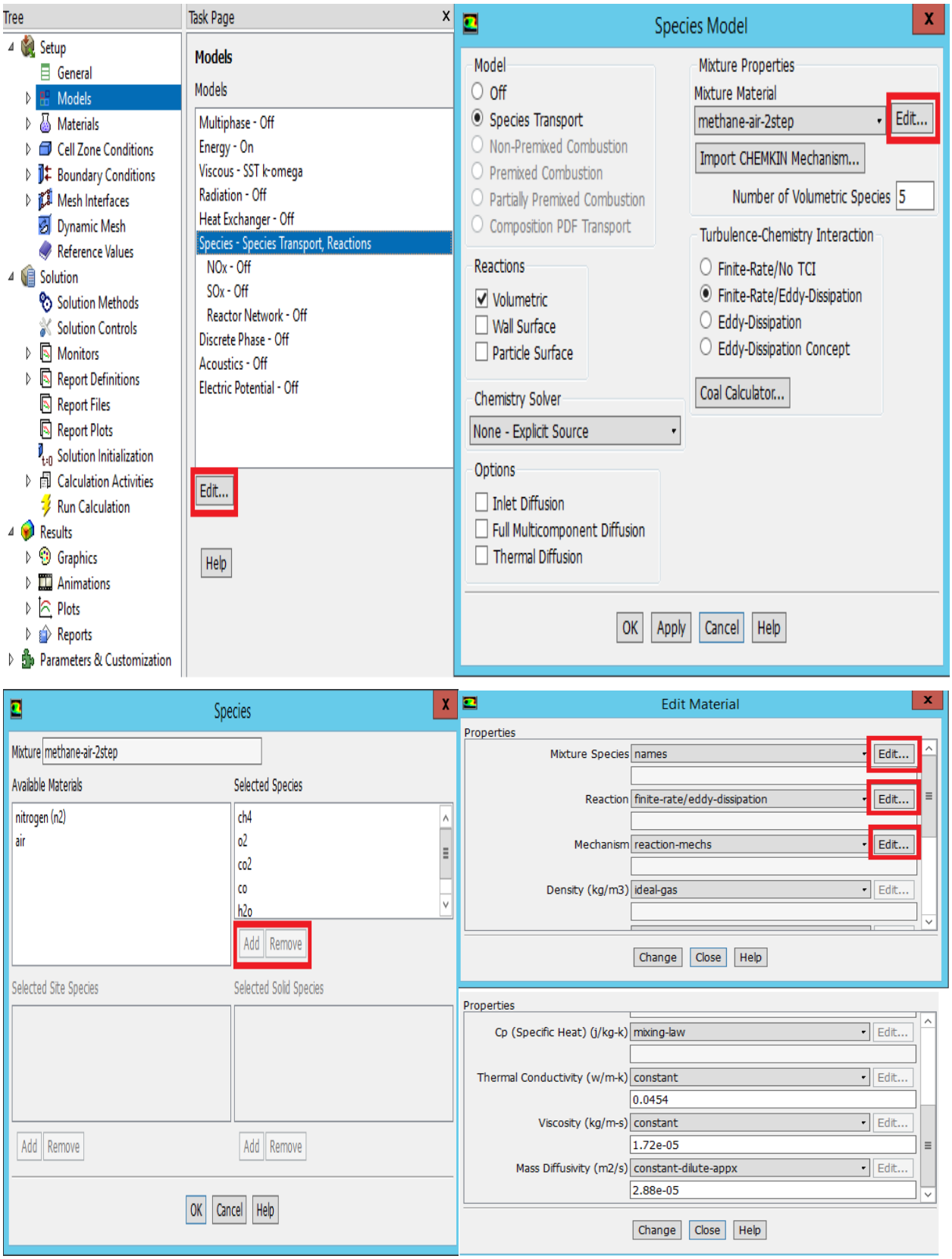

Figure H5 thru –8. ANSYS-Fluent-Solver setup.

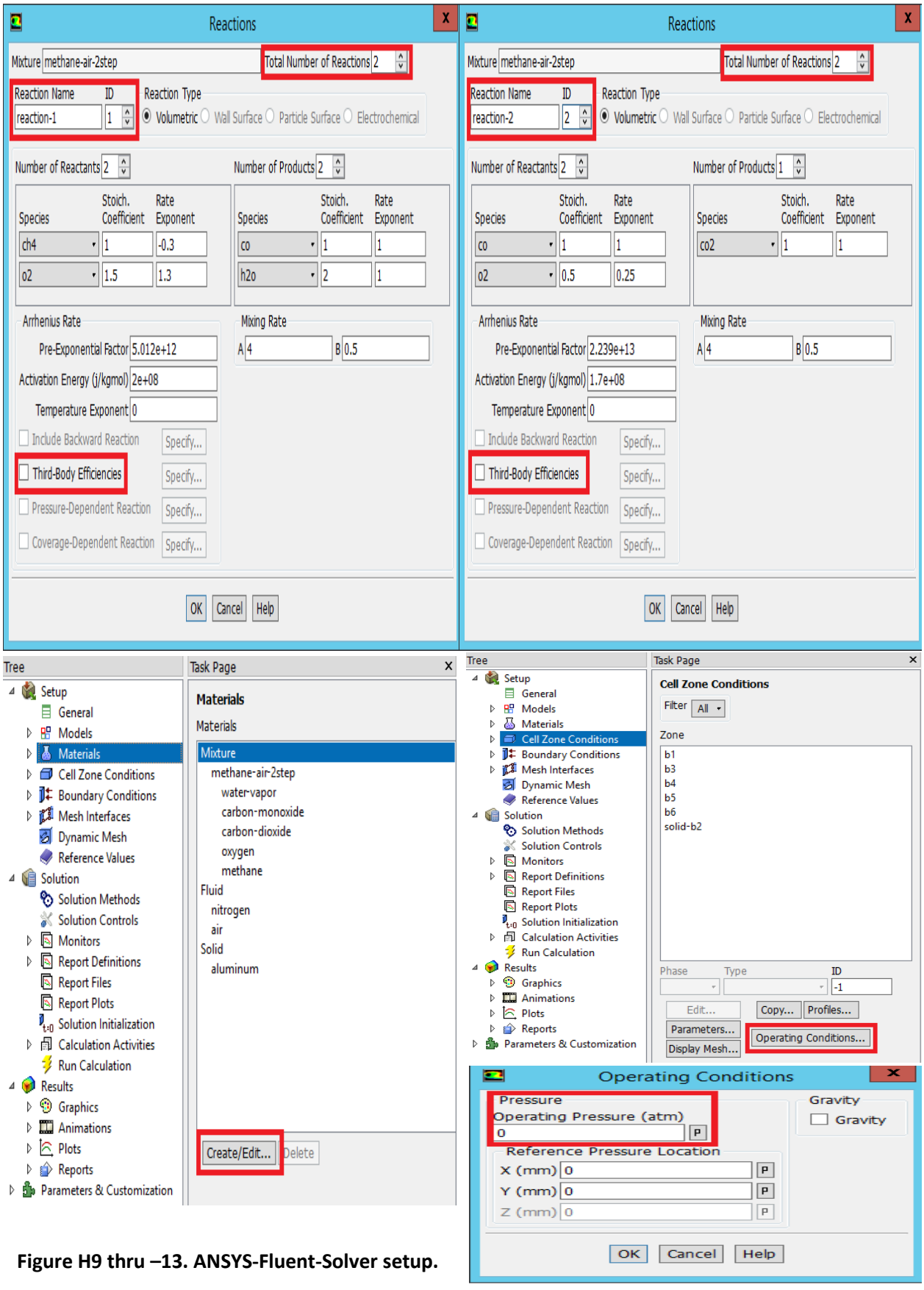

Figure H9 thru –13. ANSYS-Fluent-Solver setup.

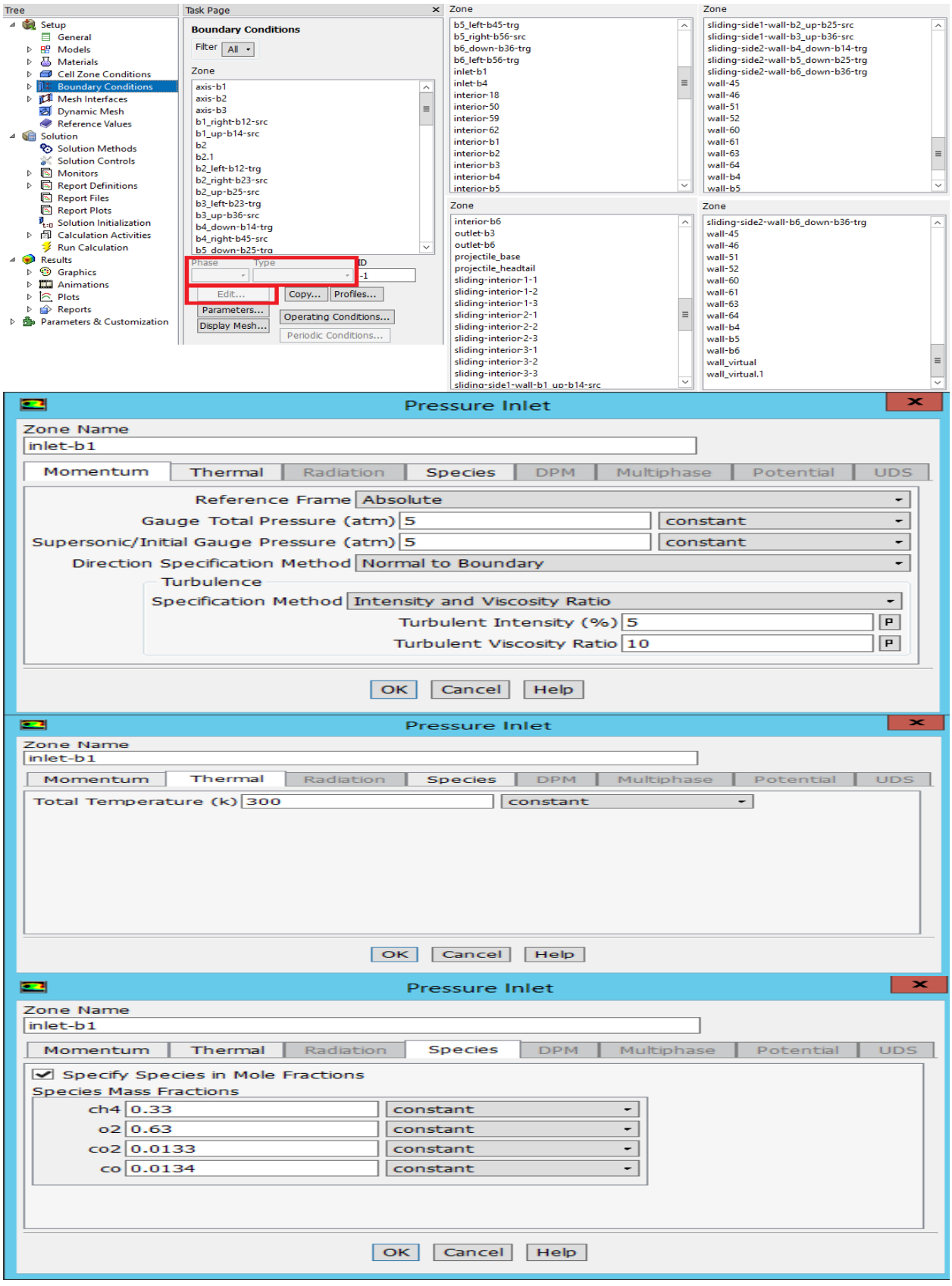

Figure H14 thru –17. ANSYS-Fluent-Solver setup.

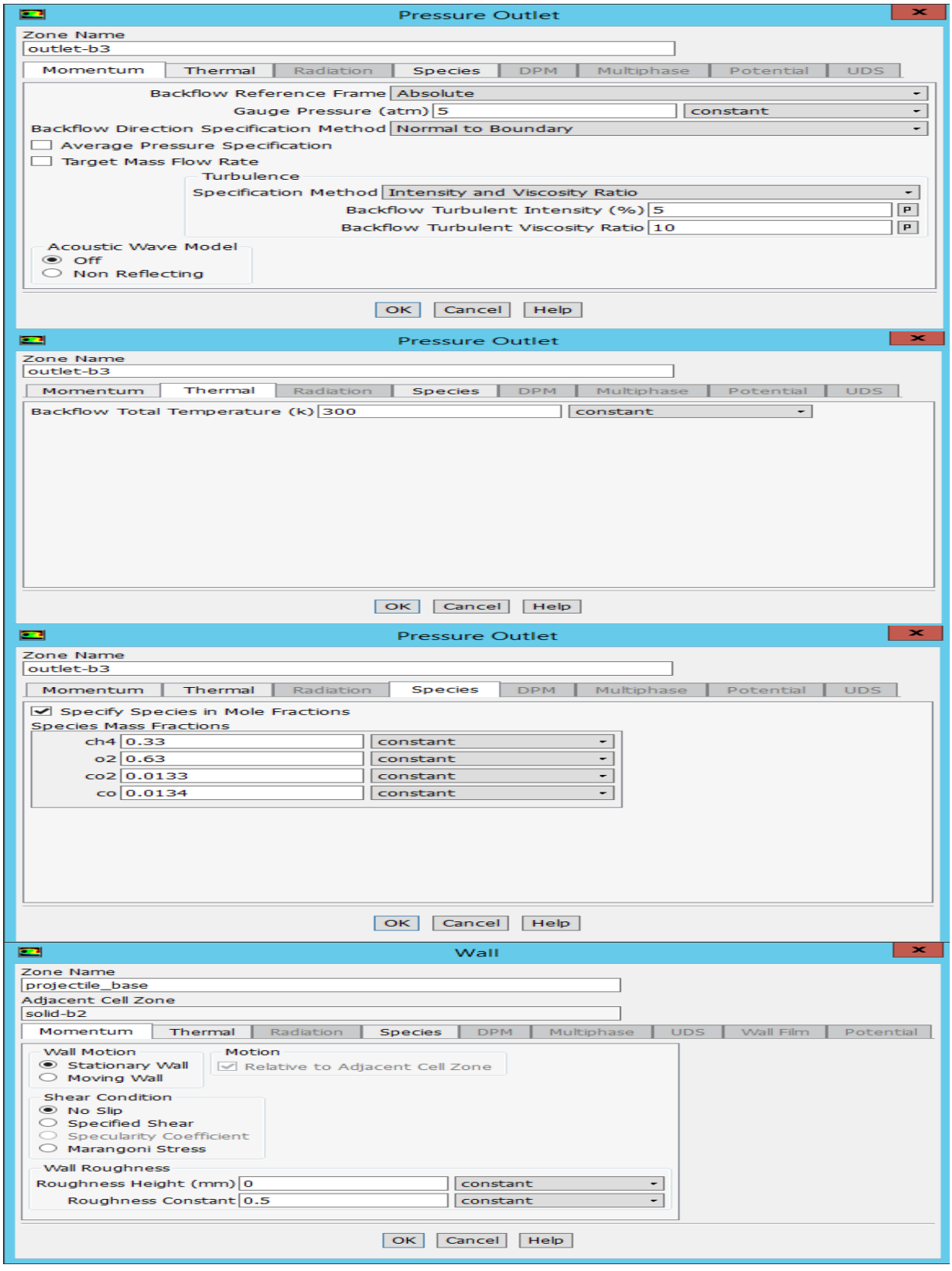

Figure H18 thru –21. ANSYS-Fluent-Solver setup.

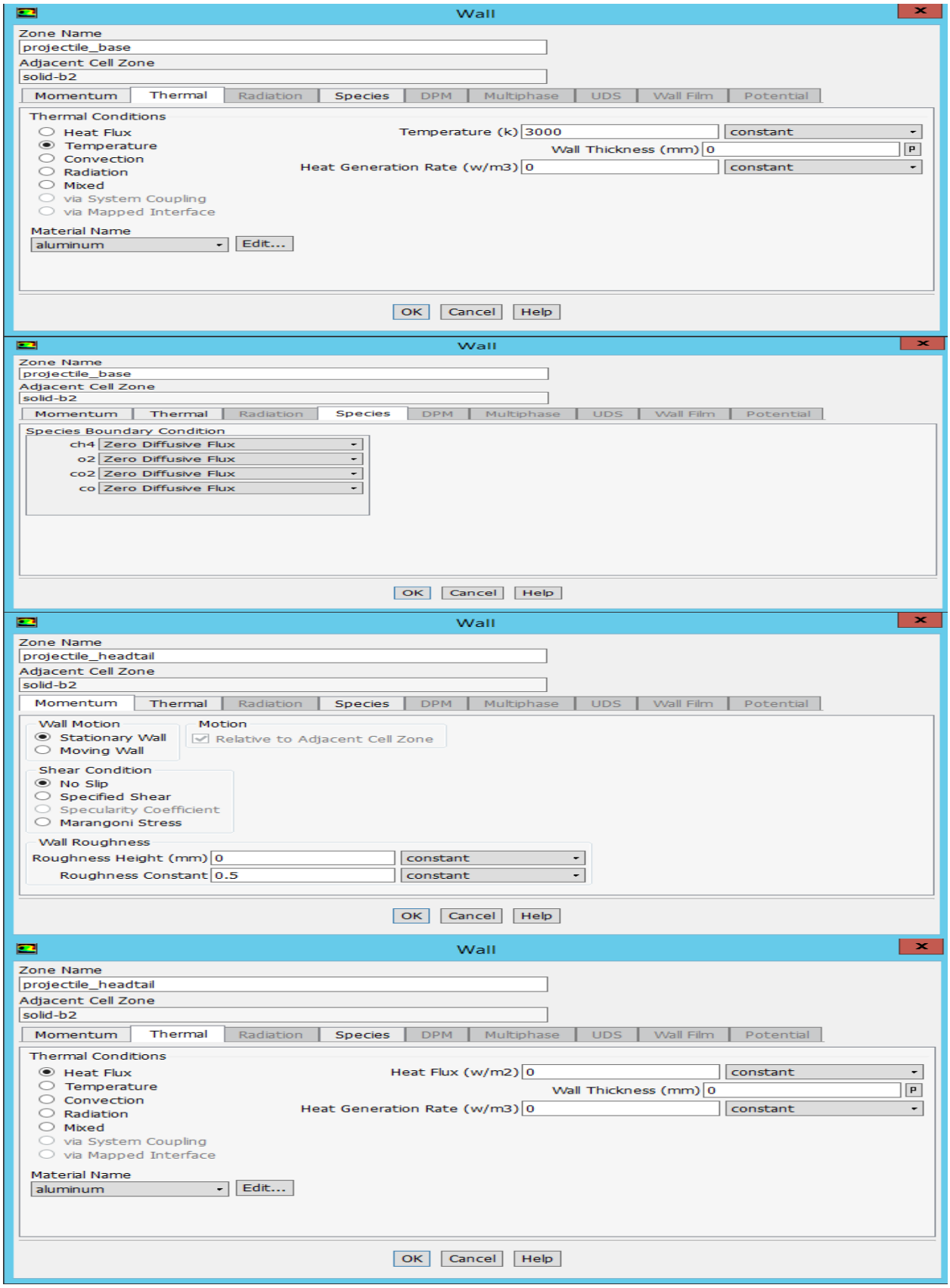

Figure H22 thru –25. ANSYS-Fluent-Solver setup.

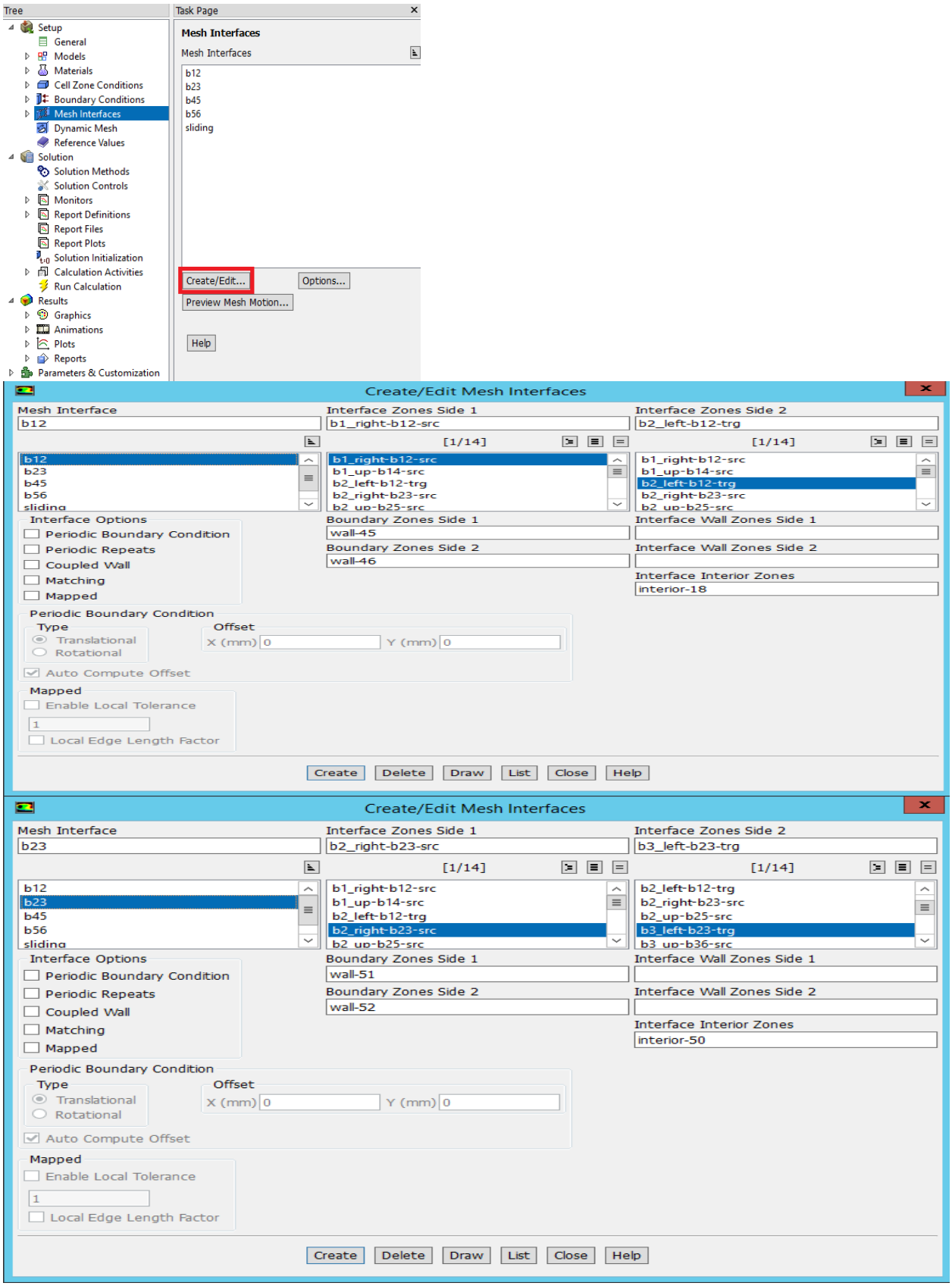

Figure H26 thru –28. ANSYS-Fluent-Solver setup.

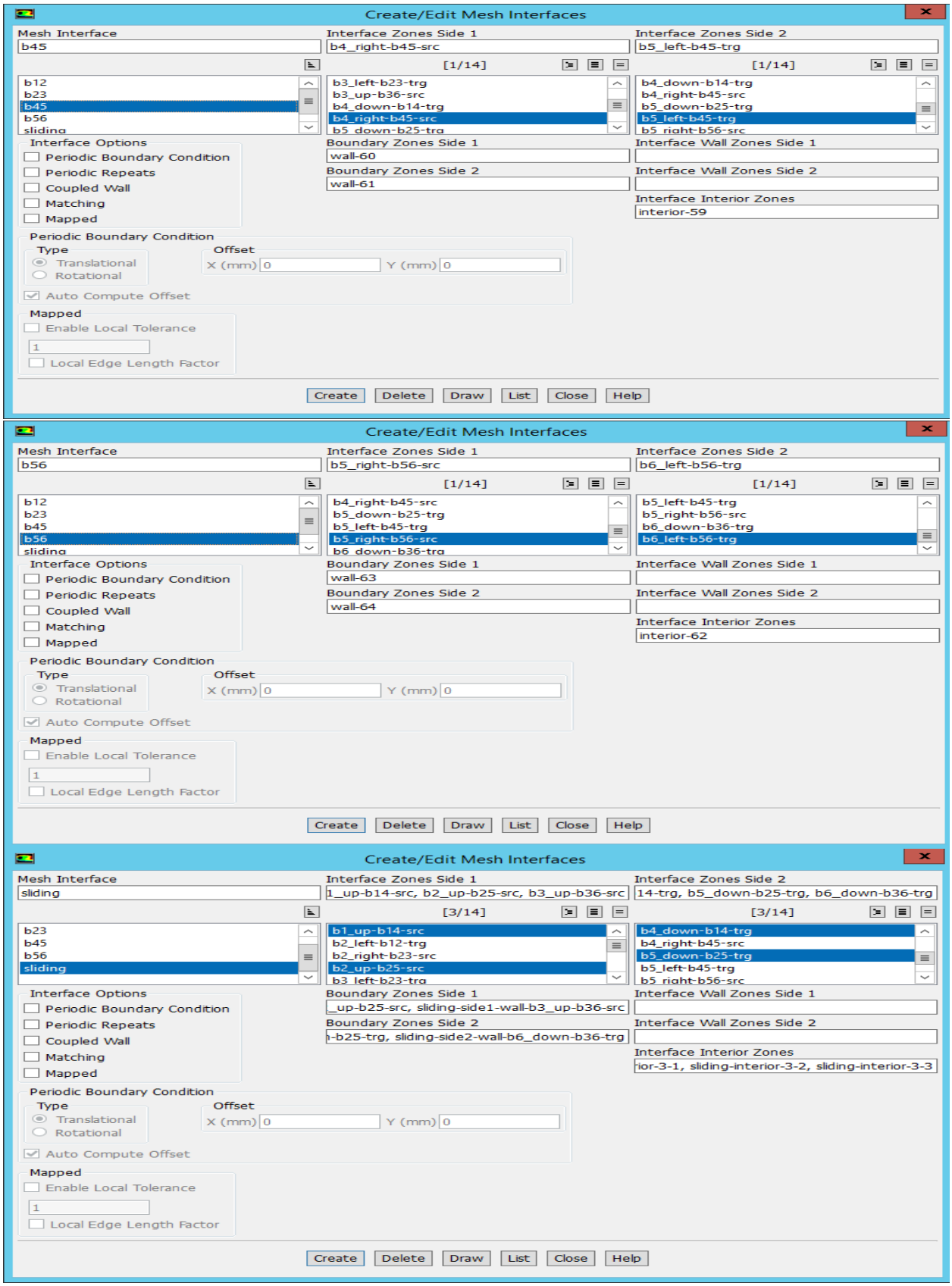

Figure H29 thru –31. ANSYS-Fluent-Solver setup.

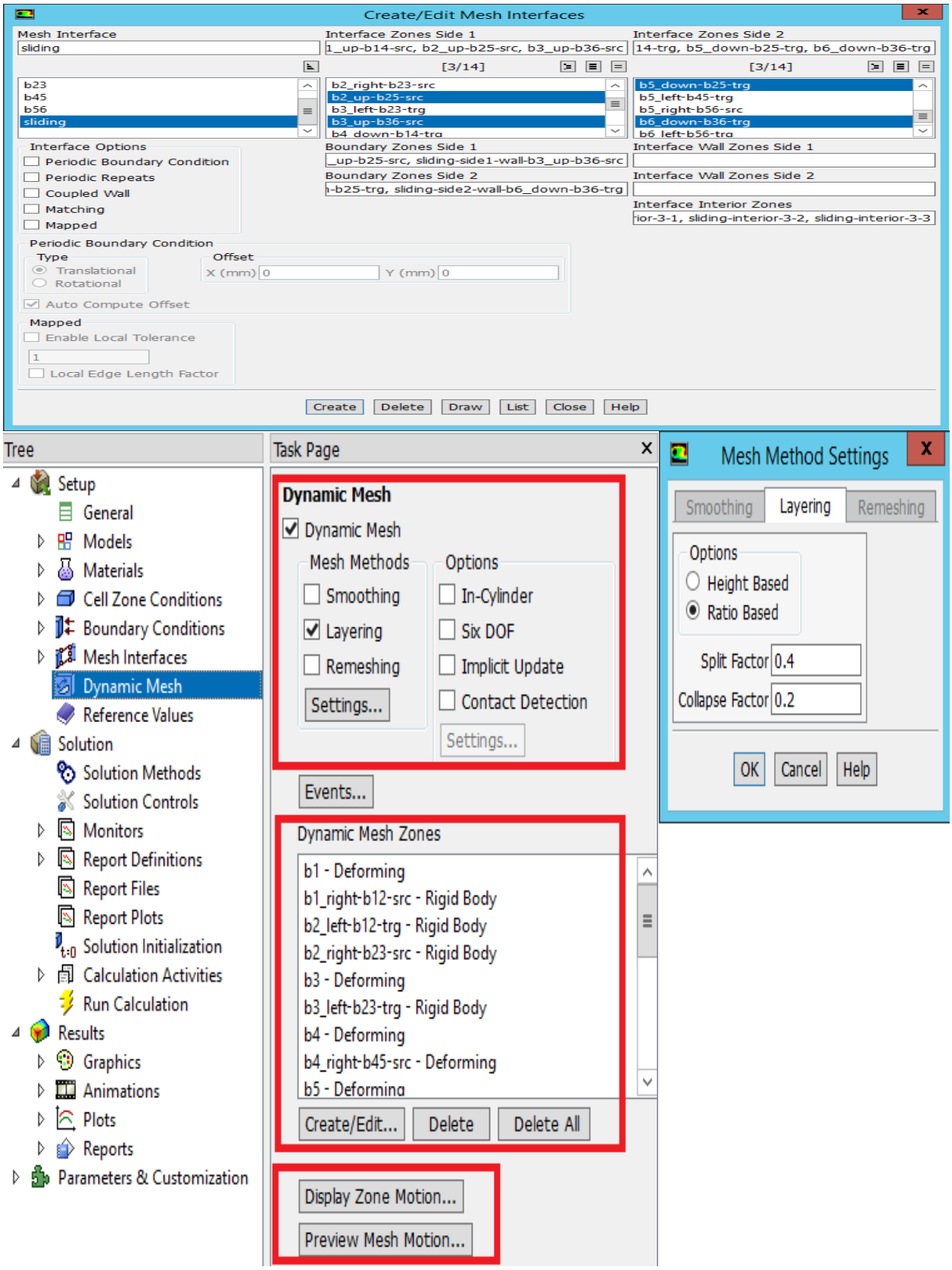

Figure H32 thru –34. ANSYS-Fluent-Solver setup.

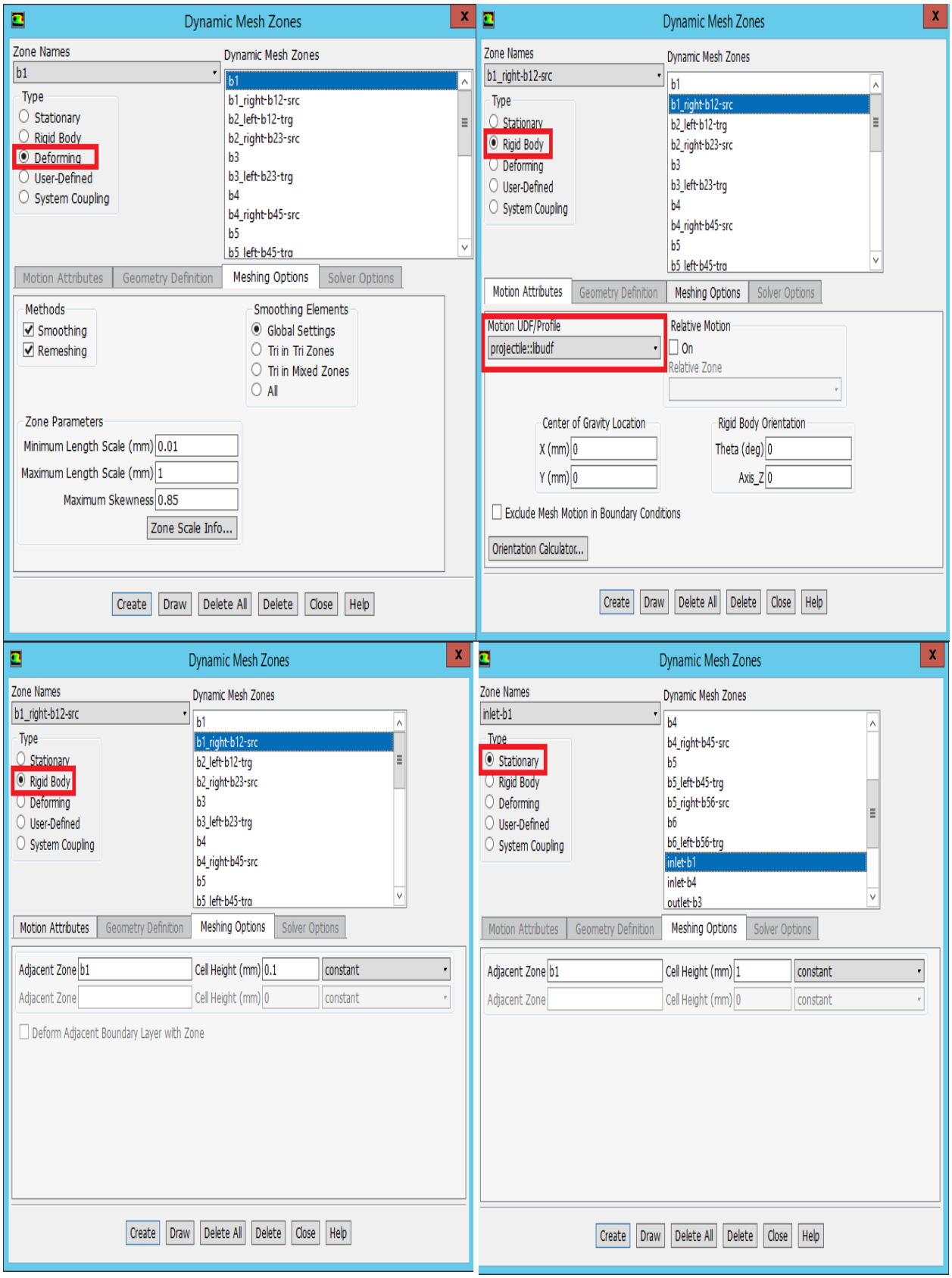

Figure H35 thru –38. ANSYS-Fluent-Solver setup.

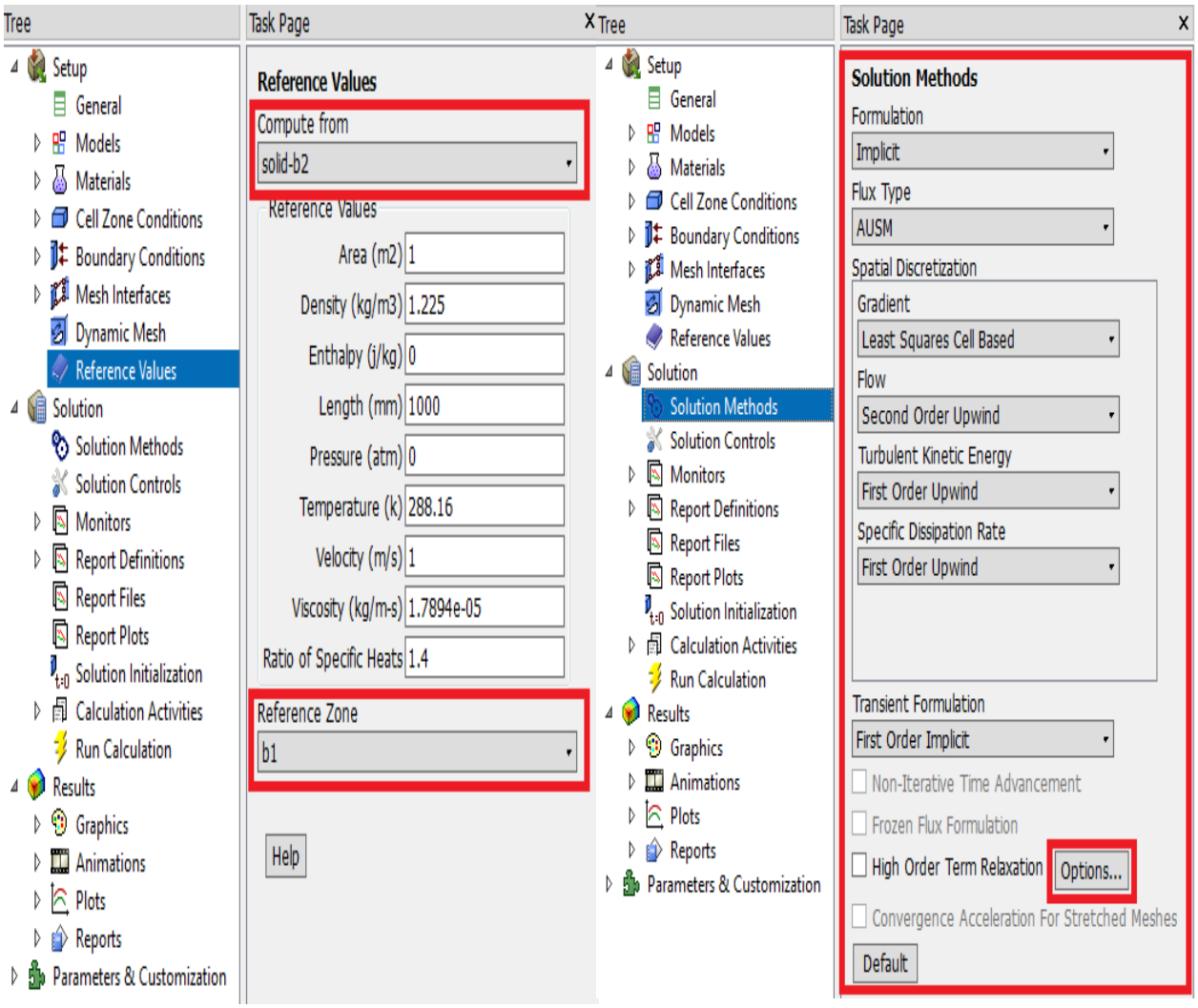

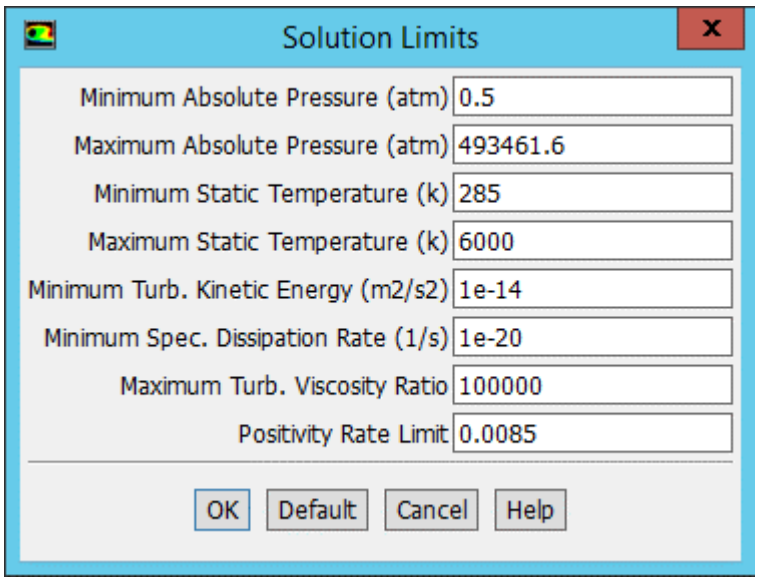

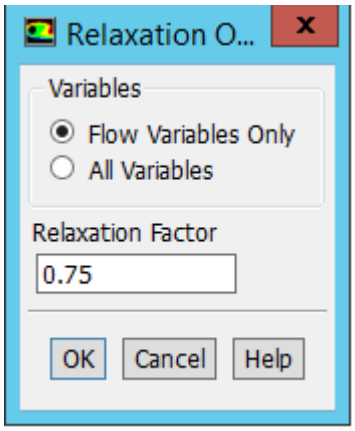

Figure H39 thru –42. ANSYS-Fluent-Solver setup.

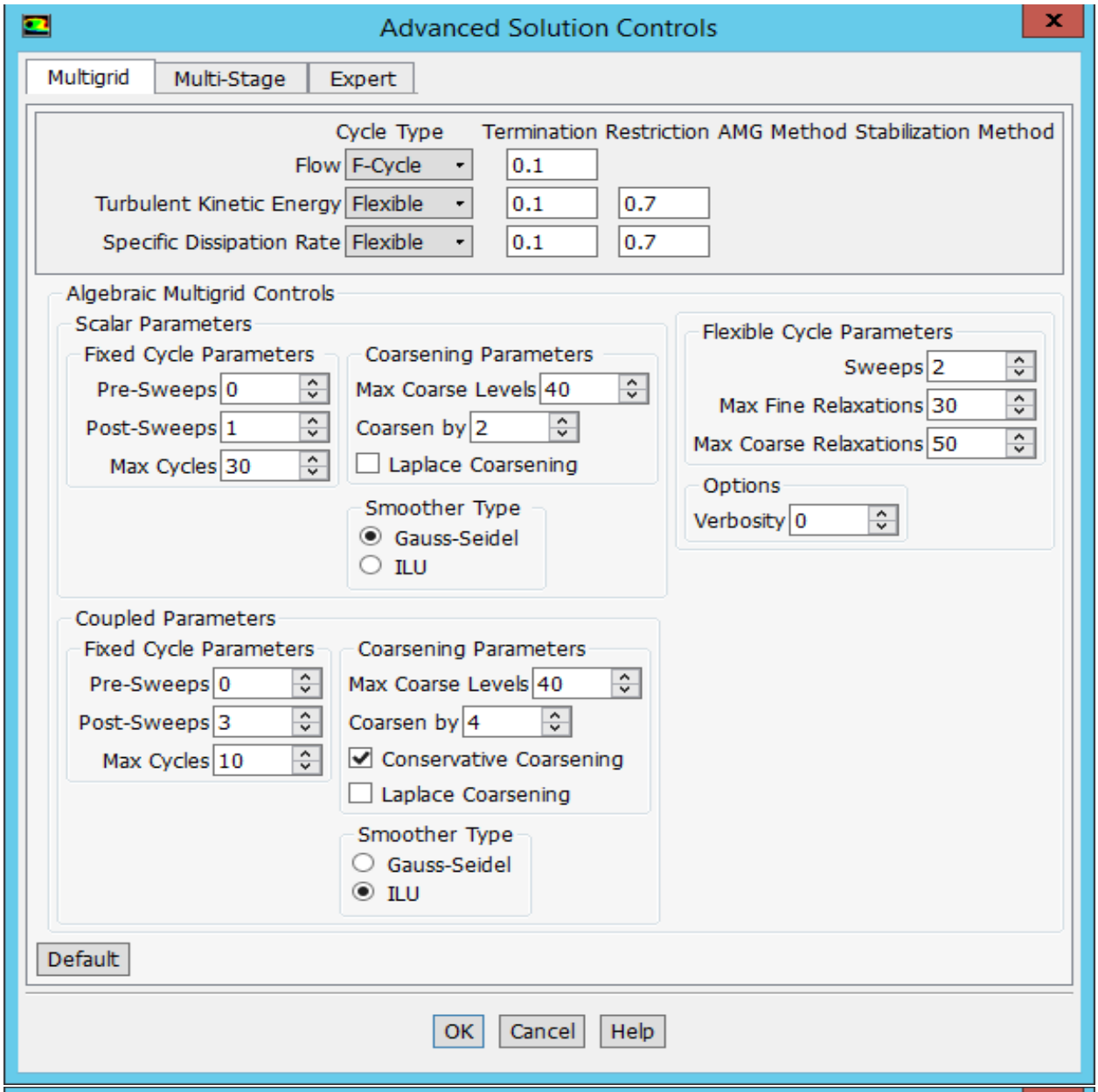

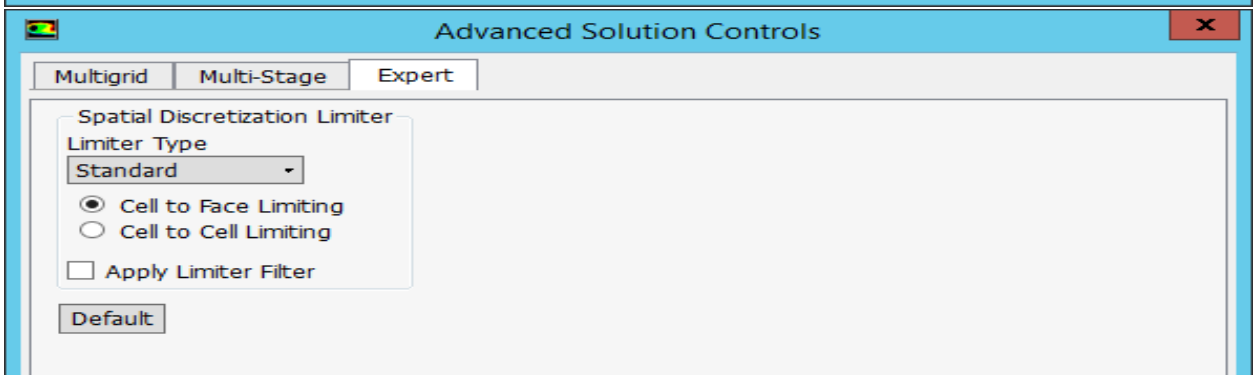

Figure H43 and –44. ANSYS-Fluent-Solver setup.

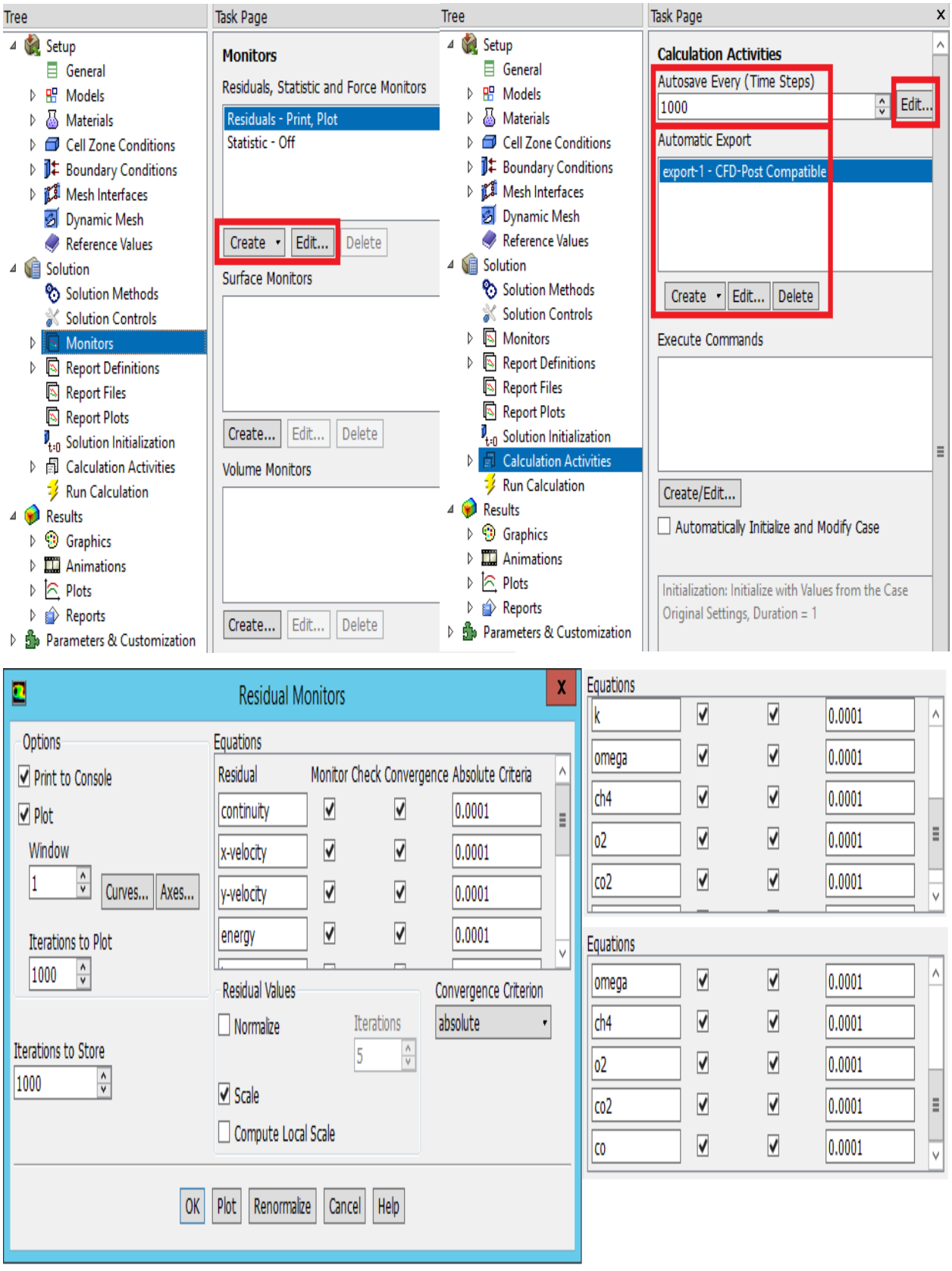

Figure H45 thru –47. ANSYS-Fluent-Solver setup.

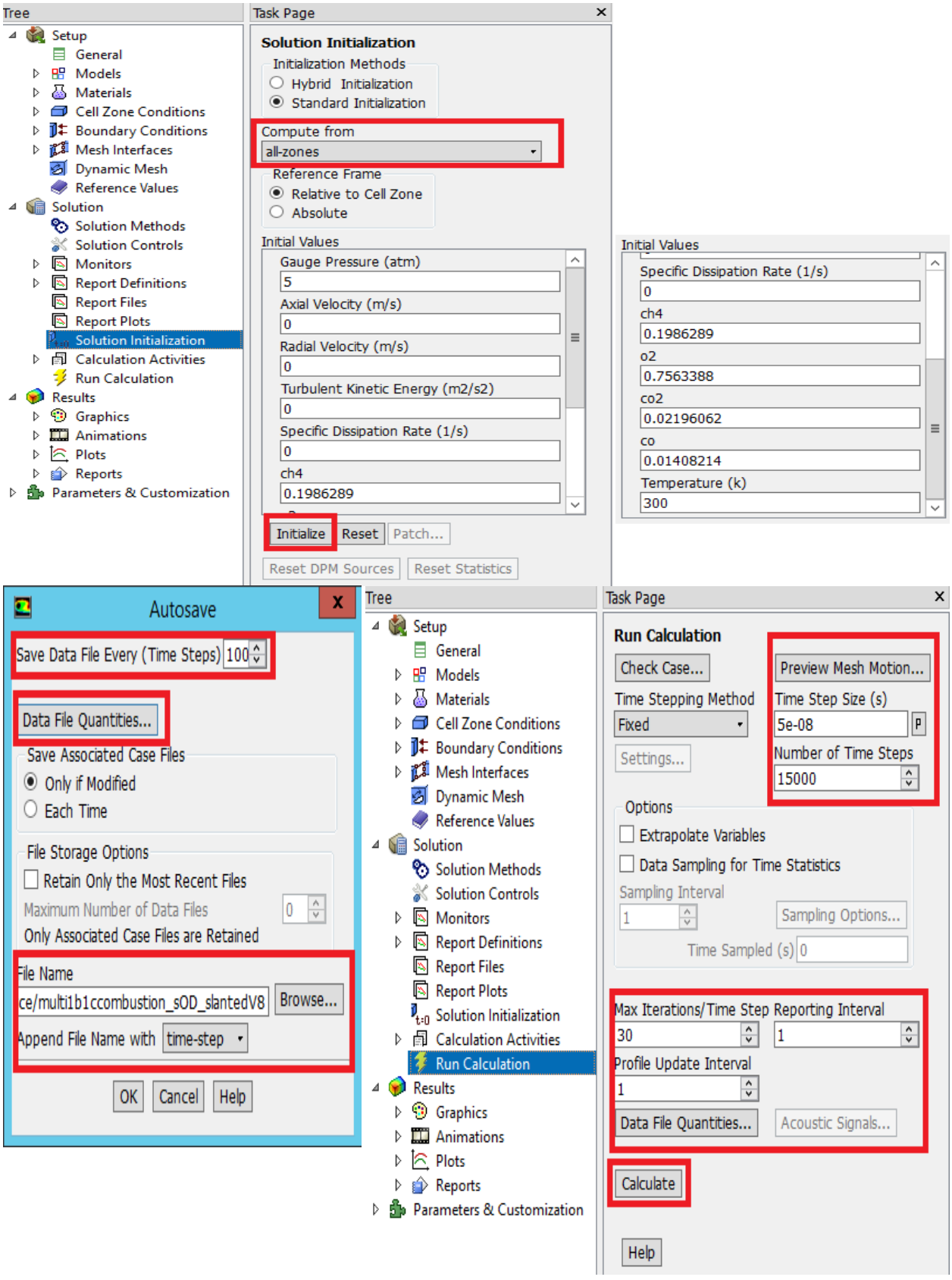

Figure H48 thru –50. ANSYS-Fluent-Solver setup.

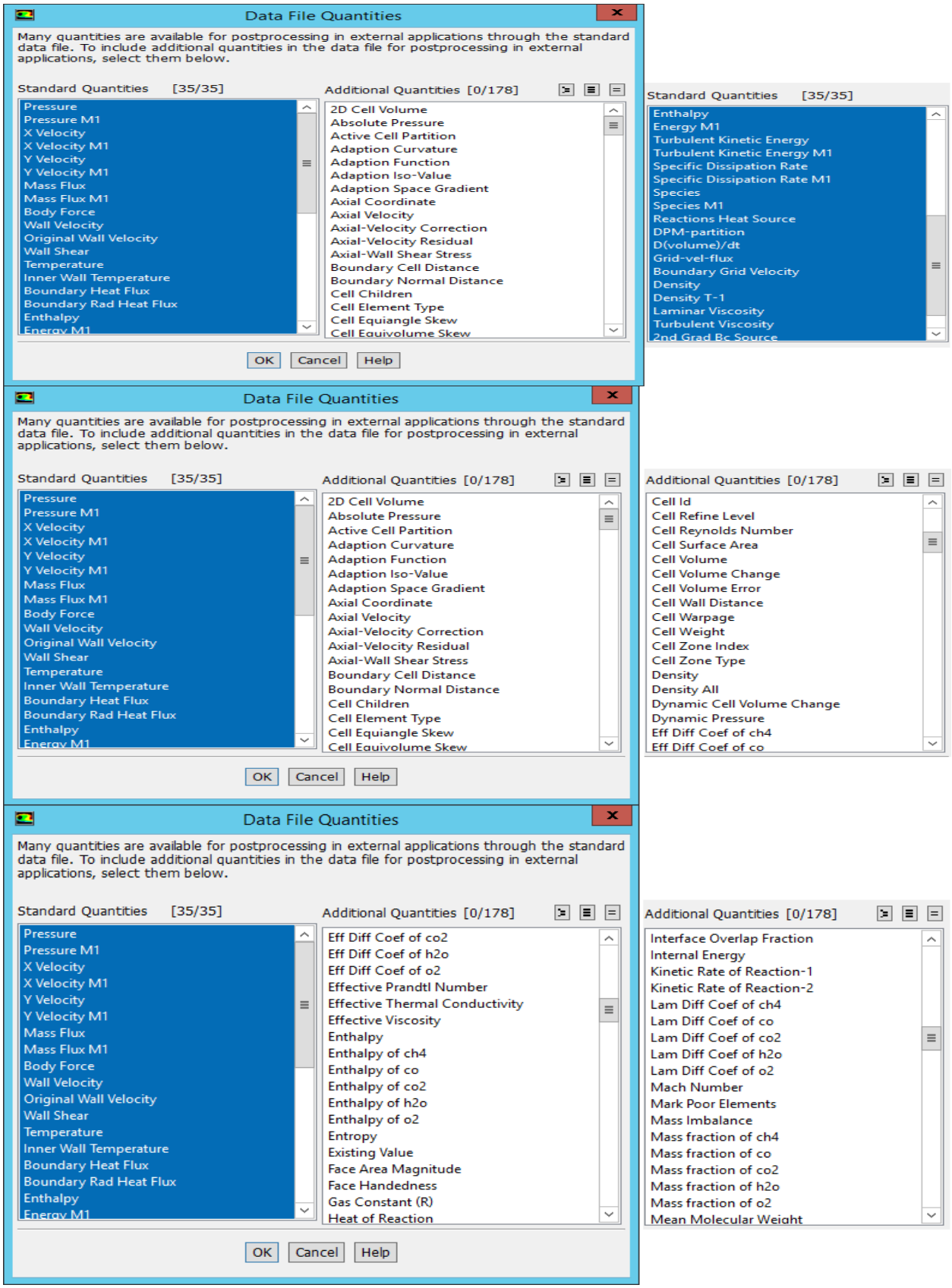

Figure H51 thru –53. ANSYS-Fluent-Solver setup.

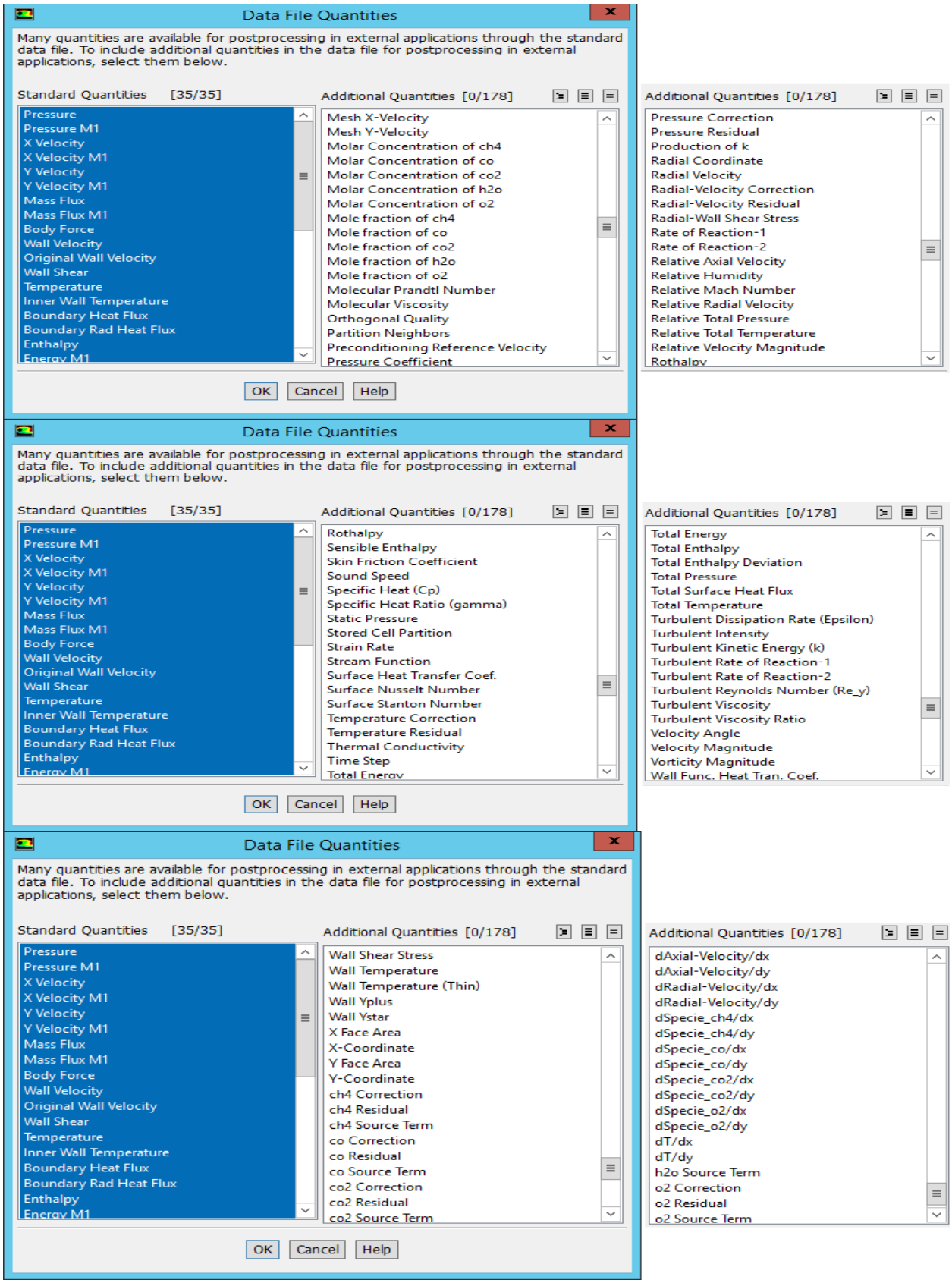

Figure H54 thru –56. ANSYS-Fluent-Solver setup.

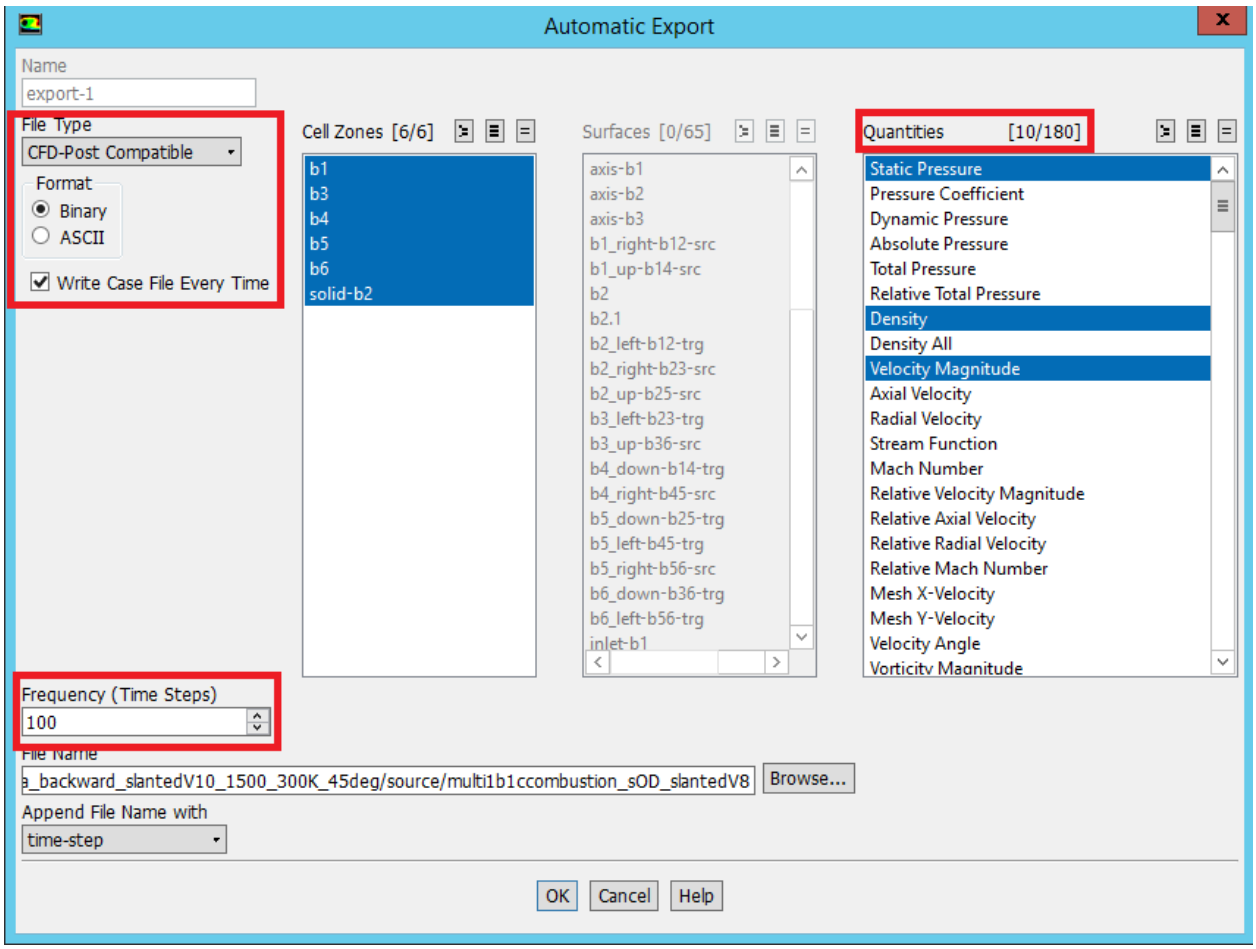

Figure H57. ANSYS-Fluent-Solver setup.

Appendix D

MATLAB scripts

```
% ------------------------------------------------------- %
% Thrust vs. Mach %
clear all;
clc

x=[2.91 3.49 4.37 4.66 5.09];

T23=[8859 5826 1090 -238 NaN];
T45=[4243 1951 1150 898 100];

P23=polyfit(x(1:4),T23(1:4),1)
P45n1=polyfit(x,T45,1)
P45n2=polyfit(x,T45,2)
P45n3=polyfit(x,T45,3)
Mp=1:0.1:6;
Y23=polyval(P23,Mp);
Y45n1=polyval(P45n1,Mp);
Y45n2=polyval(P45n2,Mp);
Y45n3=polyval(P45n3,Mp);

set(gcf,'color','w');
set(0,'defaultfigureposition',[100 100 800 600])
grid on
figure(1)
plot(x,T23,'r+','linewidth',20)
axis([1 6 -1000 12000])
set(gca,'Fontsize',[15])
xlabel('Mach')
ylabel('Thrust (N)')
title('BTRA Thrust vs. Mach')
hold on
plot(x,T45,'bO','linewidth',10)
plot(Mp,Y23,'--r','linewidth',3)
plot(Mp,Y45n3,'--b','linewidth',3)
legend('23(deg)','45(deg)','23(deg),n=1','45(deg),n=3',...
    'location','northeast')
grid on
hold off
% ------------------------------------------------------- %
% Baffle-drag variations as a function of number of dataset %
% 1200 m/sec (M = 3.49) in 23 degree BTRA configuration %

clc
```

```
clear all

X1=linspace(10,20,11)';
Y1=[4342.50,14384.60,6144.60,1597.40,7153.00,...
    2255.51,1802.80,777.00,4665.10,3771.91,8438.88]';
p1=polyfit(X1,Y1,7);
x1=linspace(10,20);
y1=polyval(p1,x1);

X2=linspace(10,20,10)';
Y2=[10881.70,11800.60,4030.40,3714.60,8794.71,...
    4386.80,2891.20,646.90,2130.20,1796.57]';
p2=polyfit(X2,Y2,7);
y2=polyval(p2,x1);

X3=linspace(10,20,9)';
Y3=[8297.70,9686.40,9342.40,5356.31,2152.40,...
    5475.20,1467.30,3181.80,3438.28]';
p3=polyfit(X3,Y3,7);
y3=polyval(p3,x1);

X4=linspace(10,20,8)';
Y4=[6183.50,14998.40,10984.11,1286.00,1064.00,...
    4051.30,1067.60,8750.28]';
p4=polyfit(X4,Y4,7);
y4=polyval(p4,x1);

X5=linspace(10,20,7)';
Y5=[11495.50,16640.11,4341.80,2374.40,...
    2487.90,1516.40,6636.08]';
p5=polyfit(X5,Y5,7);
y5=polyval(p5,x1);

X6=linspace(10,20,6)';
Y6=[13137.21,9997.80,3253.40,950.50,...
    5022.80,4052.08]';
p6=polyfit(X6,Y6,7);
y6=polyval(p6,x1);

X7=linspace(10,20,5)';
Y7=[6494.90,8909.40,4677.30,1584.40,10591.28]';
p7=polyfit(X7,Y7,7);
y7=polyval(p7,x1);

X8=linspace(10,20,4)';
Y8=[5406.50,10333.30,7212.20,7152.88]';
p8=polyfit(X8,Y8,7);
y8=polyval(p8,x1);

X9=linspace(10,20,3)';
Y9=[6830.40,12868.20,12780.68]';
p9=polyfit(X9,Y9,7);
y9=polyval(p9,x1);
```

```
figure(1)
set(gcf,'color','w');
set(0,'defaultfigureposition',[100 100 800 600])
set(gca,'Fontsize',[15])
plot(x1,y1,'Linewidth',3,'color',[0.502 0.251 0])
grid on
axis([10 20 -1000 27500])
hold on
plot(x1,y2,'Linewidth',3,'color',[0.251 0 0.502])
plot(x1,y3,'Linewidth',3,'color',[0 1 0])
plot(x1,y4,'Linewidth',3,'color',[1 0.502 1])
plot(x1,y5,'Linewidth',3,'color',[1 0 0])
plot(x1,y6,'Linewidth',3,'color',[0 1 1])
plot(x1,y7,'Linewidth',3,'color',[0.9412 0.4706 0])
plot(x1,y8,'Linewidth',3,'color',[0 0 0])
plot(x1,y9,'Linewidth',3,'color',[0 0 1])

plot(X1,Y1,'s','Linewidth',3,'color',[0.502 0.251 0])
plot(X2,Y2,'s','Linewidth',3,'color',[0.251 0 0.502])
plot(X3,Y3,'s','Linewidth',3,'color',[0 1 0])
plot(X4,Y4,'s','Linewidth',3,'color',[1 0.502 1])
plot(X5,Y5,'s','Linewidth',3,'color',[1 0 0])
plot(X6,Y6,'s','Linewidth',3,'color',[0 1 1])
plot(X7,Y7,'s','Linewidth',3,'color',[0.9412 0.4706 0])
plot(X8,Y8,'s','Linewidth',3,'color',[0 0 0])
plot(X9,Y9,'s','Linewidth',3,'color',[0 0 1])

set(gca,'xtick',[])
xlabel('Index')
ylabel('Delta drag (N)')
legend_string={'1-chamber offset','2-chamber offset',...
    '3-chamber offset','4-chamber offset','5-chamber offset',...
    '6-chamber offset','7-chamber offset',...
    '8-chamber offset','9-chamber offset'};
columnlegend(2,legend_string,'location','northeast')
hold off

z=linspace(1,9,9)';
zz=linspace(1,9)';
Z1=[max(y1),max(y2),max(y3),max(y4),max(y5),...
    max(y6),max(y7),max(y8),max(y9)]';
Z2=[min(y1),min(y2),min(y3),min(y4),min(y5),...
    min(y6),min(y7),min(y8),min(y9)]';
Z3=[mean(y1),mean(y2),mean(y3),mean(y4),mean(y5),...
    mean(y6),mean(y7),mean(y8),mean(y9)]';

pz1=polyfit(z,Z1,7);
ZZ1=polyval(pz1,zz);
pz2=polyfit(z,Z2,7);
ZZ2=polyval(pz2,zz);
pz3=polyfit(z,Z3,7);
ZZ3=polyval(pz3,zz);

figure(2)
set(gcf,'color','w');
set(0,'defaultfigureposition',[100 100 800 600])
```

```
set(gca,'Fontsize',[15])
plot(zz,ZZ1,'-r','Linewidth',3)
grid on
hold on
plot(zz,ZZ3,'-b','Linewidth',3)
plot(zz,ZZ2,'-g','Linewidth',3)

plot(z,Z1,'sr','Linewidth',3)
plot(z,Z2,'sg','Linewidth',3)
plot(z,Z3,'sb','Linewidth',3)
xlabel('Chamber offset from the base')
ylabel('Drag (N)')
legend('Upper limit baffle-drag','Average baffle-drag',...
    'Lower limit baffle-drag','location','northeast')
hold off
% ------------------------------------------------------- %
% Baffle-drag variations as a function of number of dataset %
% 1200 m/sec (M = 3.49) in 45 degree BTRA configuration %

clc
clear all

X1=linspace(10,20,11)';
Y1=[4709.14,5256.30,11148.23,14192.42,6131.30,2190.10,...
    664.30,11416.92,14488.47,8394.59,11752.93]';
p1=polyfit(X1,Y1,6);
x1=linspace(10,20);
y1=polyval(p1,x1);

X2=linspace(10,20,10)';
Y2=[5396.14,16235.53,5948.12,2969.00,2877.10,11643.53,...
   16617.03,3265.05,11648.79,2080.70]';
p2=polyfit(X2,Y2,6);
y2=polyval(p2,x1);

X3=linspace(10,20,9)';
Y3=[5583.09,11035.42,5275.30,6223.20,10956.53,5637.80,...
    1935.06,425.37,5334.90]';
p3=polyfit(X3,Y3,6);
y3=polyval(p3,x1);

X4=linspace(10,20,8)';
Y4=[382.98,188.00,2021.10,20056.83,6324.80,9044.17,...
    4774.74,5888.52]';
p4=polyfit(X4,Y4,6);
y4=polyval(p4,x1);

X5=linspace(10,20,7)';
Y5=[10840.44,3066.20,11812.53,2775.50,8357.17,6204.49,...
    11088.63]';
p5=polyfit(X5,Y5,6);
y5=polyval(p5,x1);

X6=linspace(10,20,6)';
Y6=[7586.24,16899.83,5468.80,17457.47,5517.49,109.40]';
```

```
p6=polyfit(X6,Y6,6);
y6=polyval(p6,x1);

X7=linspace(10,20,5)';
Y7=[6247.39,381.50,9213.17,14617.79,796.40]';
p7=polyfit(X7,Y7,6);
y7=polyval(p7,x1);

X8=linspace(10,20,4)';
Y8=[11033.94,14300.47,6373.49,8303.90]';
p8=polyfit(X8,Y8,6);
y8=polyval(p8,x1);

X9=linspace(10,20,3)';
Y9=[3648.03,11460.79,59.60]';
p9=polyfit(X9,Y9,6);
y9=polyval(p9,x1);

figure(1)
set(gcf,'color','w');
set(0,'defaultfigureposition',[100 100 800 600])
set(gca,'Fontsize',[15])
plot(x1,y1,'Linewidth',3,'color',[0.502 0.251 0])
grid on
axis([10 20 -13000 35000])
hold on
plot(x1,y2,'Linewidth',3,'color',[0.251 0 0.502])
plot(x1,y3,'Linewidth',3,'color',[0 1 0])
plot(x1,y4,'Linewidth',3,'color',[1 0.502 1])
plot(x1,y5,'Linewidth',3,'color',[1 0 0])
plot(x1,y6,'Linewidth',3,'color',[0 1 1])
plot(x1,y7,'Linewidth',3,'color',[0.9412 0.4706 0])
plot(x1,y8,'Linewidth',3,'color',[0 0 0])
plot(x1,y9,'Linewidth',3,'color',[0 0 1])

plot(X1,Y1,'s','Linewidth',3,'color',[0.502 0.251 0])
plot(X2,Y2,'s','Linewidth',3,'color',[0.251 0 0.502])
plot(X3,Y3,'s','Linewidth',3,'color',[0 1 0])
plot(X4,Y4,'s','Linewidth',3,'color',[1 0.502 1])
plot(X5,Y5,'s','Linewidth',3,'color',[1 0 0])
plot(X6,Y6,'s','Linewidth',3,'color',[0 1 1])
plot(X7,Y7,'s','Linewidth',3,'color',[0.9412 0.4706 0])
plot(X8,Y8,'s','Linewidth',3,'color',[0 0 0])
plot(X9,Y9,'s','Linewidth',3,'color',[0 0 1])

set(gca,'xtick',[])
xlabel('Index')
ylabel('Delta drag (N)')
legend_string={'1-chamber offset','2-chamber offset',...
    '3-chamber offset','4-chamber offset','5-chamber offset',...
    '6-chamber offset','7-chamber offset',...
    '8-chamber offset','9-chamber offset'};
columnlegend(2,legend_string,'location','northeast')
hold off
```

```
z=linspace(1,9,9)';
zz=linspace(1,9)';
Z1=[max(y1),max(y2),max(y3),max(y4),max(y5),...
    max(y6),max(y7),max(y8),max(y9)]';
Z2=[min(y1),min(y2),min(y3),min(y4),min(y5),...
    min(y6),min(y7),min(y8),min(y9)]';
Z3=[mean(y1),mean(y2),mean(y3),mean(y4),mean(y5),...
    mean(y6),mean(y7),mean(y8),mean(y9)]';

pz1=polyfit(z,Z1,6);
ZZ1=polyval(pz1,zz);
pz2=polyfit(z,Z2,6);
ZZ2=polyval(pz2,zz);
pz3=polyfit(z,Z3,6);
ZZ3=polyval(pz3,zz);

figure(2)
set(gcf,'color','w');
set(0,'defaultfigureposition',[100 100 800 600])
set(gca,'Fontsize',[15])
plot(zz,ZZ1,'-r','Linewidth',3)
grid on
hold on
plot(zz,ZZ3,'-b','Linewidth',3)
plot(zz,ZZ2,'-g','Linewidth',3)

plot(z,Z1,'sr','Linewidth',3)
plot(z,Z2,'sg','Linewidth',3)
plot(z,Z3,'sb','Linewidth',3)
xlabel('Chamber offset from the base')
ylabel('Drag (N)')
legend('Upper limit baffle-drag','Average baffle-drag',...
    'Lower limit baffle-drag','location','southwest')
hold off
% ------------------------------------------------------- %
```